Estimating Sensor Motion in Airborne SAR

Kusk, Anders

Publication date:
2006

Document Version
Publisher's PDF, also known as Version of record

Estimating Sensor Motion in Airborne SAR

Ph.D.-Thesis

Anders Kusk
Ørsted•DTU

Supervisors
Jørgen Dall
Erik Lintz Christensen

10 May 2006

Abstract

In airborne synthetic aperture radar (SAR), accurate knowledge of the SAR sensor motion is necessary to achieve an acceptable image quality with respect to resolution, image artifacts and geometrical distortions. For repeat-track interferometry, where SAR images acquired from different passes are combined, the absolute accuracy requirements are even more stringent, as small residual errors will be misinterpreted as scene displacements or topography.

This thesis deals with two aspects of motion estimation in airborne SAR. The first part is an examination of the impact of propeller aircraft vibrations on SAR focusing. Uncompensated high-frequency motion leads to sidelobes (false echoes) in SAR images. Motion measurements from two propeller aircraft are presented and evaluated with respect to their high-frequency content, and the impact of the measured motion on the image quality is predicted. The motion measurements are compared to similar measurements on a jet aircraft. It is shown that narrowband vibrations at harmonics of the propeller frequency appear in the motion data for the propeller aircraft, and that vibration levels for the jet are significantly lower. It is predicted that the levels of the measured physical vibrations do not lead to unacceptable sidelobes if left uncompensated, but aliasing of the vibrations in the INU can induce spurious low-frequency vibrations at the aliased frequencies in the navigation data. This leads to incorrect motion compensation, and since the aliased vibrations can have higher levels than the actual vibrations due to the integration processes in the INU, unacceptable sidelobes may result.

The second part of the thesis deals with correction of differential motion errors in airborne repeat track SAR interferometry. The work extends an existing differential motion estimation algorithm that integrates the azimuth misregistration to obtain an estimate of the differential motion error between the images. In this thesis, the algorithm is analysed, and potential error sources are identified and examined. One error source is azimuth misregistrations from performing motion compensation with unknown topography. A simple method for reducing topography-induced errors using an external DEM is proposed, and it seems to slightly improve the motion estimate on the L-band EMISAR data for which it was tested.

Another error source in the residual motion algorithm is along-track residual motion errors, which lead to azimuth misregistrations that can be interpreted wrongly as vertical velocity errors. A method is proposed for estimating and correcting these errrors using an external DEM or - as is possible in some cases - the residual range misregistration. The proposed method is tested on a 100 km C-band scene, for which the observed residual cross-track error was still on the order of 15 cm after the initial correction. This variation was reduced to below 2 cm over a 60 km long strip in azimuth.

Resumé

I flybåren syntetisk apertur radar (SAR) er nøjagtigt kendskab til SAR-sensorens bevægelser nødvendig for at opnå en acceptabel billedkvalitet med hensyn til opløsning, falske ekkoer og geometrisk forvrængning. Hvis der skal udføres repeat-track interferometri, hvor flere SAR-billeder optaget fra separate spor kombineres, bliver kravene til absolut nøjagtighed endnu strengere, da små restfejl kan blive misfortolket som forskydninger i scenen, eller som hidrørende fra topografien.

Denne afhandling beskæftiger sig med to aspekter af bevægelsesestimation i flybåren SAR. I første del undersøges indflydelsen af vibrationer i propelfly på SAR-fokuseringen. Ukompenserede højfrekvente bevægelser af SAR-sensoren kan føre til sidesløjfer (falske ekkoer) i fokuserede SAR-billeder. Bevægelsesmålinger fra to propelfly præsenteres og analyseres med hensyn til deres højfrekvensindhold, og den forventede indflydelse af de målte bevægelser på SAR-fokuseringen beregnes. Bevægelsesmålingerne sammenlignes med tilsvarende målinger for et jetfly. Det eftervises at harmoniske af propelfrekvensen dukker op i de målte bevægelser for propelflyene, og at vibrationsniveauerne for jetflyet er betydeligt lavere end disse. Med de målte vibrationsniveauer forventes det ikke at de fysiske vibrationer fører til uacceptable sidesløjfer, hvis de ikke kompenseres. Dog kan aliasering af højfrekvente vibrationer i INU'en introducere falske lav-frekvente vibrationer ved den aliaserede frekvens i bevægelsesdata. Dette fører til fejl i bevægelseskompensationen, og på grund af den integration, der foretages i INU'en, kan de aliaserede vibrationer have højere niveauer end de fysiske vibrationer, og dette kan føre til uacceptable sidesløjfeniveauer.

Anden del af afhandligen beskæftiger sig med korrektion af restbevægelsesfejl i flybåren repeat-track SAR interferometri. Det udførte arbejde tager udgangspunkt i en eksisterende algoritme til estimation af restbevægelsesfejl, der fungerer ved at integrere azimuth-misregistreringen mellem to SAR-billeder. I denne afhandling analyseres algoritmen, og potentielle fejlkilder identificeres og undersøges. Én fejlkilde er azimuth-misregistreringer forårsaget af topografi-uafhængig bevægelseskompensation. Der foreslås en simpel metode til at reducere sådanne fejl vha. en extern højdemodel, og metoden ser ud til at medføre en lille forbedring af estimatet af restbevægelsesfejlen for de L-bånds EMISAR data metoden blev afprøvet på.

En anden fejlkilde er restbevægelsesfejl i flyveretningen. Disse fører til azimuth-misregistrering, som fejlagtigt tolkes som restfejl i tværretningen. Der foreslås en metode til at estimere og korrigere sådanne fejl ved hjælp af en extern højdemodel eller - som det i nogle tilfælde er muligt - misregistreringen i range-retningen. Den foreslåede metode testes på en 100 km lang C-bånds-scene, for hvilken restbevægelsesfejlen stadig var af størrelsesordenen 15 cm efter korrektionen af restbevægelsesfejlen med den originale algoritme. Denne fejl reduceres med den ny metode til under 2 cm over en 60 km lang stribe i azimuth-retningen.

Contents

Chapter 1

Introduction

Synthetic Aperture Radar (SAR) is a well-established technology for remote sensing, and has applications in geophysics, topographic mapping, disaster management and many other areas. Numerous space- and airborne systems have been built and flown. Spaceborne systems have the advantage of wide coverage, whereas airborne systems have a higher degree of freedom in the choice of imaging geometry and revisit times. Also, due to the shorter range to the imaged area, airborne SAR systems achieve higher signal-to-noise ratios than spaceborne systems.

The subject of this thesis is estimation of sensor motion in airborne SAR, a subject which has seen much attention. Accurate knowledge of the SAR sensor motion is critical to achieve a good focusing quality. With the introduction in the 1990's of integrated Inertial (INU) and GPS navigation solutions, acceptable image quality can now be obtained without autofocusing algorithms. The INU is still necessary to estimate the high-frequency content of the motion, whereas the GPS corrects for the slowly varying drift of the INU. However, even with kinematic GPS, absolute positioning errors of 5-10 cm are still seen.

In this work, two aspects of airborne SAR motion estimation are examined. The first part is an examination of the impact of propeller-induced vibrations on the focusing quality in high-performance SAR systems mounted on propeller aircraft. This was motivated by the now discontinued SAR++ program [1] at Ørsted•DTU, in which, among other configurations, high-resolution (25 cm) SAR systems at C- and X-band frequencies with strict sidelobe level requirements were studied. It is well known that uncompensated sinusoidal motion errors can lead to sidelobes in the SAR impulse response, and it is conceivable that such errors could be introduced by propeller motion. To examine this, high-frequency INU motion data from a Lockheed-Martin C-130 Hercules were collected as part of this study. These motion data were compared to motion data from a small propeller aircraft, a Piper PA31 Navajo and, for reference, a GIII Gulfstream jet aircraft. Spectral analysis and point target simulations have been performed to estimate the impact on the focusing quality of a hypothetical SAR system mounted on one of these aircraft.

The second, and major, part of the thesis deals with estimation of differential motion errors in airborne repeat track SAR interferometry (RTI). SAR Interferometry is a powerful technique that can be used to detect small shifts between two SAR images acquired from different tracks. In single-pass interferometry (often referred to as across-track interferometry, or XTI), the images are acquired simultaneously

from two antennas mounted on the same aircraft. In this case, the observed phase shifts are related to the scene topography, and therefore XTI systems are often used for generation of digital elevation models (DEMs). In repeat track interferometry, the SAR images are acquired at different times, and the interferometric phase shift contains contributions both from the topography and from temporal changes in the imaged scene. This can be used to detect small displacements, for example due to landslides or glacial motion. Also, the possibility of a large baseline not limited by the aircraft dimensions allows a higher sensitivity to topography. However, since the motion errors in the two different acquisitions are generally not correlated, the difference in the motion errors is directly seen in the interferometric phase. Since the desired interferometric range shifts are often smaller than the 5-10 cm motion estimation errors which is state-of-the-art with kinematic GPS, calibration techniques using the acquired data must be applied. This may be augmented by using tie-points in the image or an external elevation model. Another problem is phase errors caused by atmospheric delays. The interferometric range shift from such errors can be up to several centimeters, so for high-precision applications this cannot be ignored.

In this work, an existing method [2] for differential motion error estimation in airborne RTI has been examined. The method is based on integration of the observed azimuth misregistration between the images to obtain a non-parametric estimate of the differential motion error. This is based on the assumption that the observed azimuth misregistration is entirely due to uncompensated cross-track velocities. However, azimuth misregistrations are also caused by along-track motion errors, and by performing motion compensation with unknown topography. The contributions from these sources of misregistration on the differential motion estimate have been analysed in this work, and methods have been developed for correcting for them using a coarse external DEM. Finally, the original algorithm has been applied to EMISAR data, and the suggested improvements have also been applied. The influence of the atmosphere on the interferometric phase has not been covered.

The thesis starts with a brief review of SAR motion compensation in Chapter 2. This is followed by the vibration analysis in Chapter 3. In Chapter 4, a brief review of motion errors in SAR interferometry is given, followed by a description of the differential motion estimation algorithm on which this work is based. The analysis and suggested improvements to the algorithm is presented in Chapter 5, and the experimental verification using EMISAR data is presented in Chapter 6, together with a discussion of the achieved results. Finally, the conclusion is presented in Chapter 7.

Chapter 2

Motion Errors in SAR Focusing

In this chapter, the origin and impact of sensor motion errors in airborne SAR are discussed. First, basic SAR focusing and motion compensation theory is presented. Then the impact of motion estimation and compensation errors on the focused SAR image is analysed. The topic of SAR motion errors and compensation has been discussed widely in the literature, e.g. [3, 4, 5], and the theory in this chapter is based on the literature.

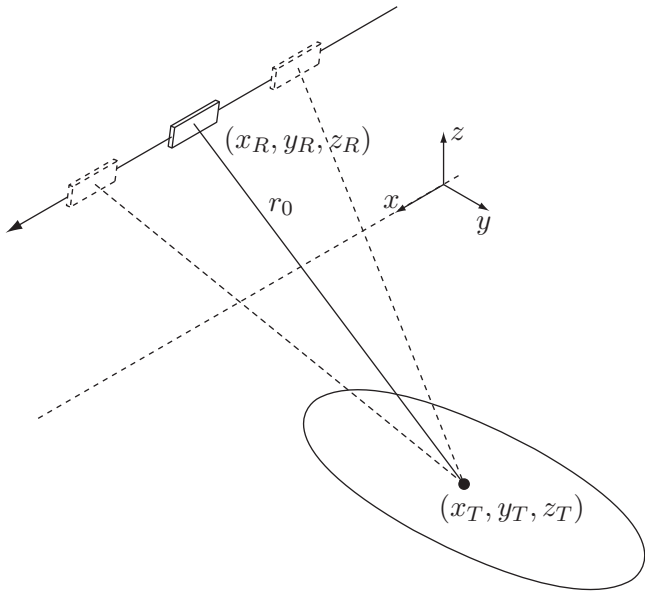

Figure 2.1: Simplified SAR geometry.

2.1 Basic SAR theory

2.1.1 Definitions and assumption

A simplified broadside looking SAR geometry is shown in Figure 2.1. An (x, y, z) coordinate system is defined such that the reference track, to which the SAR image is focused, can be described by the nominal position vector $\boldsymbol{p}_R(x) = (x, 0, z_R)$, where z_R is the (constant) reference track altitude. In these coordinates the target position

is $\boldsymbol{p}_T = (x_T, y_T, z_T)$.

For analysing the airborne SAR focusing process, it is sufficient to assume a flat Earth geometry, since the flat Earth approximation simplifies the analysis and has little impact on the focusing quality. A spherical geometry that accounts more accurately for the curvature of the sensor track is in the following chapters adopted where appropriate.

2.1.2 Focusing with nominal sensor motion

With nominal sensor motion, the range history of the target at $\boldsymbol{p}_T$ is

$$
\begin{aligned}
r_R(x) &= \|\boldsymbol{p}_T - \boldsymbol{p}_R(x)\| && (2.1)\\
&= \sqrt{(\boldsymbol{p}_T - \boldsymbol{p}_R(x)) \cdot (\boldsymbol{p}_T - \boldsymbol{p}_R(x))} && (2.2)\\
&= \sqrt{(x_T - x)^2 + y_T^2 + (z_T - z_R)^2} && (2.3)\\
&= \sqrt{(x_T - x)^2 + r_0^2} && (2.4)\\
&\approx r_0 + \frac{(x - x_T)^2}{2r_0} && (2.5)
\end{aligned}
$$

where the constant $r_0 = \sqrt{y_T^2 + (z_T - z_R)^2}$ is the range of closest approach, and the azimuth-varying part is termed the range migration, $r_M \approx \frac{(x-x_T)^2}{2r_0}$.

The nominal received signal, u, is then, after range compression and assuming a rectangular azimuth envelope:

$$
u(x, r; \boldsymbol{p}_T) = \begin{cases} a(r - r_R(x)) \exp(-j\frac{4\pi}{\lambda}(r_0 + \frac{(x-x_T)^2}{2r_0})) & |x - x_T| \le L/2 \\ 0 & \text{otherwise} \end{cases} \quad (2.6)
$$

where L is the synthetic aperture length, $a(r)$ is the range compressed pulse envelope, and λ is the radar operating wavelength. The range-Doppler algorithm, which has been used in the present work, uses the fact that the azimuth signal of (2.6) is a linear FM chirp with large time-bandwidth (actually space-bandwidth) product for typical SAR geometries. This establishes a stationary-phase relationship [6, pp.142–146] between azimuth space and azimuth spatial frequency:

$$
f_x = -\frac{2(x - x_T)}{\lambda r_0} \quad (2.7)
$$

This is convenient, since an azimuth Fourier transform of (2.6) makes the range migration of the Fourier transformed azimuth signal independent of x_T:

$$
r_M(f_x; r_0) = \frac{\lambda^2 r_0}{8} f_x^2 \quad (2.8)
$$

The azimuth transformed signal is a chirp signal in f_x following the locus $r_0 + r_M(f_x)$ It can be shown [7] that the azimuth Fourier transform of (2.6) can be approximated by (again ignoring the azimuth envelope):

$$U_{Az}(f_x, r; r_0) \approx a(r - r_0 - r_M(f_x; r_0)) \cdot \exp(j2\pi \frac{\lambda^2 r_0}{8} f_x^2) \cdot \exp(-j2\pi f_x x_T) \tag{2.9}$$

The first term of (2.9) represents the range envelope and range migration, the second term is the azimuth chirp, and the final linear phase term is related to the location of the target. For each ouput range, r_0, and azimuth frequency, f_x, the range-Doppler algorithm corrects the range migration by interpolation of the locus given by $r_0 + r_M(f_x)$, so that energy from all targets at r_0 is located at bin r_0. After this procedure, the data are multiplied by the reference function H_{Az}^*, which is the complex conjugate of

$$H_{Az}(f_x; r_0) = \exp(j2\pi \frac{\lambda^2 r_0}{8} f_x^2) \tag{2.10}$$

A final inverse azimuth transform gives the focused image.

2.2 Motion compensation

In order to use frequency-domain focusing methods such as the range-Doppler algorithm, the point target range history should be azimuth invariant. This means that the SAR data must appear as though they were collected from an equidistantly sampled uniform track. With a flat Earth approximation, this would be a straight line, and for a spherical Earth approximation a great-circle track. Since it is not possible to achieve such ideal tracks for aircraft, which are subject to wind gusts, turbulence and other atmospheric phenomena, motion compensation must be applied. The motion compensation procedure attempts to correct the collected SAR data to make them appear as though they had been collected from the ideal track.

2.2.1 Sensor track with non-ideal motion

The actual track of the sensor, including deviations from the reference track, can be described by the position vector $\boldsymbol{p}_A(x) = \boldsymbol{p}_R(x) + \Delta\boldsymbol{p}(x)$ where $\Delta\boldsymbol{p}(x) = (\Delta x, \Delta y, \Delta z)^T$ is the deviation from the reference track. If the length of $\Delta\boldsymbol{p}$ is small compared to the range to the target, the actual range can be written using (2.1) as

$$\begin{aligned} r_A &= \sqrt{(\boldsymbol{p}_T - \boldsymbol{p}_A) \cdot (\boldsymbol{p}_T - \boldsymbol{p}_A)} \\ &= \sqrt{(\boldsymbol{p}_T - \boldsymbol{p}_R - \Delta\boldsymbol{p}) \cdot (\boldsymbol{p}_T - \boldsymbol{p}_R - \Delta\boldsymbol{p})} \\ &= \sqrt{(\boldsymbol{p}_T - \boldsymbol{p}_R) \cdot (\boldsymbol{p}_T - \boldsymbol{p}_R) - 2(\boldsymbol{p}_T - \boldsymbol{p}_R) \cdot \Delta\boldsymbol{p} + \Delta\boldsymbol{p} \cdot \Delta\boldsymbol{p}} \\ &\approx \|\boldsymbol{p}_T - \boldsymbol{p}_R\| \sqrt{1 - \frac{2(\boldsymbol{p}_T - \boldsymbol{p}_R) \cdot \Delta\boldsymbol{p}}{\|\boldsymbol{p}_T - \boldsymbol{p}_R\|^2}} \\ &\approx r_R - \boldsymbol{\eta}_{los} \cdot \Delta\boldsymbol{p} \end{aligned} \tag{2.11}$$

where $\boldsymbol{\eta}_{los} = (\boldsymbol{p}_T - \boldsymbol{p}_R)/\|\boldsymbol{p}_T - \boldsymbol{p}_R\|$ is the line-of-sight unit vector from the reference track to the target. The line-of-sight vector is dependent both on the target position and the sensor position along the reference track, but with a short synthetic aperture it can be considered constant, and the value when the target is at broadside can be used. This simplifies motion compensation greatly, since all echoes received at a given range-azimuth cell can then be motion compensated using the same range displacement, regardless of whether they were received from the center or the edge of the aperture. This approximation is often referred to as the center-of-aperture approximation, and will be adopted in the following.

With the center-of-aperture assumption, the range difference along the aperture is

$$\Delta r(x; \boldsymbol{p}_T) = r_A(x) - r_R(x) \approx -\Delta\boldsymbol{p}(x) \cdot \boldsymbol{\eta}_{los}(\boldsymbol{p}_T; \boldsymbol{p}_R(x_T)) = -\Delta\boldsymbol{p}(x) \cdot \boldsymbol{\eta}_T \quad (2.12)$$

where the line-of-sight vector $\boldsymbol{\eta}_T$ is now solely a function of the target crosstrack position. Since a broadside-looking system is assumed, $\boldsymbol{\eta}_T$ will have no component in the azimuth(x) direction. This means that the azimuth component, Δx, of $\Delta\boldsymbol{p}$ will have little effect on the range history of the target, and thus will not affect the focusing quality significantly. An azimuth displacement will occur, but if it is known it can easily be corrected by resampling in azimuth before focusing. The critical part of the motion compensation is in the cross-track direction, or (y, z)-plane, and in the following, the two-dimensional line-of-sight vector $\boldsymbol{n}_T$, written as a function of the look angle, θ_T, from reference track to target in the (y, z)-plane, will be used:

$$\boldsymbol{n}_T = \begin{bmatrix} \sin\theta_T \\ -\cos\theta_T \end{bmatrix} \quad (2.13)$$

The two-dimensional cross-track position displacement vector will likewise be introduced:

$$\Delta\boldsymbol{p}_{yz} = \begin{bmatrix} \Delta y \\ \Delta z \end{bmatrix} \quad (2.14)$$

The range displacement can then be written

$$\Delta r \approx -\Delta\boldsymbol{p}_{yz} \cdot \boldsymbol{n}_T = -\Delta y \sin\theta_T + \Delta z \cos\theta_T \quad (2.15)$$

2.2.2 Motion compensation procedure

Motion compensation must be carried out individually for each azimuth position, x, and involves four steps:

1. Estimation of sensor position relative to the reference track, $\Delta\boldsymbol{p}(x)$
2. Interpolation in azimuth to correct for the azimuth displacement $\Delta x(x)$
3. Estimation of required range correction $\Delta r(r; x)$
4. Interpolation in range to correct echo positions
5. Phase correction in range to allow azimuth focusing

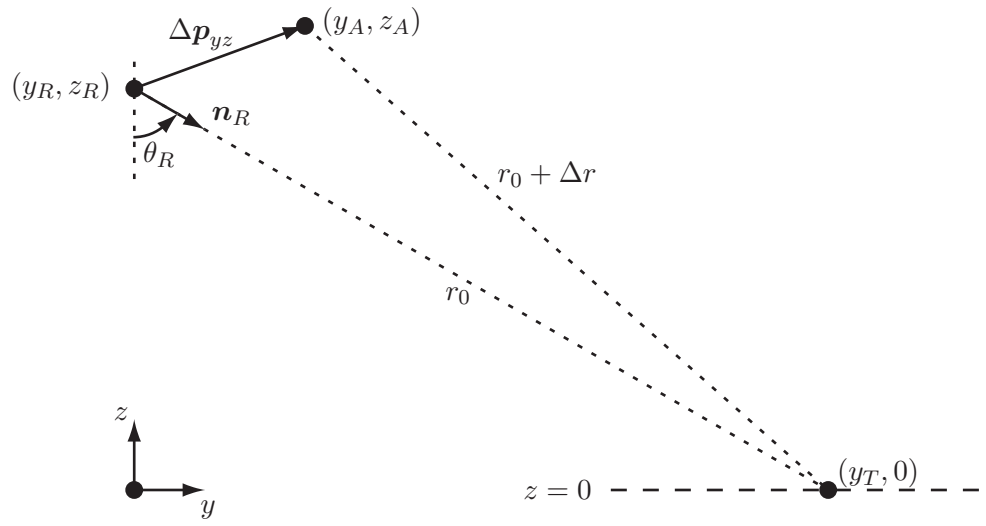

Figure 2.2: Ideal motion compensation geometry.

In the ideal situation, all targets are located on a flat Earth or some other well-defined reference surface, and accurate knowledge of the sensor motion is available. The resulting motion compensation geometry is illustrated in Figure 2.2, where the reference surface has been chosen as the plane at $z = 0$.

For each range, r_0, the required range correction can be estimated by use of (2.15), using the reference surface line-of-sight vector $\boldsymbol{n}_R$ instead of $\boldsymbol{n}_T$. For each focused range, r_0, of the output range line, g_o, an interpolation and phase correction is carried out on the input line, g_i:

$$g_o[r_0] = \exp(\frac{4\pi}{\lambda}\Delta r) \cdot g_i[r_0 + \Delta r] \tag{2.16}$$

After this interpolation and phase correction has been performed for all range output pixels, range migration correction and azimuth compression can then be carried out to complete the focusing process.

Even in the ideal situation with full knowledge of sensor motion and topography, the motion compensation procedure might not result in optimal image quality if the displacement from the reference track becomes too large. In this case, the range variation of the phase correction (2.16) with range will cause a locally linear phase on the impulse responses in the output line. The slope of this linear phase varies with range, and causes a range variant shift of the range spectra. This can cause problems if it is not accounted for in the range migration interpolation. The effect is closely related to the baseline decorrelation seen in SAR interferometry (see 4.1.3).

2.2.3 Residual motion errors

Accurate motion compensation requires accurate knowledge of the sensor motion and, ideally, also the topography. The non-ideal situation is illustrated in Figure 2.3, where motion estimation errors and an unknown line-of-sight vector, $\boldsymbol{n}_T$ are included. The actual shift to be compensated is

$$\Delta r = -\Delta \boldsymbol{p}_{yz} \cdot \boldsymbol{n}_T = -(\Delta \widehat{\boldsymbol{p}}_{yz} + \Delta \boldsymbol{p}_{yz,\epsilon}) \cdot \boldsymbol{n}_T \tag{2.17}$$

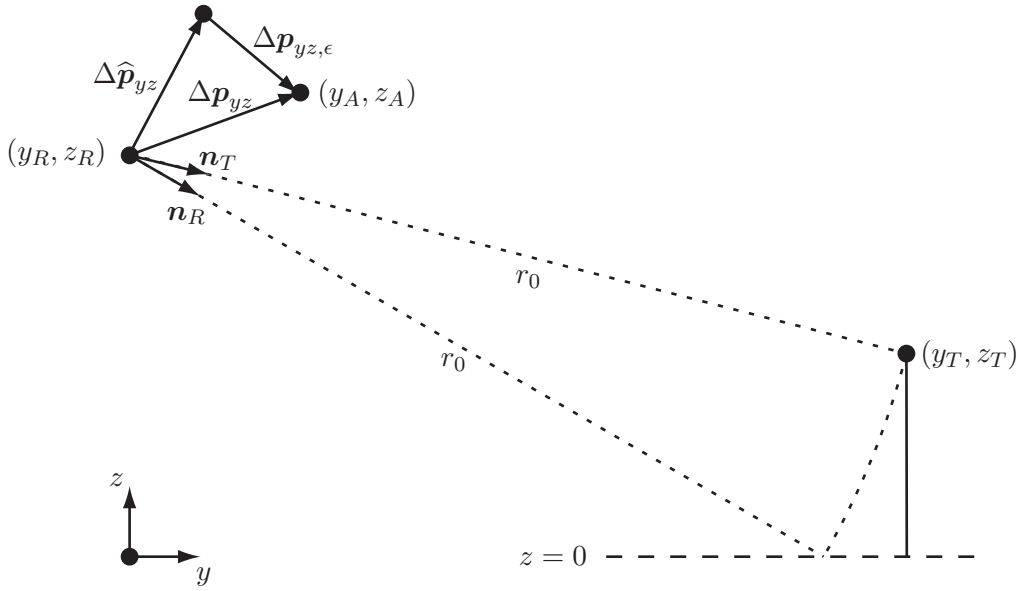

Figure 2.3: Motion compensation geometry with unknown topography and motion estimation errors.

where $\Delta\widehat{\boldsymbol{p}}_{yz}$ is the estimated sensor motion relative to the reference track and $\Delta\boldsymbol{p}_{yz,\epsilon}$ is the residual motion error. The residual motion error is the uncompensated displacement that remains after the estimated displacement has been corrected. The applied motion compensation is

$$\Delta\widehat{r} = -\Delta\widehat{\boldsymbol{p}}_{yz} \cdot \boldsymbol{n}_R \tag{2.18}$$

The residual range displacement is thus

$$\Delta\tilde{r} = \Delta r - \Delta\widehat{r} \approx -\Delta\widehat{\boldsymbol{p}}_{yz} \cdot (\boldsymbol{n}_T - \boldsymbol{n}_R) - \Delta\boldsymbol{p}_{yz,\epsilon} \cdot \boldsymbol{n}_T = \Delta r_{topo} + \Delta r_\epsilon \tag{2.19}$$

where

$$\Delta r_{topo} = -\Delta\widehat{\boldsymbol{p}}_{yz} \cdot (\boldsymbol{n}_T - \boldsymbol{n}_R) \tag{2.20}$$

is the residual range shift due to the topography coupling with the compensated displacement, and

$$\Delta r_\epsilon = -\Delta\boldsymbol{p}_{yz,\epsilon} \cdot \boldsymbol{n}_T \tag{2.21}$$

is the residual range shift due to a residual motion error. In addition to the range displacement, an uncompensated phase occurs:

$$\tilde{\phi} = -\frac{4\pi}{\lambda}\Delta\tilde{r} = \phi_{topo} + \phi_\epsilon \tag{2.22}$$

where

$$\phi_{topo} = -\frac{4\pi}{\lambda}\Delta r_{topo} = \frac{4\pi}{\lambda}\Delta\widehat{\boldsymbol{p}}_{yz} \cdot (\boldsymbol{n}_T - \boldsymbol{n}_R) \tag{2.23}$$

and

$$\phi_\epsilon = -\frac{4\pi}{\lambda}\Delta r_\epsilon = \frac{4\pi}{\lambda}\Delta\boldsymbol{p}_{yz,\epsilon} \cdot \boldsymbol{n}_T \tag{2.24}$$

Even with perfect knowledge of the sensor motion ($\Delta \boldsymbol{p}_{yz,\epsilon} = 0$), a range shift occurs due to the unknown topography. This shift is the basis of interferometry (see section 4.1), where the uncompensated phase shift is used to infer the topography. However, if the displacement to be compensated changes along the aperture, the impulse response can be affected, as described in section 2.3.

2.3 Impact of motion errors on focusing

Residual motion errors can cause both geometric distortion and degradation of the SAR impulse response. In the ideal case, the impulse response is, without weighting, a sinc-function in both the range and azimuth directions. If a motion error is introduced along the aperture, the effect is a modification of the impulse response. Constant and linear motion errors cause geometric distortions (shift of the impulse response), whereas higher-order motion errors cause a degradation of the impulse response (defocusing, loss of contrast and ghost echoes). The main impact of higher order motion errors comes from the azimuth phase error (2.22). Higher order motion errors can be divided into slowly varying errors, which can be modeled by a polynomium of degree two or larger, and high-frequency errors, which can be modeled by a Fourier series or a Gaussian white noise process.

2.3.1 Constant and linear motion errors

The effect of a constant residual motion error is to shift the image in the range direction. The shift is range-dependent, according to (2.15).

A linear cross-track motion error occurs if there is a constant uncompensated cross-track velocity $\frac{\partial \Delta p_{yz,\epsilon}}{\partial x}$. This is illustrated on Figure 2.4, where, due to the residual motion error, the assumed sensor track is along the x-axis, but the image is acquired and focused to the actual track, which is rotated by the angle α. The angle α is related to the residual cross-track motion error by

$$\tan \alpha = \frac{\partial \Delta \boldsymbol{p}_{yz,\epsilon}}{\partial x} \cdot \boldsymbol{n}_T \tag{2.25}$$

If $\alpha \ll 1$, which will be the case for small motion errors, then

$$\tan \alpha \approx \sin \alpha \approx \alpha \tag{2.26}$$

From the figure it is clear that the cross-track velocity error causes the image to be shifted in range and azimuth, with an azimuth shift, δ_x, given by

$$\delta_x = x_A - x_R = r_0 \sin \alpha \approx r_0 \frac{\partial \Delta \boldsymbol{p}_{yz,\epsilon}}{\partial x} \cdot \boldsymbol{n}_T = -r_0 \frac{\partial \Delta r_\epsilon}{\partial x} \tag{2.27}$$

and a range shift, δ_r, given by

$$\delta_r = r_A - r_R = r_0 \cos \alpha - r_0 = -r_0(1 - \cos \alpha) \tag{2.28}$$

If $\alpha \ll 1$, then $(1 - \cos \alpha) \ll \sin \alpha$, and the main effect of the linear error is the shift in the azimuth direction. This azimuth shift is proportional to range, and to the projection of the cross-track velocity on the line-of-sight direction. As an example, if there is a cross-track velocity error of 1 m/s with a nominal along-track velocity of 240 m/s, the resulting azimuth shift for a target at 10 km range is 42 m, whereas the range shift is only −9 cm.

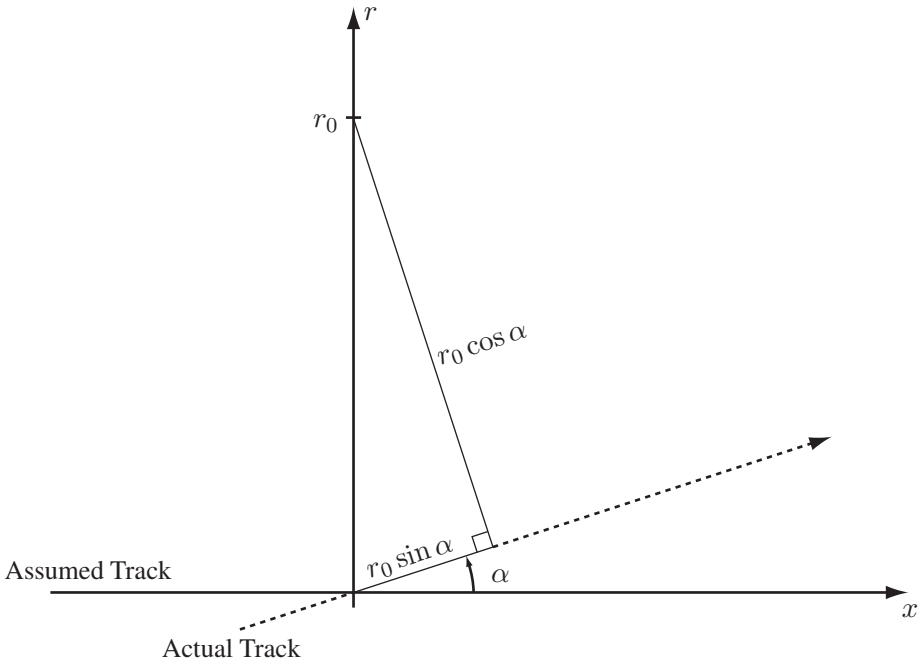

Figure 2.4: Effect of a linear cross-track motion error, looking down into the slant range plane.

2.3.2 Higher order motion errors

The main effect of higher-order motion errors is a modification of the azimuth impulse response through the azimuth phase error along the aperture introduced by (2.24). There are three main effects of higher-order motion errors,

1. Defocusing, which increases the 3 dB-width of the azimuth impulse response (loss of resolution) and decreases the peak level (loss of signal-to-noise ratio)
2. Increased sidelobe levels (paired echoes) in the impulse response, which can mask weaker targets. This can be evaluated by the Peak Sidelobe to Mainlobe Ratio (PSLR)
3. Loss of image contrast, which can be evaluated by the Integrated Sidelobes to Mainlobe Ratio (ISLR)

Various phase errors and their effects are illustrated in Figure 2.5 and discussed in the following.

Phase errors that can be modeled by a polynomial of order higher than one generally cause defocusing and/or asymmetric sidelobes in the impulse response, but will not be dealt with in detail in the remainder of the report. A quadratic phase error, which can occur if there is an uncompensated cross-track acceleration, leads to defocusing since an incorrect azimuth chirp rate is used. Such a quadratic phase error is illustrated in Figure 2.5a. Typically, a quadratic phase error with a maximum variation of $\pi/4$ along the aperture is accepted with respect to focusing quality [7].

High frequency peridodic motion errors can be modeled by a Fourier series. Concentrating on a single sinusoidal motion error component, the azimuth phase error

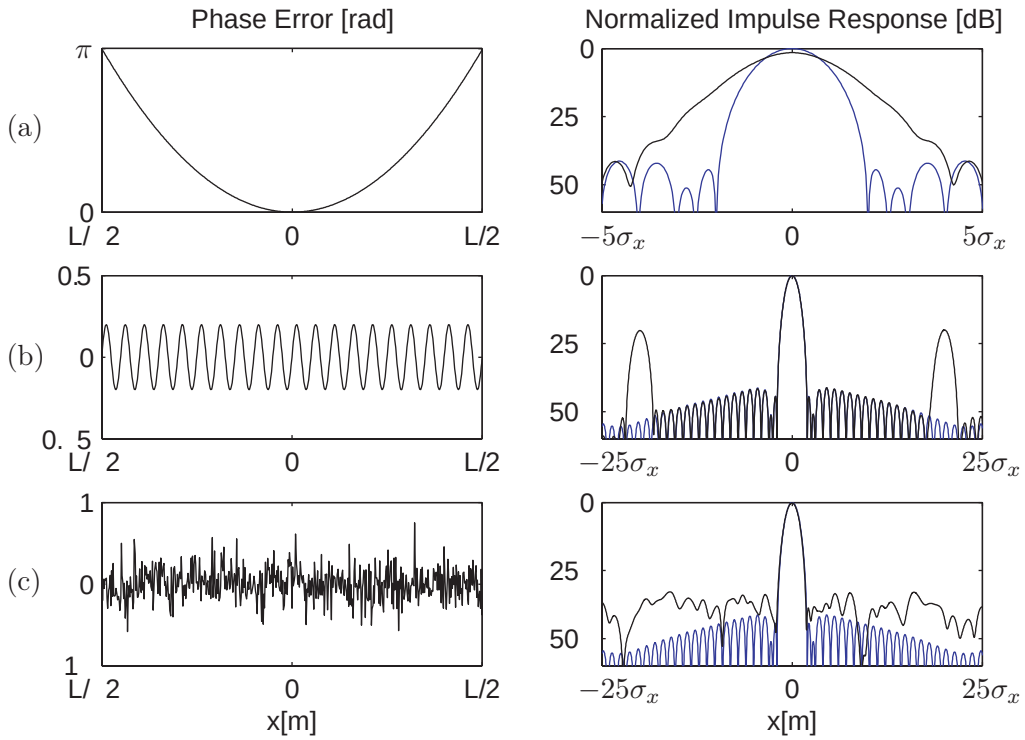

Figure 2.5: Effects of azimuth phase errors on the Hamming-weighted impulse response, (a) Quadratic phase error with maximum value of π at edge of aperture, (b) Sinusoidal phase error with $\phi_k = 0.2$ rad and $f_{x,k} = 20/L$, (c) Random phase error with $\phi_{rms} = 0.2$ rad. Blue curve is the nominal response, black is with phase error.

resulting from a motion error can be written

$$\phi_\epsilon(x) = \phi_k \sin(2\pi f_{x,k} x) = -\frac{4\pi}{\lambda} r_k \sin(2\pi f_{x,k} x) \tag{2.29}$$

where r_k is the amplitude of the motion error projected on the line-of-sight direction, ϕ_k is the corresponding amplitude of the phase variation and $f_{x,k}$ is the spatial frequency of the vibration. Assuming a constant sensor along-track velocity v_x, the spatial frequency is related to the temporal frequency, $f_{t,k}$ by

$$f_{x,k} = \frac{f_{t,k}}{v_x} \tag{2.30}$$

The nominal azimuth signal is multiplied by the phase factor:

$$\exp(j\phi_k \sin(2\pi f_{x,k} x)) = \sum_{n=-\infty}^{\infty} J_n(\phi_k) \exp j2\pi n f_{x,k} x \tag{2.31}$$

where J_n is the n^{th} order Bessel function of the first kind. Assuming $\phi_k \ll \pi$, the following approximations apply [8]:

$$\begin{aligned} J_0(\phi_k) &\approx 1 \\ J_{\pm 1}(\phi_k) &\approx \pm\frac{\phi_k}{2} \\ J_n &\approx 0, \qquad |n| > 1 \end{aligned} \tag{2.32}$$

Thus (2.31) can be approximated by

$$\exp(j\phi_k \sin(2\pi f_{x,k} x)) \approx 1 + \frac{\phi_k}{2}(\exp(j2\pi f_{x,k} x) - \exp(-j2\pi f_{x,k} x)) \tag{2.33}$$

The multiplication of the nominal azimuth response by (2.33) results in the nominal signal plus two attenuated replicas shifted in spatial frequency by $f_{x,k}$. Using (2.7) and (2.33), it is seen that the focused image will contain the nominal impulse response plus two attenuated responses displaced from the mainlobe by $\pm\xi_x$ where

$$\xi_x = \frac{\lambda r_0}{2} f_{x,k} = \frac{\lambda r_0}{2v_x} f_{t,k} \tag{2.34}$$

The amplitude of the echoes compared to the mainlobe is $\frac{\phi_k}{2}$, so the resulting PSLR is

$$\text{PSLR} = 20\log(\frac{|\phi_k|}{2}) \tag{2.35}$$

Evaluated in terms of the displacement amplitude, r_k, this can be written

$$\text{PSLR} = 20\log(\frac{2\pi}{\lambda}|r_k|) \tag{2.36}$$

The effect of a sinusoidal phase error with 20 cycles of variation along the aperture and an amplitude of 0.2 rad is shown in Figure 2.5b.

Uncorrelated random phase errors will result in sidelobes in the focused impulse response along the length of the aperture. The average level of these sidelobes are determined by the RMS-value of the phase error, and can be shown to lead to an ISLR of [5]:

$$\text{ISLR} = 20\log(\phi_{RMS}), \qquad \phi_{RMS} \ll \pi \tag{2.37}$$

A random phase error with $\phi_{RMS} = 0.2$ is illustrated in Figure 2.5c.

2.4 Estimation of sensor motion

For airborne SAR systems, the primary motion sensor has typically been the Inertial Navigation Unit, or INU. An INU has the advantage of a high update rate (typically 50-200 Hz) and high short-term accuracy, but drift of the navigation solution can cause low-frequency motion errors, with consequences for focusing as described in 2.3.1. The position drift errors are typically measured in nautical miles per hour.

The Global Positioning System (GPS) complements an INU nicely, since the GPS navigation solution has good long-term stability but a low update rate (typically on the order of 1 Hz). Navigation systems that integrate an INU and a GPS receiver are available today, one example is the Honeywell H764G unit used in the EMISAR system, and in the vibration analysis in Chapter 3. The accuracy of a stand-alone GPS receiver is measured in meters, but using phase-differential methods such as kinematic GPS, this can be improved to a typical accuracy of 5-10 cm. Differential methods require one or more reference GPS receivers on the ground. Thus application of kinematic GPS in on-line navigation requires real-time access to such a reference network, but if this is not available, recorded navigation data can be corrected off-line.

The integration of GPS and INU navigation data is a field of study in itself, and methods range from simple polynominal corrections of the INU data [9] to Kalman filtering solutions incorporating sophisticated navigation sensor models [10].

Chapter 3

Aircraft Vibrations and SAR Focusing

In this chapter, the impact of aircraft propeller vibration on SAR focusing is examined. The original motivation for this study was to examine whether the motion compensation requirements of a high-performance SAR system – the now discontinued SAR++ program at Ørsted•DTU EMI [1] – could be met by a low-cost aircraft installation, e.g. on a propeller aircraft. As mentioned in 2.3.2, a sinusoidal motion error causes an increase in PSLR on the focused azimuth impulse response. One design goal of the SAR++ system was a Peak Sidelobe Ratio (PSLR) of -40 dB for the impulse response. Uncompensated vibrations induced by propeller rotation could cause undesired sidelobes in the SAR image, undermining these goals.

Previous studies of aircraft vibrations in SAR focusing have typically been carried out in conjunction with a specific system design, e.g. [11, 12]. In these studies, the focus has been on random vibrations associated with air turbulence. However, little, if anything, has been published on high-frequency sinusoidal motion effects from propeller vibration and its influence on SAR focusing. In the present study, the focus is on high-frequency narrow-band vibrations.

For the vibration analysis, motion measurements from three different types of aircraft were compared. The types of aircraft represent three different categories:

- A Lockheed C-130 Hercules heavy propeller transport aircraft,
- A Piper PA31 Navajo light six-seat propeller aircraft,
- A Gulfstream GIII medium-size jet aircraft, included for reference.

The three aircraft types are illustrated in Figure 3.1. The C-130 measurements are the most complete. They were carried out by the author for the purposes of this study, piggybacking on a radiometer mission over the Atlantic Ocean. The Piper measurements were kindly supplied by Kristian Keller of the Danish National Survey and Cadastre (KMS), who collected them on gravimetric flights over Vadehavet in Denmark. The GIII measurements were carried out in conjunction with an EMISAR flight over Zeeland, Denmark but the motion data were not used for actual SAR motion compensation.

a)

b)

c)

Figure 3.1: Aircraft types used in vibration analysis. (a) Lockheed-Martin C130, (b) Piper Navajo PA31, (c) Gulfstream GIII.

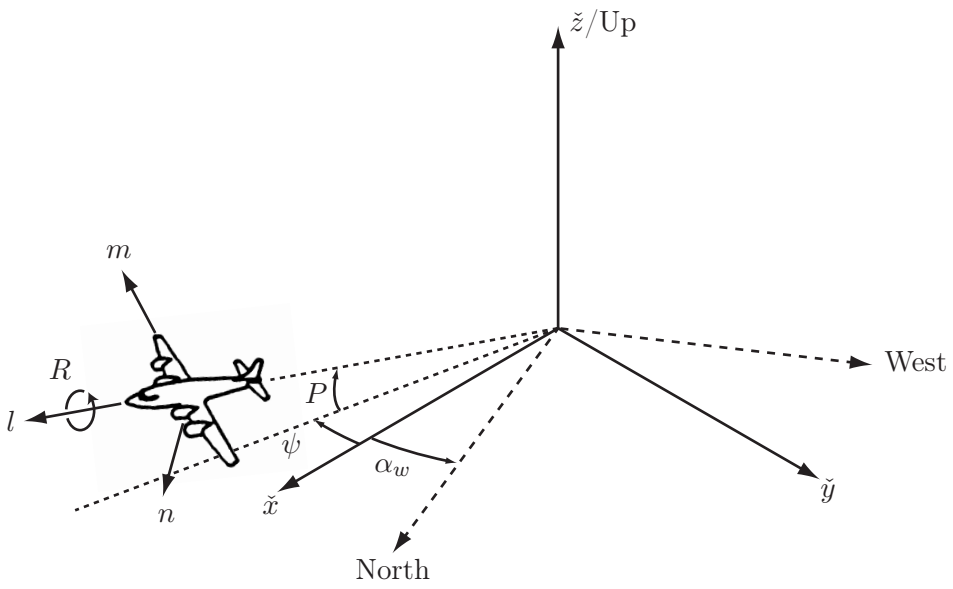

Figure 3.2: Coordinate systems and angles used in motion estimation. For illustration purposes, the origin of the (l, m, n)-system has been displaced, but it is actually coincident with the origin of the $(\check{x}, \check{y}, \check{z})$ and the (North,West,Up) system.

First, the motion sensor is described and the methodology used to measure and evaluate motion impact is presented. Then motion measurements from the three aircraft platforms are presented and evaluated. The motion measurements are evaluated with respect to their high-frequency content, and the impact on SAR focusing of these vibrations is estimated. Then aliasing of high-frequency vibrations is examined, and, finally, the results are discussed. The vibration analysis in this work has also been summarized in [13].

3.1 Motion sensor description

The type of motion sensor used in this analysis is a Honeywell H764G EGI (Embedded GPS in an Inertial Navigation System)[14]. The EGI unit is capable of delivering high speed motion data at 200 Hz, in the form of instantaneous acceleration, velocity and attitude, as well as position data (in the form of latitude, longitude and altitude) at 50 Hz. In the following, the operating principle of the H764G EGI is described. The description is based on [14], [15], and [10].

3.1.1 EGI coordinate systems

To describe the EGI navigation processing, the coordinate systems defined in Figure 3.2 are necessary. These are also the coordinate systems used by the EGI.

The (l, m, n) system, or aircraft body frame, is a moving coordinate system with origin at the instantaneous EGI position. The (l, m, n) system is assumed fixed with respect to the airframe, with the pointing direction of l along the roll (R) axis, m along the pitch (P) axis, and n along the yaw (Y) axis. Note that the yaw axis is pointing down through the bottom of the aircraft.

The $(\check{x}, \check{y}, \check{z})$ system is the EGI navigation frame, which the EGI uses to calculate its navigation solution. The high speed outputs (200 Hz) are also referenced to this system. Its origin is, as the aircraft body frame, at the instantaneous EGI position, but it is a locally level coordinate system, i.e. the $\check{x}$- and $\check{y}$-axes lie in a plane parallel to a plane that is tangent to the reference ellipsoid (the WGS-84 ellipsoid) and the $\check{z}$-axis is perpendicular to the reference ellipsoid and points up. The $\check{x}$- and $\check{y}$- axes are rotated relative to the North- and West-directions, respectively, by the wander angle, α_w. The wander angle is a leftover from early gimbaled INU systems. In these systems, the inertial sensors were isolated from aircraft movements by mounting them in rotating gimbals, so that the sensor axes were made to physically track the navigation frame axes. In order to prevent the sudden 180° change in North/South direction when navigating near the poles, the navigation frame axes were rotated relative to the North/West axes by the wander angle. The time variation of the wander angle can be described by the following expression for its derivative:

$$\dot{\alpha}_w(t) = -\dot{\varphi}_{lon}(t) \cdot \sin \varphi_{lat}(t) \tag{3.1}$$

The orientation of the aircraft body frame with respect to the navigation frame is given by the three attitude angles, ψ (azimuth angle), P (pitch), and R (roll), as defined on the figure[1]. The true heading of the aircraft, ψ_{th}, can be calculated from the azimuth angle and the wander angle by

$$\psi_{th} = \psi - \alpha_w \tag{3.2}$$

The coordinate transformation matrix, or direction cosine matrix, for rotating body frame coordinates (l, m, n) to navigation frame coordinates $(\check{x}, \check{y}, \check{z})$ is

$$\boldsymbol{C}_{nav}^{body} = \begin{bmatrix} C_\psi C_P & -S_\psi C_R + C_\psi S_P S_R & S_\psi S_R + C_\psi S_P C_R \\ -S_\psi C_P & -C_\psi C_R - S_\psi S_P S_R & C_\psi S_R - S_\psi S_P C_R \\ S_P & -C_P S_R & -C_P C_R \end{bmatrix} \tag{3.3}$$

where $C_\psi = \cos\psi$, $S_\psi = \sin\psi$, and so forth. Replacing ψ by ψ_{th} in (3.3) gives the coordinate transformation from the body frame to the local geodetic frame (N,W,U).

3.1.2 EGI navigation processing

The EGI is mounted rigidly to the aircraft with its inertial sensors (accelerometers and gyros) aligned with the (l, m, n) aircraft axes. In practice, the sensor axes may have a different (fixed) orientation relative to the aircraft axes, but this is measured at the time of installation and programmed into the EGI, which automatically compensates for this. For the purposes of the present discussion, the sensor axes can be assumed to be aligned with the (l, m, n) axes.

The inertial sensors consists of three accelerometers and three gyros. The accelerometers measure accelerations along the l,m, and n axes, and the gyros measure rotation rates about these axes. All measurements are with respect to inertial space.

Before a flight, the initial position and attitude of the EGI must be established. The position (latitude, longitude, and altitude) is input by the operator (or the

[1]Note that the term "azimuth" is often used for along-track position in SAR theory, but this is unrelated to the azimuth angle used here.

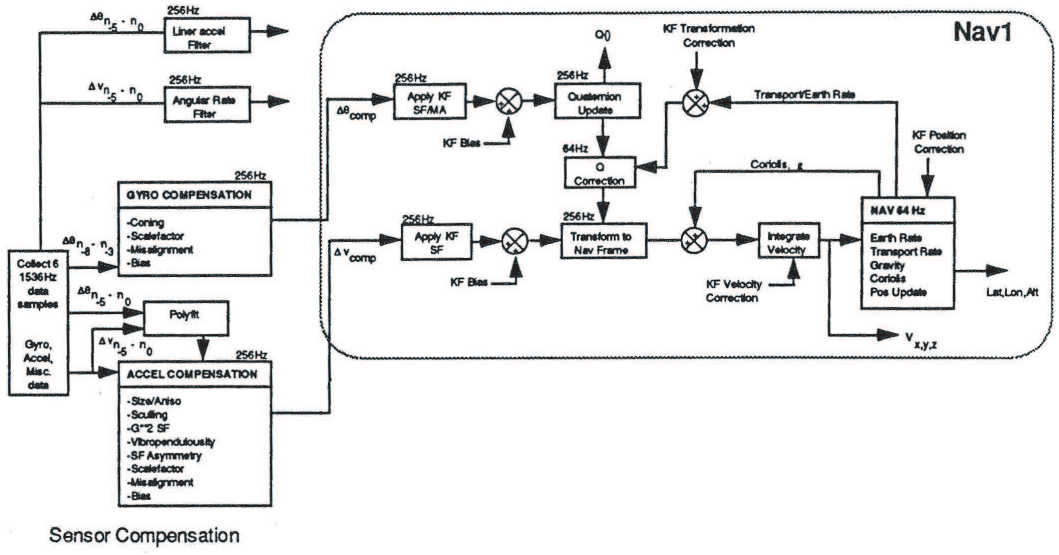

Figure 3.3: Inertial navigation processing flow for the H764G EGI, from [15]. Note that the EGI used in this project uses different sampling frequencies than illustrated on the figure. Thus 1536 Hz, 256 Hz, and 64 Hz on the figure corresponds to 1200 Hz, 200 Hz and 50 Hz in the EGI used in this project.

GPS position is used), after which the EGI performs an alignment to establish its initial attitude (azimuth, pitch, and roll angle). During the alignment, which takes a few minutes, the EGI does not move, and the pitch and roll is estimated using the accelerometer measurements and the fact that these only measure gravitational acceleration when the EGI is not moving. The initial azimuth angle is established using a procedure called gyrocompassing, which relies on the gyro measurements and knowledge of the Earth rotation rate. After the alignment, the EGI can begin navigating, as described in the following.

The processing that the EGI performs when navigating is illustrated on Figure 3.3. The inertial sensors are sampled at 1200 Hz, and the measurements are compensated for various non-idealities using temperature measurements and stored calibration data. The compensated acceleration and rotation rate measurements (Δv_{comp} and $\Delta\theta_{comp}$ on the figure) are propagated at 200 Hz to the navigation processor (Nav1 on the figure). Also, the raw measurements, filtered and decimated to 200 Hz, are available in the EGI output (upper left part of the figure).

As mentioned earlier, the EGI also contains a GPS receiver, which works by measuring the distance to GPS satellites. The EGI merges the GPS and inertial measurements in a Kalman filter, which uses a sophisticated model of the EGI to keep track of various sensor errors. These include (but are not limited to) bias, scale factors, and misalignments of the inertial sensors; velocity, attitude, and position errors; and GPS clock errors. All available measurements are used in the Kalman filter, but its error estimates are updated at 1 Hz only. Based on these error estimates, Kalman filter corrections are applied at all levels in the navigation processing, indicated by the abbreviation KF in Figure 3.3. The GPS part of the EGI will not be covered in further detail here, since it does not affect the estimate of high-frequency motion above 1 Hz.

After the the Kalman filter corrections for scale factors (SF), misalignment (MA) and bias of the inertial sensors, the sensor attitude is updated using the measured attitude rates. In principle, this can be done using direction cosine matrices, but for numerical reasons, the EGI keeps track of attitude using quarternions, which are four-element vectors that can be used to describe rotations [10]. Mathematically, however, the results are equivalent, and in the following, the process is described using direction cosine matrices. The derivative of (3.3) can be written

$$\frac{\mathrm{d}}{\mathrm{d}t}\boldsymbol{C}_{nav}^{body} = \boldsymbol{C}_{nav}^{body}\begin{bmatrix} 0 & -\omega_Y & \omega_P \\ \omega_Y & 0 & -\omega_R \\ -\omega_P & \omega_R & 0 \end{bmatrix} \tag{3.4}$$

where ω_R, ω_P, and ω_Y are the roll, pitch, and yaw axis angular rates (i.e. rotation rates about the l, m, and n axes, respectively) as measured by the gyroscopes. The attitude update ("Quarternion Update" in Figure 3.3) thus corresponds to a numerical integration of (3.4), at each step using the previous value of the stored attitude. This integration is performed at 200 Hz. Gyroscopes measure rotations relative to an inertial frame, but the body frame and navigation frame are both rotating coordinate systems, so the measured attitude is corrected for the motion of the sensor and the Earth rate ("Transport/Earth rate" in Figure 3.3). This correction, which is combined with the Kalman filter correction of attitude, is performed on all of the 200 Hz samples, but the correction parameters are only updated at 50 Hz, since they depend on the position of the sensor, and this is only calculated at 50 Hz.

The updated, corrected attitude is used to transform the measured body frame accelerations to the navigation frame. Since the navigation frame is rotating, the navigation frame accelerations include a Coriolis component, which is corrected for. The next step is the correction for the gravitational acceleration, which is calculated using the sensor position and a model of the Earth gravity field. The measured acceleration is the inertial acceleration minus the gravitational acceleration (i.e. if the EGI is sitting still on the Earth surface, it measures what appears to be an upwards acceleration). An error in the sensor altitude will lead to an error in the estimated gravitational acceleration, and this is a positive feedback mechanism, since if the altitude estimate is, for example, too high, the estimated gravitational acceleration is too low, causing an upwards acceleration error. This leads to instability of the vertical position estimate, so inertial navigation units on aircraft need an external measurement of altitude, which can be provided from a pressure altimeter or from the GPS altitude. In both cases, the external altitude measurement is merged with the inertial measurements through the Kalman filter.

After the Coriolis and gravitational acceleration correction, the accelerations are integrated to obtain velocities in the navigation frame ($v_{x,y,z}$ in Figure 3.3), and these are available at 200 Hz. The navigation frame velocities are integrated to obtain displacement in the navigation frame, and this displacement is then used to update the sensor position (which is also the origin of the navigation frame). The position calculation is only performed at 50 Hz, and the output is Latitude, Longitude, and Altitude on the reference ellipsoid. The wander angle, which is used to horizontally rotate navigation frame velocities to (North-West-Up) or (East-North-Up)-velocities, is also output at 50 Hz.

The latitude, longitude, and altitude outputs of the EGI are not suitable for SAR motion compensation, both due to coarse quantization, and due to discontinuities

in the data at 1 second intervals caused by the Kalman filter position corrections. Therefore, the position estimation in EMISAR processing is based on integration of velocities [30].

3.1.3 EGI high frequency characteristics

To use the EGI data for estimating aircraft vibration levels, the frequency characteristic of the EGI should be known. The EGI output sampling frequency is 200 Hz, sufficient to represent motion in the 0-100 Hz band. Unfortunately, the EGI high-frequency characteristics are not well described in the documentation, and if the measurement bandwidth of the EGI is lower than 100 Hz, the vibration levels estimated from the EGI data may be lower than the actual physical vibrations. On the other hand, if the EGI measurement bandwidth extends beyond 100 Hz, vibrations above 100 Hz may be aliased to frequencies in the 0-100 Hz band. The following description has been assembled from various references.

The accelerometers (Honeywell Q-Flex QA2000) used in the EGI have a bandwidth of more than 300 Hz [16], whereas the gyros (GG1320 Digital Ring Laser Gyro) have a bandwidth on the order of 1000 Hz when mounted in a rigid sensor block [17]. According to [15], the H764 EGI's inertial sensors are internally mounted in a rigid aluminum block, so this is indeed the case. Both values are comfortably above the 100 Hz output bandwidth of the EGI, so the level of the vibrations in the band from 0-100 Hz should be reliably measured by the EGI.

It is not indicated on Figure 3.3 or elsewhere in the EGI documentation whether the transition from 1200 Hz to 200 Hz sampling implies a low-pass anti-alias filtering operation, although this would be natural. One reason for this could be the fact that the gyros are dithered in order to prevent a phenomenon known as lock-in, which causes the output of a ring laser gyro to be 0 at low angular rates [10]. The dithering is a small amplitude, high-frequency (on the order of 500 Hz) sinusoidal rotation applied to the gyro to ensure that it never operates in the lock-in region. It is applied inside the gyro casing, and a piezoelectic sensor mounted in the casing estimates the applied dither, which is then subtracted before the angular rate measurement is output from the gyro. Nevertheless, there may be a residual dither signal present in the angular rate measurement, and this would turn up as an error peak at the dither frequency in the spectrum of the output angular rate. If no anti-aliasing was applied, this would cause the dither frequency to be aliased to a frequency in the 0-100 Hz band. The same thing would happen to actual physical vibrations of the EGI above 100 Hz. Thus, if aliased vibration peaks can be identified in the motion data, the level of the original vibration cannot be reliably estimated since the frequency characteristics of the EGI above 100 Hz is not known. However, the aliased motion signal will be a pure error signal.

3.1.4 Selection of motion variables for vibration measurements

The output motion data that are available at 200 Hz are summarized in Table 3.1. The output raw body accelerations and angular rates *are* filtered, according to the upper left part of Figure 3.3), but the quantities that would be used in SAR motion compensation are the output navigation frame velocities ($v_{x,y,z}$ in Figure 3.3) and navigation frame attitude angles (not indicated directly in the Figure). On Figure 3.4

Variable	Description
a_l, a_m, a_n	Filtered body accelerations
$\dot{Y}$, $\dot{P}$, $\dot{R}$	Filtered angular rates
$v_{\check{x}}$, $v_{\check{y}}$, $v_{\check{z}}$	Navigation frame velocities
ψ, P, R	Azimuth angle, pitch, and roll

Table 3.1: Overview of available 200 Hz motion data.

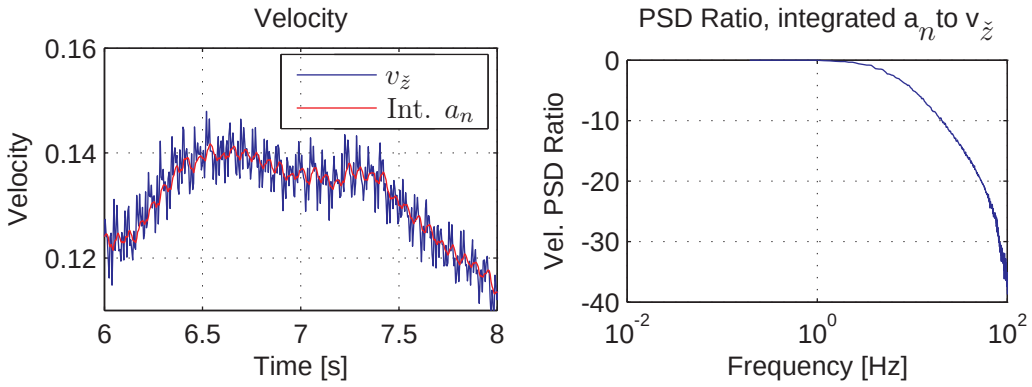

Figure 3.4: Comparison of integrated vertical body acceleration and navigation frame vertical velocity. A linear trend has been removed from both quantities.

is shown a comparison of the output navigation frame vertical velocity, $v_{\check{z}}$, and the velocity calculated from the output vertical body acceleration, a_n. The figure is based on a short segment of level flight, taken from the C130 dataset described in section 3.2.1. For level flight, the n and $\check{z}$ axes are approximately parallel, although the n-axis points down and the $\check{z}$-axis points up. The a_n component was inverted and integrated and a linear trend was removed. This was necessary since the output a_n has not been compensated for gravity acceleration, but the linear trend removal does not affect the high-frequency content. The only correction applied to $v_{\check{z}}$ was removal of a linear trend. On the left side of Figure 3.4, the integrated a_n is plotted together with $v_{\check{z}}$ for comparison. It is clearly seen that the navigation frame velocities have more high frequency content. This is also seen from the power spectral densities (PSD) of the integrated a_n and the $v_{\check{z}}$ components. These were calculated, and on the right part of Figure 3.4, the ratio of the two PSD's is plotted. The ratio resembles a low-pass filter characteristic with a 3 dB frequency of 7 Hz. A similar trend was seen when comparing output body angular rates and output navigation frame attitude angles. Although this does not reveal whether the data used in the navigation processing are low-pass filtered, it indicates that the output body accelerations and angular rates should not be used for vibration level estimation since they would underestimate the high-frequency vibration levels seen in SAR motion compensation data above 7 Hz.

3.2 Measurements

In this section, the measurement setups for the various aircraft vibration measurements is described.

3.2.1 C-130 measurement setup

The C-130 Hercules is a heavy military transport aircraft. As such it is not the obvious choice for a low-cost SAR installation (see the chapter introduction), as operating cost are generally high. However, since the C-130 can fly with open doors (at low altitude) and sensor equipment can easily be installed on cargo pallets, a SAR installation could possibly be made without costly modifications of the airframe. The C-130 has four four-blade turboprop engines, and under normal operation, the propeller rotation rate is fixed at 1020 RPM =17 Hz.

Vibration measurements for the C-130 were carried out during a radiometer flight to the North Atlantic. The H764G EGI unit used was borrowed from KMS, and full 200 Hz velocity and attitude data were collected. Existing EGI data collection software was modified by the author for the purposes of this mission. A second EGI (the one used in EMISAR) was used by the radiometer, and on the homeward transit after the main mission was completed, data were collected from the EMISAR EGI as well. The EMISAR EGI has the problem, however, that attitude data are delivered at 200 Hz but only updated at 50 Hz. This is probably due to a bug in the firmware. Velocity measurements are updated at 200 Hz, though. Unfortunately it was not possible to collect data from both EGIs at the same time.

The KMS EGI was mounted at the bottom of a rack that was again mounted on one of the C-130 standard cargo pallets. The installation is shown on Figure 3.5. A GPS antenna was mounted in a roof window in the front of the aircraft and connected to the EGI to improve the long-term stability of the navigation solution, although this was not strictly required for the purposes of this investigation.

The data set selected for processing was collected when the C-130 was flying at an altitude of 25000 feet and a velocity of 350 knots. This velocity is close to maximum for the C-130, which would be desirable in a SAR system to increase both flight stability and coverage. An altitude of 25000 feet was also typically intended in EMISAR flights.

3.2.2 Piper PA31 measurement setup

The Piper PA31 Navajo is a six seat light business aircraft used for many purposes. It has two three-blade turbopiston engines, where the propeller rotation rate is set by the pilot according to flight conditions and requirements. The particular aircraft used in this measurement is operated as a surveying aircraft by the Danish surveying company SCANKORT A/S.

The Piper measurements were kindly supplied by Kristian Keller of the Danish National Survey and Cadastre (KMS), who collected them on gravimetry flights over Vadehavet. The EGI was the same unit used for the C-130 measurements. On the Piper, the EGI was mounted in a rack that was latched into a seat mount and screwed tight to the floor. The data collection was made with software that collected only 50

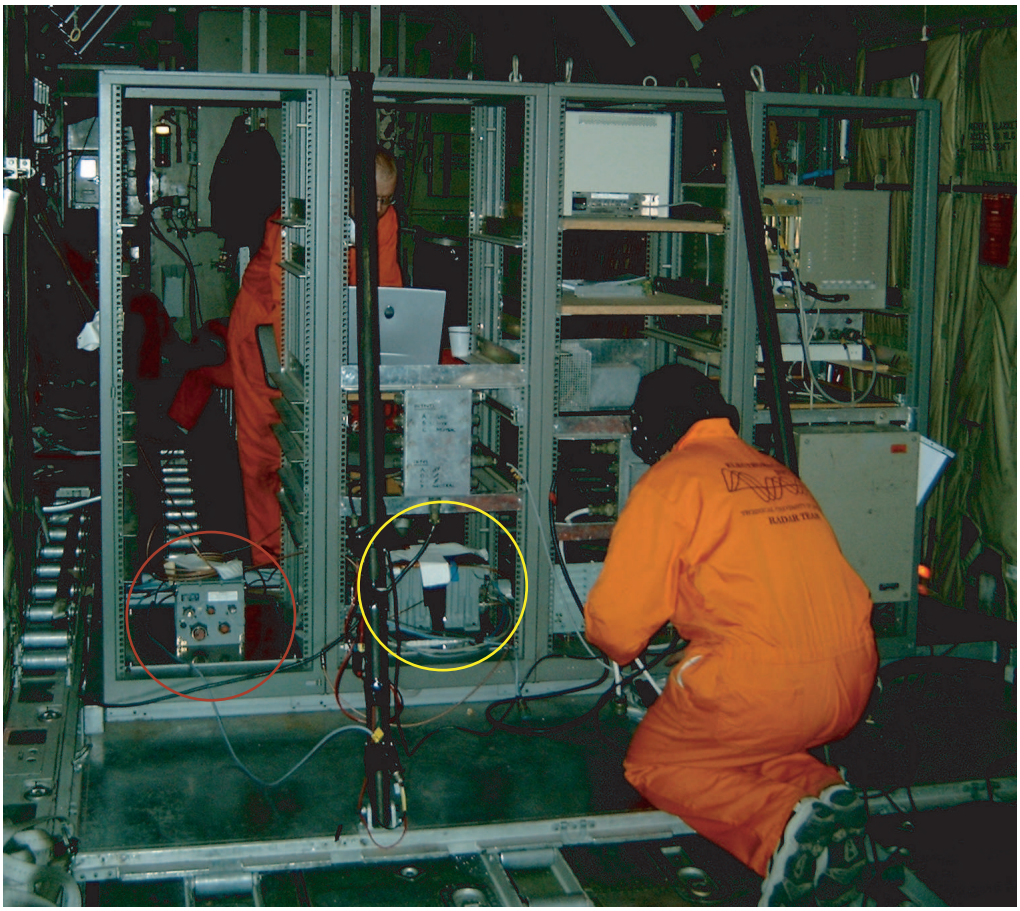

Figure 3.5: C-130 EGI Installation. The KMS EGI is indicated by the red circle and the EMISAR EGI (yellow circle) is mounted next to it, rotated 90°.

Hz data, so 200 Hz measurements are unfortunately not available.

The data set used for analysis was collected flying at 3400 feet and a speed of 150 knots. However, the Piper is capable of flying at 25000 feet and a speed of 200 knots. These could be suitable values for flying a SAR system, but unfortunately motion data were not available for these flight conditions. The maximum propeller rotation rate for the Navajo is 2575 RPM = 42.9 Hz, but the actual propeller rotation rates used for this flight were not logged.

3.2.3 GIII measurement setup

The GIII is a medium-sized jet aircraft used for both civilian and military purposes. It has two tail-mounted turbojet engines. The EMISAR system was mounted on a GIII of the Royal Danish Airforce, and the GIII measurements were included in this analysis in order to compare the vibration environment of a propeller aircraft to that of a jet aircraft.

The motion data were collected during an EMISAR flight, but not during SAR data collection, where the EGI is controlled by EMISAR, which only collects 50 Hz data. As mentioned in 3.2.1, the EMISAR EGI only updates attitude data at 50 Hz, even when 200 Hz data are collected, so only 50 Hz attitude data are available. As for the mounting, the EGI was screwed tight onto a metal plate latched into a seat mount.

The flight conditions were very similar to those of the C-130 measurements, with an altitude of 25000 feet and a velocity of 380 knots.

3.2.4 Summary of flight conditions

The relevant parameters for the three different aircraft measurements are summarized in Table 3.2

Aircraft	Engine Type	Speed [kts]	Altitude [feet]
C-130 Hercules	4 × 4-blade Turboprop	350	25000
PA-31 Navajo	2 × 3-blade Piston	150	3400
Gulfstream GIII	2 × Turbojet	380	25000

Table 3.2: Flight conditions for motion measurements.

3.3 Vibration analysis

This section describes the processing carried out on the collected EGI data to estimate vibration amplitudes and their impact on SAR focusing.

3.3.1 Model for small aircraft vibrations

In the following, a model for small amplitude aircraft deviations from the reference track is derived. It is assumed that the aircraft/EGI follows a straight and level track in the reference (x, y, z) coordinate system similar to Figure 2.1 and is only

perturbed from the reference motion by small scale translational and rotational body vibrations. The reference motion of the SAR antenna is given by

$$\boldsymbol{p}_R(t) = \begin{bmatrix} v_{x,nom}t \\ 0 \\ 0 \end{bmatrix} + \begin{bmatrix} 1 & 0 & 0 \\ 0 & -1 & 0 \\ 0 & 0 & -1 \end{bmatrix} \boldsymbol{d}^{body} \tag{3.5}$$

where $v_{x,nom}$ is the sensor reference along-track velocity and $\boldsymbol{d}^{body}$ is the leverarm vector from the EGI to the SAR antenna, specified in the (l, m, n) body coordinates:

$$\boldsymbol{d}^{body} = \begin{bmatrix} d_l \\ d_m \\ d_n \end{bmatrix} \tag{3.6}$$

The small scale vibrations are modeled by the body accelerations, a_l, a_m, and a_n, and by the rotations R, P, and Y. The roll (R) and pitch (P) angles are defined as in Figure 3.2, whereas the yaw (Y) angle is defined like the azimuth angle, but is measured relative to the nominal track, so that a yaw angle of 0 indicates that the aircraft is pointed in the nominal direction of flight. According to (3.3), the transformation from body coordinates to reference track coordinates is given by:

$$\boldsymbol{C}_{ref}^{body} = \begin{bmatrix} C_Y C_P & -S_Y C_R + C_Y S_P S_R & S_Y S_R + C_Y S_P C_R \\ -S_Y C_P & -C_Y C_R - S_Y S_P S_R & C_Y S_R - S_Y S_P C_R \\ S_P & -C_P S_R & -C_P C_R \end{bmatrix} \tag{3.7}$$

Since small perturbations are assumed, $Y, P, R \ll 1$, so $C_X = \cos X \approx 1$, and $S_X = \sin X \approx X$, where X is either Y, P or R. With these approximations, and assuming also that double and triple products can be neglected,

$$\boldsymbol{C}_{ref}^{body} \approx \begin{bmatrix} 1 & -Y & P \\ -Y & -1 & R \\ P & -R & -1 \end{bmatrix} \tag{3.8}$$

The translational motion of the EGI in the (x, y, z)-system can be expressed as

$$\begin{aligned} \boldsymbol{p}_M(t) &= \int \begin{bmatrix} v_{x,nom} + v_x(t) \\ v_y(t) \\ v_z(t) \end{bmatrix} \mathrm{d}t = \begin{bmatrix} v_{x,nom}t \\ 0 \\ 0 \end{bmatrix} + \int\int \begin{bmatrix} a_x(t) \\ a_y(t) \\ a_z(t) \end{bmatrix} \mathrm{d}t^2 \\ &\approx \begin{bmatrix} v_{x,nom}t \\ 0 \\ 0 \end{bmatrix} + \int\int \begin{bmatrix} 1 & -Y(t) & P(t) \\ -Y(t) & -1 & R(t) \\ P(t) & -R(t) & -1 \end{bmatrix} \begin{bmatrix} a_l(t) \\ a_m(t) \\ a_n(t) \end{bmatrix} \mathrm{d}t^2 \\ &\approx \begin{bmatrix} v_{x,nom}t \\ 0 \\ 0 \end{bmatrix} + \int\int \begin{bmatrix} a_l(t) \\ -a_m(t) \\ -a_n(t) \end{bmatrix} \mathrm{d}t^2 \end{aligned} \tag{3.9}$$

where, in the last approximation, it has been assumed that small accelerations coupling with small rotations can be neglected. The actual antenna motion is

$$\begin{aligned} \boldsymbol{p}_A(t) &= \boldsymbol{p}_M(t) + \boldsymbol{C}_{ref}^{body} \boldsymbol{d}^{body} \\ &\approx \boldsymbol{p}_M(t) + \begin{bmatrix} 1 & -Y(t) & P(t) \\ -Y(t) & -1 & R(t) \\ P(t) & -R(t) & -1 \end{bmatrix} \begin{bmatrix} d_l \\ d_m \\ d_n \end{bmatrix} \end{aligned} \tag{3.10}$$

The displacement from the sensor reference track caused by small scale vibrations is then

$$\begin{aligned}\Delta\boldsymbol{p}(t) \approx \boldsymbol{p}_A(t) - \boldsymbol{p}_R(t) &= \int\int \begin{bmatrix} a_l(t) \\ -a_m(t) \\ -a_n(t) \end{bmatrix} \mathrm{d}t^2 + \begin{bmatrix} 0 & -Y(t) & P(t) \\ -Y(t) & 0 & R(t) \\ P(t) & -R(t) & 0 \end{bmatrix} \begin{bmatrix} d_l \\ d_m \\ d_n \end{bmatrix} \\ &= \int \begin{bmatrix} v_x(t) \\ v_y(t) \\ v_z(t) \end{bmatrix} \mathrm{d}t + \begin{bmatrix} 0 & -Y(t) & P(t) \\ -Y(t) & 0 & R(t) \\ P(t) & -R(t) & 0 \end{bmatrix} \begin{bmatrix} d_l \\ d_m \\ d_n \end{bmatrix}\end{aligned} \tag{3.11}$$

where the cross-track motion has been expressed as a function of the velocities and attitude angles, which are used in the motion estimation.

3.3.2 Estimating vibration measurement errors

When estimating the impact of vibrations on the SAR impulse response, it is important to note that it is not the vibrations themselves that cause phase errors, but the failure to estimate and compensate them correctly. The motion measurements presented in this chapter were carried out with one motion sensor, and so a "truth" value is not available for comparison. Ideally, two motion sensors should have been used simultaneously, but this was unfortunately not possible. However, the underlying assumption in the following is that the estimate of high frequency motion due to vibration is potentially erroneous. There are several reasons why the vibration content of measured motion data might not correspond to the actual motion of the SAR antenna:

1. High frequency vibrations can be due to structural vibrations in the airframe. If the SAR antenna is displaced from the motion sensor, the amplitude and/or phase of the vibration might be different at the two locations. This phenomenon is referred to as leverarm flexure. Leverarm flexure effects can be reduced by mounting the motion sensor close to the SAR antenna, but this might not be possible in a low-cost installation.

2. For high frequency vibrations, small unknown delays between SAR data and motion data will cause a frequency-dependent phase shift of the measured vibration. For example, a 10 ms delay will cause a 50 Hz vibration to be measured 180° out of phase, doubling the motion induced phase error. Delays between SAR data and motion data can of course be reduced by proper design and calibration of the SAR system and motion sensor, but it is necessary to be aware of this.

3. High frequency vibrations that are undersampled by the motion sensor can turn up at a lower aliased frequency. Since SAR data are typically collected at a higher frequency than motion data, the corresponding vibration component in the SAR data might not be aliased at all or aliased to a different frequency. This means that, in addition to the uncompensated vibration in the SAR data, a new vibration component is introduced by the motion compensation at the aliased frequency. Means to reduce aliasing effects include using a motion sensor with higher sampling frequency, but systems with a sampling frequency higher than 300 Hz are not generally available.

Aliasing effects can to some extent be identified in the motion sensor data if it is related to harmonics of the propeller frequency. For the other two types of error the motion error cannot be predicted, but it is likely that the potential motion error induced would be the same order of magnitude as the measured vibrations. Therefore, measuring the actual vibration environment provides a rough estimate of the magnitude of such errors.

3.3.3 Assumed SAR system description

To evaluate the impact of measured vibration levels on SAR focusing, assumptions regarding the SAR system must be made. As mentioned in the chapter introduction, the work was carried out with the SAR++ system [1] in mind. This work considered both L, C, and X-band systems. The sidelobes introduced by vibrations will be largest for an X-band system, since according to (2.36) the PSLR is inversely proportional to wavelength, and furthermore, an X-band system will generally have smaller physical dimensions than lower-frequency systems, which would make an installation on a small aircraft more feasible. Therefore the system parameters from the SAR++ X-band configurations have been adopted. The relevant parameters assumed for the vibration analysis are summarized in Table 3.3. The assumed sensor velocity and altitude are those used in each individual motion measurement (see Table 3.2).

Parameter	Value
Wavelength, λ	3.2 cm
Unweighted azimuth resolution	0.25 m
Look angle, θ_R	45°

Table 3.3: Assumed SAR system parameters for analysis.

3.3.4 Motion data processing

In order to get results that are meaningful in a SAR context, the EGI data described in section 3.1.4 must first be transformed to a suitable SAR imaging coordinate system. Thus, short data sets (of a few minutes) exhibiting approximately constant course, velocity and altitude (i.e. during transit) were selected. Since the variation of the wander angle is slow when not travelling near the poles, it is assumed constant for the short duration being processed (see also (3.1)). The mean of the wander angle will be accounted for by the procedure described below, and the actual discrepancy in impulse response arising from assuming a constant wander angle will be of a low-frequency nature, and thus insignificant in the context of this investigation. The investigation proceeds as follows, using the measure motion data summarized in Table 3.1:

1. Select an N-sample motion data set of approximately constant heading, velocity and altitude.

2. Calculate dataset mean of horizontal velocity vector components, i.e the navigation frame velocities $v_{\tilde{x}}[1:N]$ and $v_{\tilde{y}}[1:N]$.

3. Calculate dataset mean azimuth angle by

$$\psi_{mean} = -\arctan(v_{\check{y},mean}/v_{\check{x},mean})$$

Note that ψ is measured positive clockwise with respect to the $\check{x}$-axis.

4. Calculate the yaw angle, Y by:

$$Y[1:N] = \psi[1:N] - \psi_{mean}$$

5. Rotate horizontal velocities to the SAR imaging coordinate system by

$$\begin{bmatrix} v_x \\ v_y \\ v_z \end{bmatrix} = \begin{bmatrix} \cos(\psi_{mean}) & \sin(\psi_{mean}) & 0 \\ -\sin(\psi_{mean}) & \cos(\psi_{mean}) & 0 \\ 0 & 0 & 1 \end{bmatrix} \begin{bmatrix} v_{\check{x}} \\ v_{\check{y}} \\ v_{\check{z}} \end{bmatrix}$$

After this preprocessing, estimates of along-track velocity, v_x, across-track velocities, v_y and v_z, and attitude angles Y, P, and R are available.

The spectra of the measured motion data are estimated by the Welch power spectrum estimation method [18]. With this method, N data samples are divided into smaller bins of length L, with an overlap, M, between bins. Each bin is windowed by a suitable window function (a Blackman window in this work), transformed by FFT, and the resulting amplitude spectra are averaged over all bins. This method was chosen for its simplicity.

The output of the spectral analysis is power spectral density (PSD), which is measured in $(\mathrm{m/s})^2/\mathrm{Hz}$ for velocities and $\mathrm{rad}^2/\mathrm{Hz}$ for attitude angles. Sinusoidal vibrations will turn up as more or less well-defined peaks in the power spectra, and the power in one peak can be estimated by integrating the power spectrum over the width of the peak. This estimated power, $\widehat{\Gamma}_k$, can again be converted to a sinuoidal amplitude, $\widehat{A}_k$:

$$\widehat{A}_k = \sqrt{2 \cdot \widehat{\Gamma}_k} \tag{3.12}$$

3.3.5 PSLR estimation

To evaluate the impact of a measured sinusoidal vibration on SAR focusing, specifically the PSLR, it is necessary to calculate the range displacement and resulting phase error caused by this vibration. Each vibration frequency can be treated separately, as sinusoidal motion errors with different frequencies will give rise to sidelobes at different positions in the impulse response, according to (2.34).

The estimated PSLR gives an idea of the values that could be expected in an actual SAR system. As mentioned in section 3.3.3 an X-band sensor with the parameters from Table 3.3 is assumed. For wavelengths other than X-band, the relative increase or decrease in PSLR can be calculated by (see (2.36)):

$$\Delta\mathrm{PSLR} = -20\log(\frac{\lambda}{3.2\ \mathrm{cm}}) \tag{3.13}$$

For an L-band system (λ =24 cm), the PSLR from a given vibration is 18 dB lower than in the X-band system. For a C-band system at λ =5.66 cm, the PSLR would be approximately 5 dB lower than in the X-band system.

In the following, each component of the measured vibrations (v_y, v_z, Y, P, R) is analyzed individually (v_x does not give rise to significant range displacement, see section 2.2.1). A line-of-sight look angle of $\theta_R = 45°$ is assumed, as mentioned in Table 3.3. This is a typical look-angle for an airborne SAR.

According to (3.11) and (2.15), a horizontal cross-track velocity vibration of frequency $f_{t,k}$ and amplitude $v_{y,k}$ will be projected on to the line-of-sight direction ($\theta = 45°$), and give rise to the range displacement $\Delta r_{y,k}$:

$$\Delta r_{y,k} = \sin\theta_R \int v_{y,k} \sin(2\pi f_{t,k} t)\mathrm{d}t = -\frac{v_{y,k}}{2\sqrt{2}\pi f_{t,k}} \cos(2\pi f_{t,k} t) \tag{3.14}$$

Likewise, a vertical velocity vibration of amplitude $v_{z,k}$ will give a range displacement

$$\Delta r_{z,k} = -\cos\theta_R \int v_{z,k} \sin(2\pi f_{t,k} t)\mathrm{d}t = \frac{v_{z,k}}{2\sqrt{2}\pi f_{t,k}} \cos(2\pi f_{t,k} t) \tag{3.15}$$

The estimated range displacement amplitude is then, for both a horizontal and a vertical cross-track velocity:

$$\Delta r_{v,k} = \frac{v_k}{2\sqrt{2}\pi f_{t,k}} \tag{3.16}$$

The effect of angular vibration can also be seen from (3.11), assuming straight and level flight for which $Y, P, R \ll 1$. Looking at the cross-track components (only they give rise to range displacements), the range displacement is

$$\begin{aligned} \Delta r_{\Theta,k} &= \begin{bmatrix} -Y d_l + R d_n \\ P d_l - R d_m \end{bmatrix} \cdot \boldsymbol{n}_T \\ &= (-Y d_l + R d_n)\sin\theta_R - (P d_l - R d_m)\cos\theta_R \end{aligned} \tag{3.17}$$

The resulting displacement is highly dependent on the leverarm chosen. Since there is no "right" way to chose this, the displacement amplitude corresponding to a specific angular parameter will be estimated by multiplying the vibration amplitude by 1 m. This isolates the effect of a vibration in a single attitude parameter, and gives a result that can be easily related to other leverarm sizes.

To sum up, the following expression can be used to evaluate the PSLR resulting from a velocity vibration of amplitude v_k and frequency $f_{t,k}$ (see (2.36) and (3.16)):

$$\mathrm{PSLR}_v = \frac{\phi_k}{2} = \frac{v_k}{\sqrt{2}\lambda f_{t,k}} \tag{3.18}$$

The PSLR from an angular vibration of amplitude Θ_k is estimated as

$$\mathrm{PSLR}_\Theta = \frac{\sqrt{2}\pi}{\lambda} d_\Theta \Theta_k \tag{3.19}$$

with Θ_k given in radians, $d_\Theta = 1$ m and the displacement projected on the 45° line-of-sight direction.

3.4 C-130 measurements

3.4.1 Motion spectra

The collected motion data for the C-130 were processed as described in section 3.3.4. The estimated vibration spectra are shown in Figures 3.6 and 3.7. A Blackman window was used in the power spectrum estimation to decrease leakage, especially from the low-frequency part of the motion spectrum, which is typically of much larger magnitude than the high-frequency part. The selected values of N, L, and M in the power spectrum estimation (see section 3.3.4), were a compromise between having a long enough data set for sufficient resolution and noise reduction and a sufficiently short data set for constant flight conditions. At the 200 Hz sampling rate, $N = 10000$ corresponds to 50 seconds of data.

Examining the high-frequency part (>10 Hz) of the v_y spectrum, a relatively constant noise floor with peaks at the frequencies 17, 34, 51, 68, and 85 Hz is seen. The C-130 uses constant-speed 4-blade propellers rotating at 1020 RPM or 17 Hz, so the measured frequencies are the fundamental and higher harmonics of the propeller frequency. The largest peak is actually at the blade frequency, 68 Hz, and not at the fundamental propeller frequency. The noise floor level is consistent with the nominal RMS jitter of the EGI velocity outputs [14]. This is specified as $6 \cdot 10^{-4}$ m/s, giving a single sided noise density of -84 dB/Hz with 200 Hz sampling.

The v_z spectrum looks similar to the v_y spectrum except for a slight increase in the noise floor between 50 Hz and 60 Hz, the cause of which is not known. Also, a small peak is seen at 64 Hz which is consistent with the second harmonic(=136 Hz) of the blade frequency aliased by the 200 Hz sampling.

Looking at the attitude spectra, there is an average noise floor slightly below -110 dB/Hz, which is probably due to the EGI attitude quantization of 96 μrad, giving a quantization noise density of -114 dB/Hz. The strongest vibration peak is seen at the fundamental harmonic of the blade frequency, 68 Hz, and the second strongest at the aliased second blade harmonic at 64 Hz. Both peaks are strongest in the roll angle spectrum.

To sum up, the vibration amplitudes estimated from the motion spectra are given in Table 3.4. The table allows a comparison of the different vibration components but do not directly say anything about their impact on SAR focusing. This is analyzed in the following section.

Frequency Hz	v_x mm/s	v_y mm/s	v_z mm/s	R μrad	P μrad	Y μrad
17	0.3	1.5	2.7	6.9	8.5	0.0
34	0.2	0.8	0.5	4.7	3.0	1.0
51	0.5	0.4	1.7	2.5	9.2	0.5
64	0.1	0.0	0.2	36.9	13.1	8.8
68	3.3	7.5	4.3	51.8	22.6	7.3
85	0.1	0.2	0.2	2.7	0.0	1.2

Table 3.4: C-130 measured vibration amplitudes.

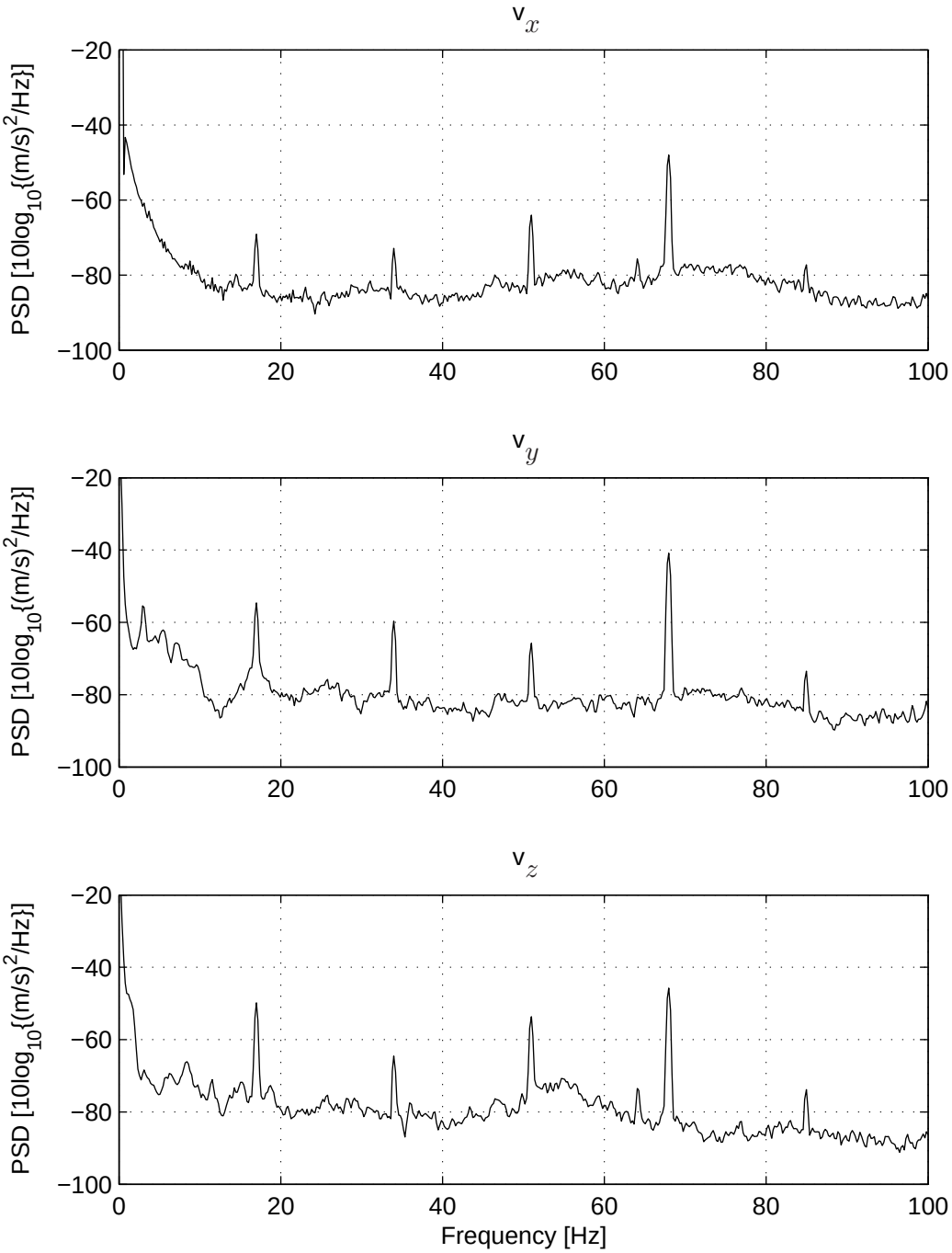

Figure 3.6: C-130 Power spectral densities (PSD) for velocities. N=10000, L=1024, M=512, Blackman window.

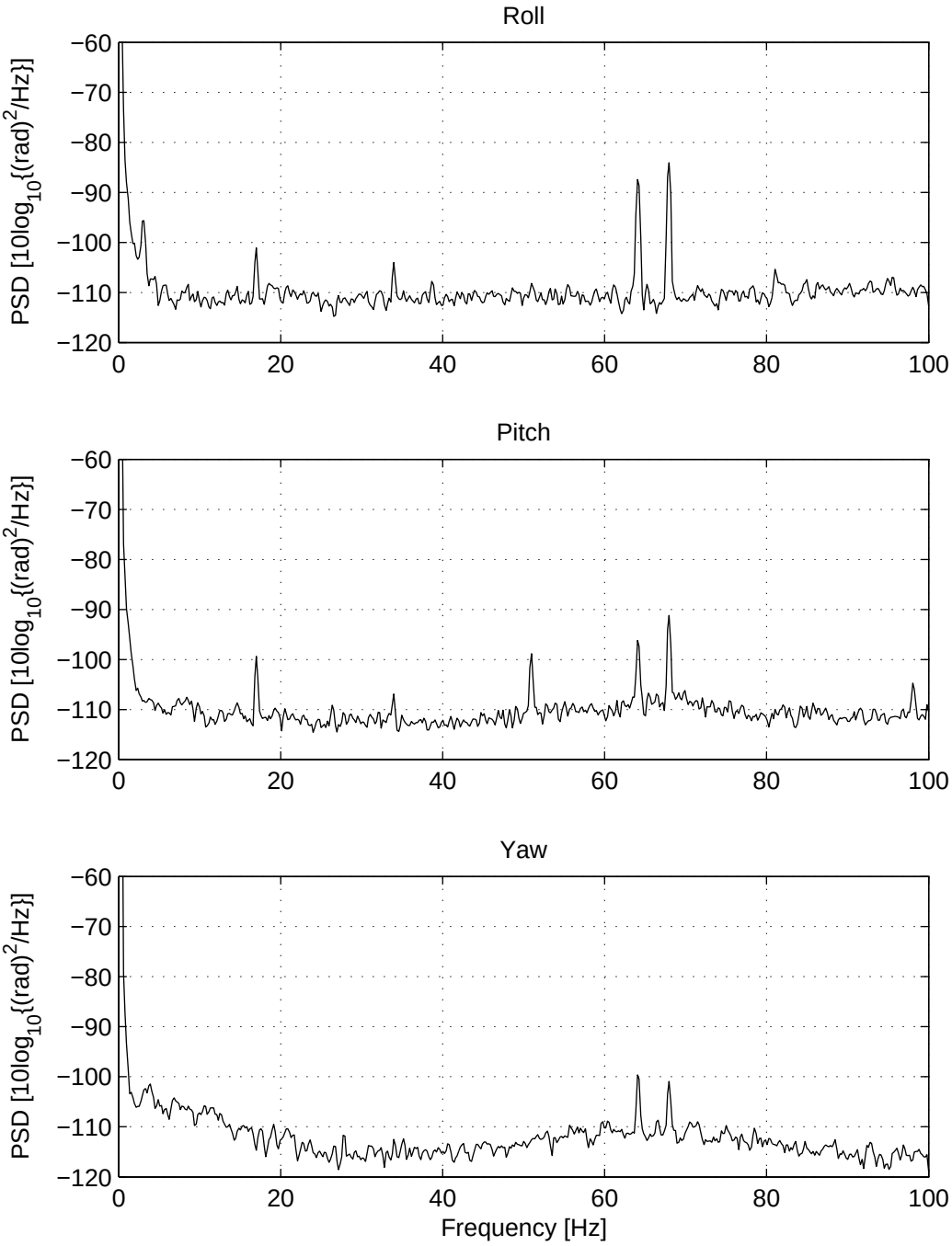

Figure 3.7: C-130 Power spectral densities (PSD) for attitude angles. N=10000, L=1024, M=512, Blackman window.

3.4.2 C-130 PSLR evaluation

In order to evaluate the impact of the measured vibration levels in Table 3.4, the analysis described in section 3.3.5 was performed. The resulting PSLR-values, calculated by using (3.18) and (3.19), are given in Table 3.5. The missing PSLR-values are those where the peak did not rise above the noise floor. PSLR estimates were also calculated from the second set of measurements using the EMISAR EGI (see 3.4). Only velocity data were usable here, and the estimated PSLR values are within a few dB of the values estimated using the KMS EGI.

It must be stressed that the PSLR estimates were made under the assumption that the measured high-frequency motion represents a motion estimation error (see section 3.3.5). This is indeed the case for the aliased vibration at 64 Hz, which will not be present in the SAR data (assuming they are sampled at a frequency $f_{PRF} > 2{\cdot}136$ Hz, which is usually the case). Furthermore, the presence of the aliased vibration in the motion data also implies that an uncompensated vibration will be seen in the SAR data at the unaliased frequency of 136 Hz. Effects of aliasing are treated in section 3.4.3.

The azimuth separation of the sidelobes relative to the mainlobe depends on the spatial frequency of the vibration causing it, according to (2.34). For the fundamental propeller vibration, $f_t = 17$ Hz and with the measured aircraft speed of 350 knots and altitude of 25000 feet, the displacement is $\xi_x = 16$ m, with the SAR parameters of Table 3.3.

Frequency Hz	ξ_x m	PSLR_y dB	PSLR_z dB	PSLR_R dB	PSLR_P dB	PSLR_Y dB
17	16	−54	−49	−60	−59	–
34	32	−65	−70	−64	−68	−77
51	49	−75	−63	−69	−58	−83
64	61	−99	−84	−46	−55	−58
68	65	−52	−57	−43	−50	−60
85	81	−87	−87	−68	–	−76

Table 3.5: C-130 estimated sidelobe displacement and PSLR from vibration. An X-band system with $\lambda = 3.2$ cm, $\theta = 45°$, $h = 25000$ feet, $v = 350$ kts and a leverarm of 1 m is assumed.

From Table 3.5 it is seen that the maximum PSLR induced by velocity vibrations is −49 dB, which is an acceptable value. The maximum PSLR caused by angular vibration is −43 dB, which is also acceptable. This is under the assumption of a leverarm of 1 m, and the cumulative effect of all the vibrations cannot be estimated from these numbers. However, even if all translational and rotational effects at a frequency are added in phase, the maximum PSLR is −36 dB, which, although above the design goal of the SAR++ criteria (see the chapter introduction) is acceptable in most SAR systems. For L- and C-band systems, the PSLR will be below −40 dB.

To illustrate the possible cumulative effects of the measured vibrations, a point target simulation was made, illustrated in Figure 3.8. In this simulation, it was assumed that all vibrations above 10 Hz were in effect residual motion errors, so a hypothetical SAR point target phase history was generated using a subset of the measured

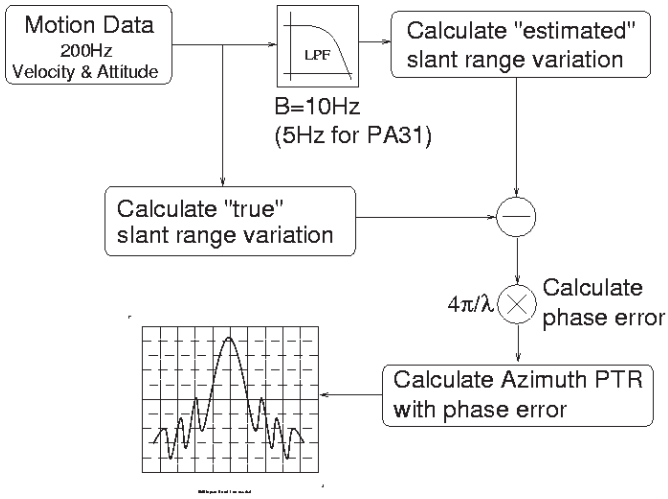

Figure 3.8: Point target simulation with the assumption that all motion above 10 Hz is a residual motion error.

motion data, (v_x, v_y, v_z, Y, P, R), low-pass filtered to a 10 Hz bandwidth. The chosen subset corresponds to the length of a single aperture, with the SAR parameters from Table 3.3. This simulated signal history was then phase corrected using the non-filtered version of the motion data and focused. In this way, the measured motion signal above 10 Hz is interpreted as motion estimation error. A leverarm, $\boldsymbol{d}^{body} = (1/\sqrt{3}\text{ m}, 1/\sqrt{3}\text{ m}, 1/\sqrt{3}\text{ m})^T$, was assumed, since in a high-vibration environment, a short distance between motion sensor and SAR antenna is critical [20]. The resulting impulse response can be seen on Figure 3.9. It is seen from the figure that the simulated PSLR is below -40 dB for all sidelobes, with the two largest pairs at -42 dB and -45 dB. These are due to the 68 Hz and 64 Hz (136 Hz aliased) vibrations, respectively, and caused by the roll angular vibration working through the leverarm. If instead a leverarm $d = (1/\sqrt{3}\text{ m}, 1/\sqrt{3}\text{ m}, -1/\sqrt{3}\text{ m})^T$ is selected these two peaks are reduced by more than 10 dB. This is in agreement with (3.17), since $\cos(45°) = \sin(45°)$.

Summing up, the effects of the measured C-130 vibrations on the SAR impulse response seem to be within acceptable limits, i.e. below -40 dB. It can be briefly noted that sidelobes consistent with a 17 Hz-vibration have actually been seen in focused SAR data acquired from a C-130 [19, 20]. This was in an X-band system, and the sidelobe level was within the acceptable limits.

3.4.3 Aliasing of motion data

Ideally, the motion sensor input bandwidth (e.g. physical gyro or accelerometer bandwidth) should be less than or equal to half the INU sampling rate to avoid aliasing. In this case, the residual motion error resulting from an out-of-band vibration would only be the actual physical vibration seen in the SAR data. However, as was seen in section 3.4.1, a high-frequency motion signal can be aliased to a lower frequency due to the motion sensor sampling. Since the EGI measures translational accelerations and rotational attitude rates, accelerations must be integrated twice to obtain displacement, and attitude rates integrated once to obtain attitude. An acceleration sinusoidal component a_k at frequency $f_{t,k}$ gives rise to a displacement

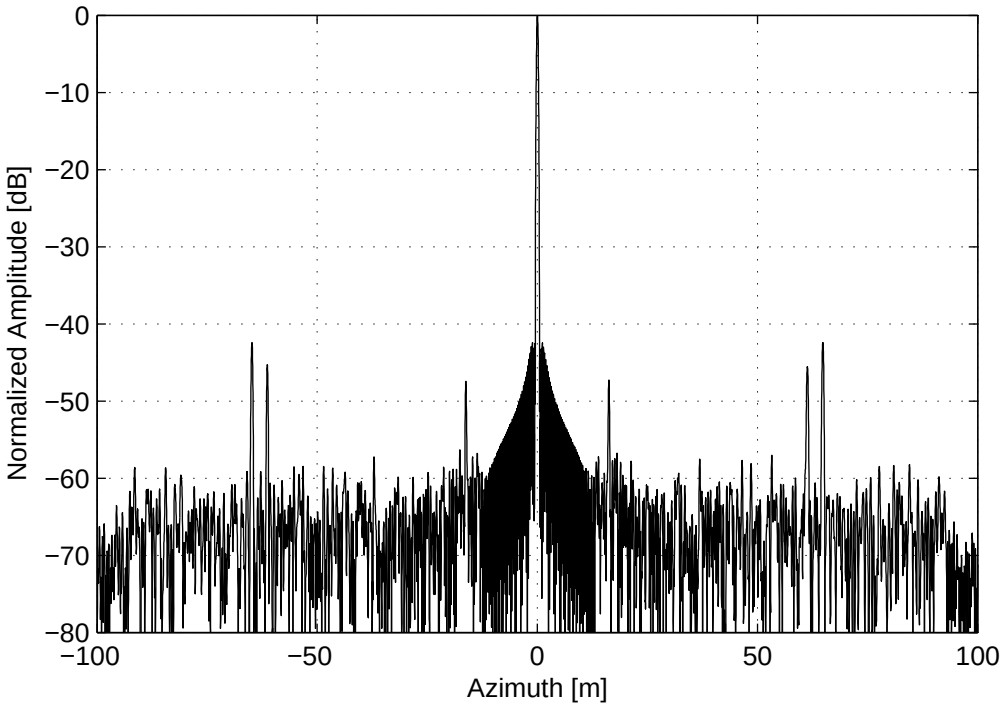

Figure 3.9: Simulated C-130 azimuth impulse response with vibration errors.

given by:

$$y_k = \int\int a_k cos(2\pi f_{t,k} t) dt^2 = -\frac{a_k cos(2\pi f_{t,k} t)}{(2\pi f_{t,k})^2} \tag{3.20}$$

If the acceleration signal is undersampled so that $f_{t,k}$ is aliased to f_A, the displacement estimated from the motion data is:

$$y_A = \int\int a_k cos(2\pi f_A t) dt^2 = -\frac{a_k cos(2\pi f_A t)}{(2\pi f_A)^2} \tag{3.21}$$

The aliased signal amplitude, y_A, is larger than the amplitude of the original signal by a factor of $(f_{t,k}/f_A)^2$. Likewise, aliasing of the attitude rate signal or the velocity signal leads to an increase in amplitude of $(f_{t,k}/f_A)$. Thus, an in itself insignificant out-of-band vibration can, through aliasing, result in an error signal of significantly larger amplitude than the unaliased signal. This could lead to unacceptable sidelobe levels. However, the highest sidelobe levels will also be associated with the lowest aliased frequency. If the aliased vibration period becomes longer than the synthetic aperture duration, the sidelobes will fall within the mainlobe. In this case, the phase error should be treated as a low-frequency phase error (see section 2.3.1).

To illustrate the potential effects of aliasing, it is examined what happens if the EGI 50 Hz data are used for motion compensation instead of 200 Hz data. This excercise is not purely hypothetical, since for example EMISAR collects only the EGI 50 Hz data for SAR focusing. It is important to note here, that the EGI integrates rotation rates and accelerations internally at 200 Hz. Attitude rates and accelerations in the band from 0-100 Hz will thus be integrated correctly to obtain attitude and velocity. However, the integration of velocity to obtain position will be performed at 50 Hz, causing aliasing of vibrations above 25 Hz. This could be avoided if the 50 Hz EGI

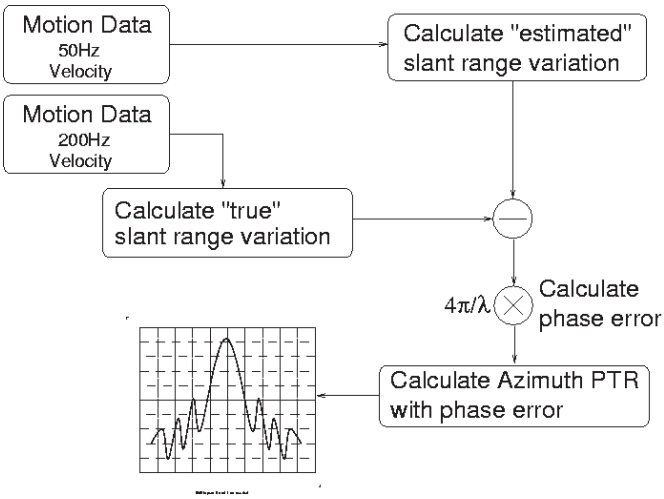

Figure 3.10: Simulation of 200 Hz to 50 Hz aliasing

output data were low-pass filtered before decimation from 200 Hz to 50 Hz, but this is not the case.

A simulated SAR point target phase history was generated using the collected 200 Hz velocity data and the SAR system parameters of Table 3.3. This simulated signal was then phase corrected using the 50 Hz velocity data also available from the EGI, and refocused. The principle is illustrated in Figure 3.10. The resulting phase error and impulse response is shown on Figure 3.11. Note that attitude data were not used in this simulation, since they are not integrated after the 50 Hz aliasing.

From Figure 3.11 we see that the phase error from aliasing causes close-in sidelobes in the impulse response of approximately -26 dB. This is not acceptable in most SAR systems. The phase error is caused by the 51 Hz vibration (see Figure 3.6) being aliased to 1 Hz by the 50 Hz motion sampling. Thus the velocity integration introduces a 1 Hz sinusoidal with 50 times the original vibration amplitude. The sidelobe-to-mainlobe separation is 0.9 m, which is consistent with (2.34) and the measured along-track velocity of 180 m/s.

The point target simulation was also performed using SAR parameters like those of the EMISAR C-band configuration (i.e. $\lambda = 5.66$ cm, $\sigma_x = 1.5$ m). In this case, since the aperture is shorter, the phase error becomes almost linear, causing only a slight displacement of the impulse response.

3.5 Piper PA31 measurements

3.5.1 Motion spectra

The motion spectra estimated for the Piper measurements are shown on Figures 3.12 and 3.13. Only 50 Hz data were available here, and 5000 samples were used in the motion spectrum estimation, corresponding to 100 seconds of data.

Analysing the velocity spectra, it is seen that the largest velocity vibration is in the along-track velocity. However, this does not affect the SAR focusing. In all three velocity directions, peaks are seen at 6.25 Hz, 12.5 Hz, 18.75 Hz, and 25 Hz. The

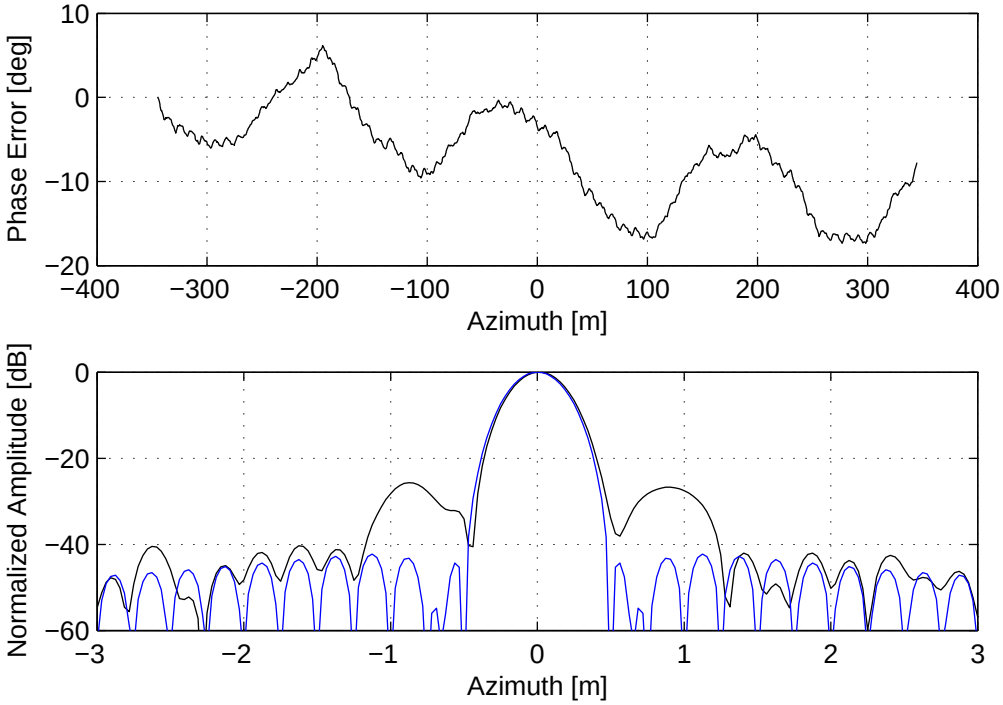

Figure 3.11: Phase error and impulse response with aliasing for an X-band system with 25 cm azimuth resolution. Blue curve is impulse response with no phase error.

shape of the 6.25 Hz and 12.5 Hz peaks suggest that they are actually several peaks with narrow spacing, indicating aliasing. For the attitude measurements, the pitch parameter shows the strongest peaks, whereas there is only a very weak 12.5 Hz peak in the yaw parameter. Also in the attitude parameters, the 6.25 Hz and 12.5 Hz peaks seem to actually be several peaks. It was attempted to separate the peaks by using a longer data window in the power spectrum estimation, but this did not succeed.

Above 5 Hz, the noise floor in the velocity spectra is located at approximately -75 dB/Hz. This is 3 dB higher than expected from the EGI nominal velocity jitter (see section 3.4.1), which is equivalent to a single-sided noise density of -78 dB/Hz with the 50 Hz sampling. For the attitude parameters, the quantization noise has a single sided density of -105 dB/Hz which is in agreement with the observed attitude spectra.

The peak positions are most likely related to the propeller RPM, but since this is not known, guesses must be made. This is complicated by the fact that the EGI operates internally at 200 Hz. Thus, a vibration above 100 Hz will be aliased first by the 200 Hz sampling. If the aliased vibration frequency falls above 25 Hz, it will again be aliased by the 50 Hz sampling of the EGI output data that has been used in the PA31 measurements. Comparing the observed frequencies with the typical RPM operating range for the Piper PA31, the most likely propeller rate candidates are 1875 RPM=31.25 Hz, or 2625 RPM=43.75 Hz. Of these, the former is the most likely, since the specified maximum continuous operating RPM for the Piper is 2575 RPM. Also, the low RPM is consistent with the fact that the measurements were taken at a speed well below the maximum cruise speed (150 knots compared to 200 knots). With an RPM of 1875 and the aliasing described above, the aliased

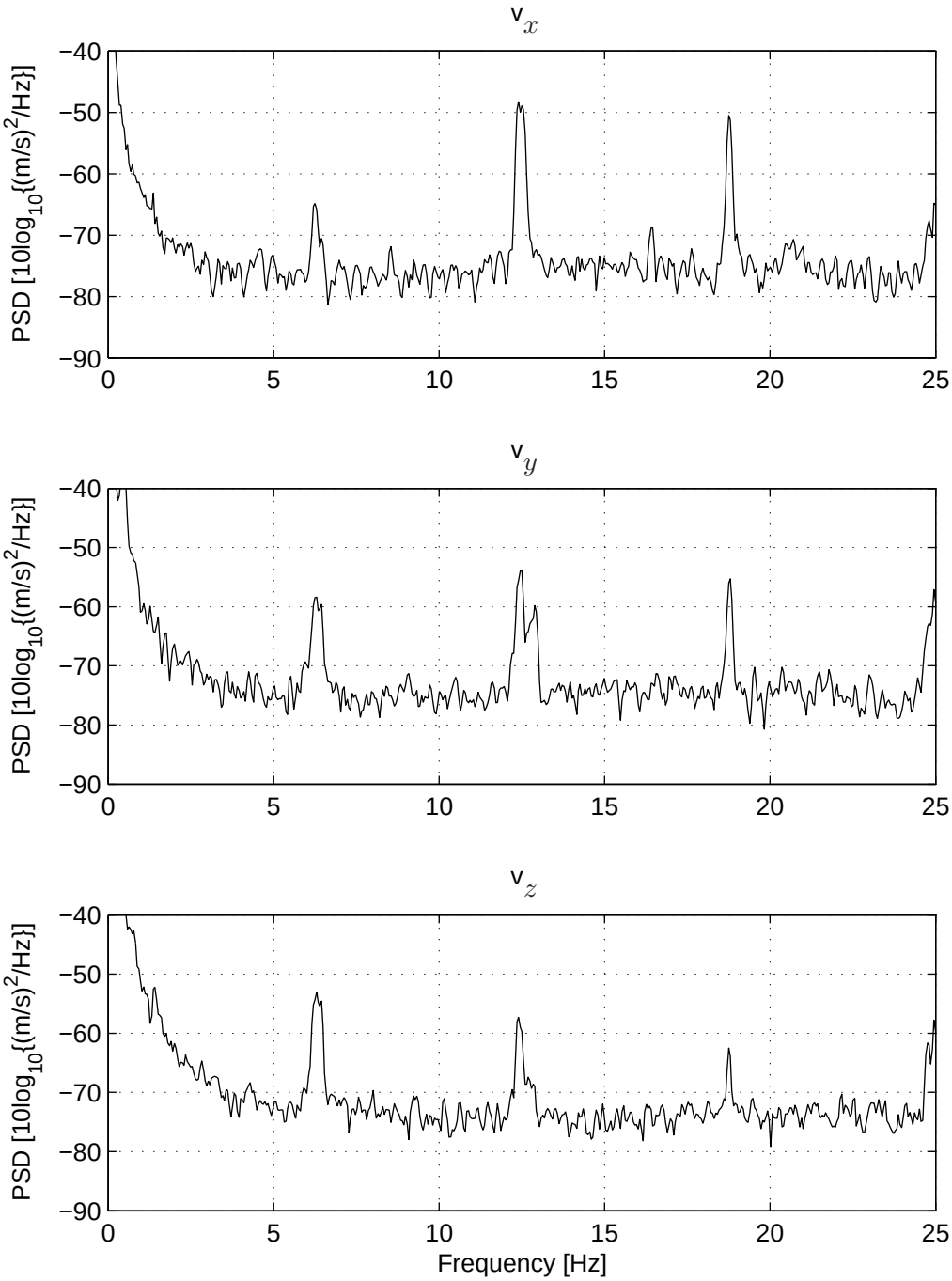

Figure 3.12: Piper PA31 power spectral densities (PSD) for velocities. N=5000, L=1024, M=512, Blackman window.

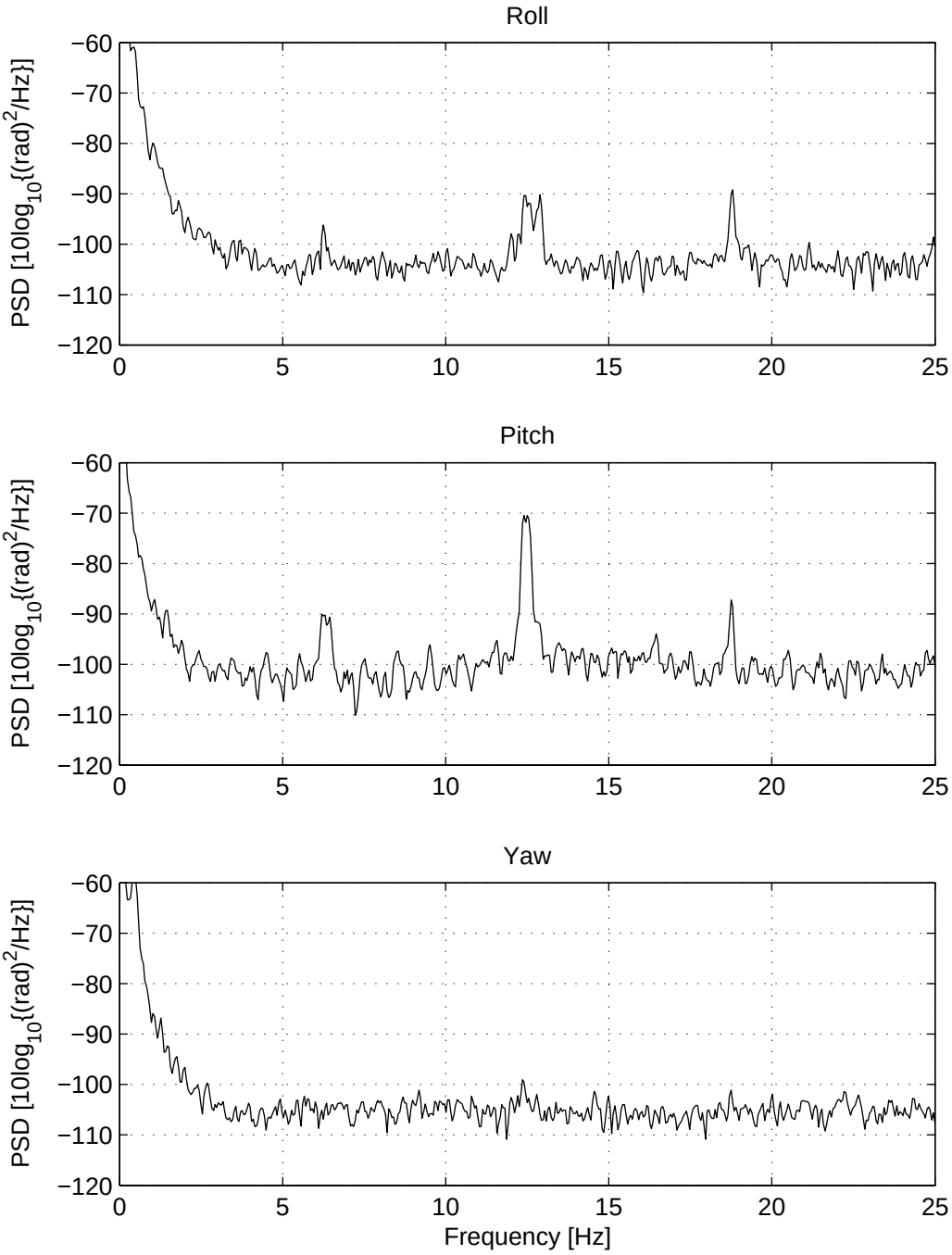

Figure 3.13: Piper PA31 power spectral densities (PSD) for attitude. N=5000, L=1024, M=512, Blackman window.

propeller harmonics will be located at the frequencies in Table 3.6. The 8^{th} harmonic will be aliased to 0 Hz, so it will not be discernible from the non-aliased low-frequency motion.

Frequency [Hz]	Harmonics Aliased to Frequency
6.25	3^{rd} (93.75 Hz) & 5^{th} (156.25 Hz)
12.5	2^{nd} (62.5 Hz) & 6^{th} (187.5 Hz)
18.75	Fundamental (31.25 Hz), 7^{th} (218.75 Hz) & 9^{th} (281.25 Hz)
25.0	4^{th} (125 Hz)

Table 3.6: Aliased harmonics of PA31 propeller frequency at 1875 RPM. The harmonics have been aliased first by 200 Hz sampling and then by 50 Hz sampling.

The shape of the 6.25 Hz and 12.5 Hz peaks are explained by the fact that two harmonics actually alias to those frequencies. Also, the 3^{rd} and 6^{th} harmonics are the fundamental and second harmonics of the blade frequency, since the PA31 has three-blade propellers. In the C-130 data, the strongest peaks were observed at the blade frequency in both the velocity and attitude data. If this was the case here, the largest peak should be at 6.25 Hz. The reason that the 12.5 Hz peak is the largest is probably that the 6^{th} harmonic (=second blade harmonic) is aliased to 12.5 Hz already in the initial 200 Hz sampling before acceleration integration. The fundamental and 3^{rd} blade harmonics are acceleration-integrated at 93.75 Hz (unaliased) and 81.25 Hz (aliased) respectively. The higher frequency leads to relatively smaller amplitudes of the integrated acceleration vibrations (see section 3.4.3).

3.5.2 PA31 PSLR Evaluation

Since all the peaks are aliased and some fall close to each other, it is difficult to estimate the power content of the individual peaks. If close-lying peaks are treated as one peak, the vibration amplitudes in Table 3.7 are observed. Converting the vibration amplitudes to PSLR (see sections 3.3.5 and 3.4.2), the results in Table 3.8 are seen.

Frequency Hz	v_x mm/s	v_y mm/s	v_z mm/s	R μrad	P μrad	Y μrad
6.25	0.3	1.0	1.4	9.0	21.5	0.0
12.50	2.5	1.5	1.0	24.9	191.9	4.6
18.75	1.6	0.9	0.3	16.2	20.6	2.4

Table 3.7: PA31 measured vibration amplitudes

We see here that the only critical vibration is the angular vibration in the pitch parameter aliased to 12.5 Hz. This leads to a PSLR of -31 dB if working through a 1 m leverarm component. This is larger than the design goal of -40 dB in the SAR++ requirements (see the chapter introduction). If the 200 Hz motion data were used, the fundamental, 2^{nd}, and 3^{rd} propeller harmonics would not be aliased, but the 6^{th} propeller harmonic would still be aliased to 12.5 Hz. Thus, if a significant part of the power seen in the 12.5 Hz peak in the pitch spectrum comes from the aliased 6^{th}

Frequency Hz	ξ_x m	PSLR$_y$ dB	PSLR$_z$ dB	PSLR$_R$ dB	PSLR$_P$ dB	PSLR$_Y$ dB
6.25	1.9	−49	−46	−58	−51	–
12.50	3.8	−51	−55	−49	−31	−64
18.75	5.7	−60	−68	−53	−51	−70

Table 3.8: PA31 estimated sidelobe displacement and PSLR from vibration. An X-band system with λ =3.2 cm, θ = 45°, h=1000 m, and a leverarm of 1 m is assumed.

propeller harmonic, there could still be unacceptable sidelobes at $\xi_x = 3.8$ m with the given system parameters and leverarm. To illustrate the possible cumulative effects of these aliased vibrations, a point target simulation similar to the one in section 3.4.2 was made. The SAR parameters used were the same as in the C-130 measurement, except that an altitude of 1000 m and a velocity of 150 knots was assumed, as the vibration data were acquired under these flight conditions. The simulated phase history was generated using the motion data low-pass filtered to a 5 Hz bandwidth, but phase corrected by the non-filtered motion data before focusing. The resulting impulse response is presented on Figure 3.14. Here it is seen that the PSLR associated with the 12.5 Hz peak is −32 dB, whereas the cumulative effects of the 6.25 Hz vibrations amount to a PSLR of −37 dB.

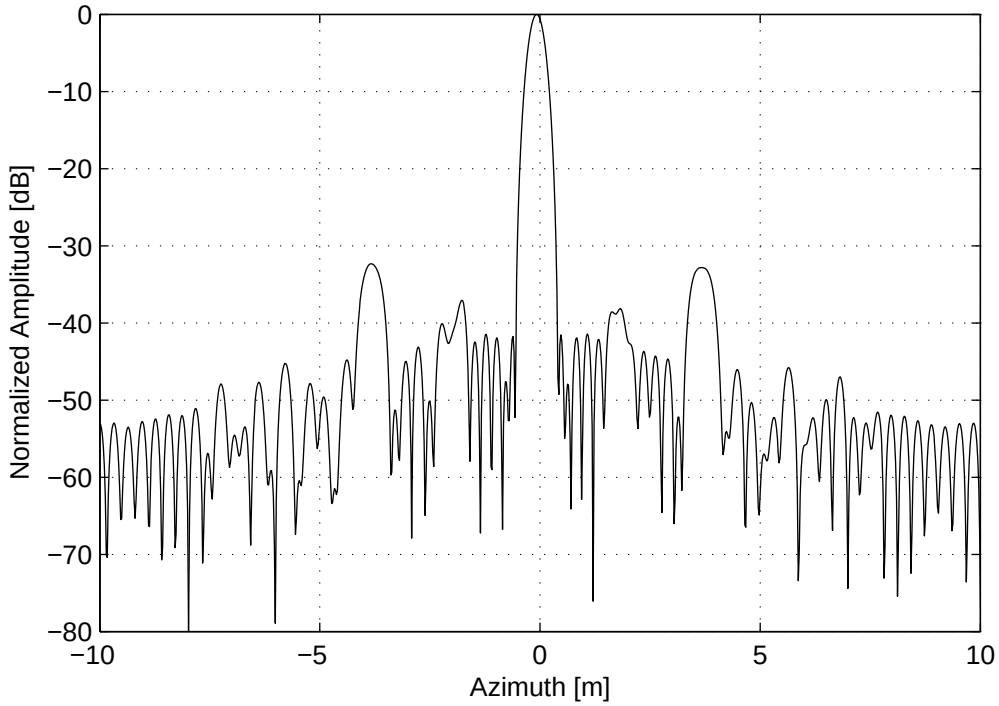

Figure 3.14: Simulated PA31 azimuth impulse response with vibration errors.

In estimating the PSLR values of Table 3.8 and Figure 3.14, it was assumed that the 50 Hz motion data are used for motion compensation, unfiltered. With the 50 Hz sampling, all of the observed motion signal above 5 Hz is actually aliased and can be removed by a low-pass filter. Harmonics that are aliased to low frequencies where

there is already physical motion (e.g. the 8^{th} harmonic aliased to 0 Hz), however, cannot be filtered this way. Either way, the actual physical vibrations will be left uncompensated, and cause sidelobes in the SAR data. Their level, however, will likely be equal to or smaller than the levels seen in Table 3.8 (See also section 3.4.3).

3.6 Gulfstream GIII measurements

3.6.1 Motion spectra

For reference, motion spectra for a Gulfstream GIII jet aircraft are also presented here. They were acquired during an EMISAR flight with the EMISAR EGI. The motion measurements were processed the same way as for the C-130 measurements (see section 3.4.1), and the resulting spectra are shown on Figures 3.16 and 3.17. As mentioned in section 3.2.1, due to a bug, the EMISAR EGI only updates attitude data at 50 Hz, even in the 200 Hz data. Therefore, Figure 3.17 only shows the attitude spectrum up to 25 Hz. However, the velocity spectrum of Figure 3.16 can be directly compared to the C-130 velocity spectrum on Figure 3.6. It is clear that there are no signifcant vibration peaks in the GIII spectra compared to the C-130 spectra. The attitude parameters, especially, show only a noise floor above a few Hz. This noise floor is consistent with the expected quantization noise density of -105 dB/Hz.

A PSLR-evaluation was not made for the GIII data due to the low observed vibration levels. However, a point target simulation, similar to the one in section 3.4.2 was made. The assumed SAR system parameters were the same as for the C-130 case, but only velocity data were used. This is because the attitude data were only available at 50 Hz, and furthermore, as seen from Figure 3.17, there does not appear to be any angular motion signal above a few Hz. The simulated phase history was, as for the C-130 point target simulation, generated using the motion data low-pass filtered to a 10 Hz bandwidth but phase corrected using the non-filtered motion data. The simulated impulse response is seen on Figure 3.15. It is seen that there are practically no discernable sidelobes.

3.7 Discussion

From the analysis in the preceding section it seems clear that the actual propeller-induced cross-track vibrations - which will appear as small sinusoidal variations in the SAR signal phase - will not lead to unacceptable sidelobes if left uncorrected. This is under the assumption of a small leverarm of less than 1 m between motion sensor and SAR antenna. If the motion sensor sampling frequency is too low, high-frequency vibrations might be aliased to lower frequencies before integration in the INU, and this will result in spurious vibrations in the motion data not reflected by the SAR data. That is worse, since the integration of the aliased sinuosidal is performed at a lower frequency. This will in turn lead to a higher level of the spurious signal compared to the signal that caused it. Ideally, the INU should perform anti-alias filtering on its sensor inputs, which could be achieved by an initial oversampling and digitial filtering of the acceleration and gyro outputs. Actually, as described in section 3.1.2, the sensor signals are initially oversampled by a factor of 6 (i.e.

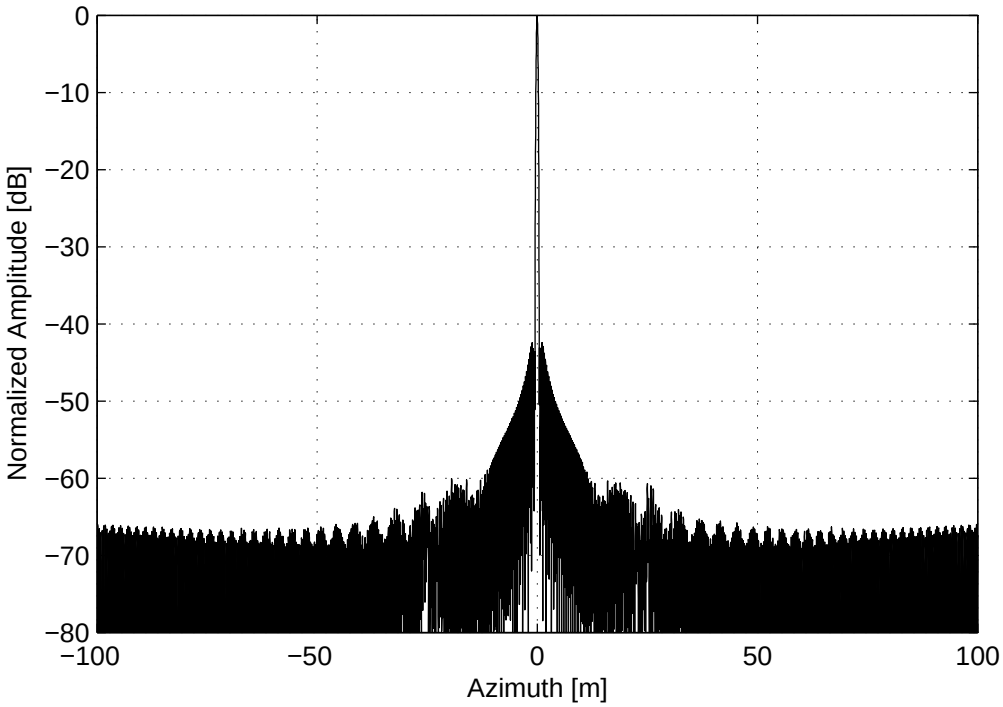

Figure 3.15: GIII Simulated impulse response with vibration errors.

1200 Hz), but aliasing was seen in the 200 Hz C-130 data, indicating that aliasing is not fully suppressed internally in the EGI. It is also clear that the 50 Hz velocities output together with position data are not lowpass-filtered before decimation from 200 Hz. This suggests that for propeller aircraft systems, the full bandwidth should be used. As was shown in 3.4.3, the C-130 has a propeller harmonic of 51 Hz, which will alias to 1 Hz if the 50 Hz motion data are used. The resultant sidelobes seem not to be significant for L- and C-band systems as they fall in the mainlobe. However for a 25 cm resolution X-band system, the sidelobes will separate from the mainlobe, deteriorating the image quality, as illustrated in Figure 3.11.

For the PA31 Navajo case, all high-frequency motion above 5 Hz came from the 50 Hz aliasing, but even with 200 Hz samling, aliasing could still occur, as shown in section 3.5.2. In this case, the prudent approach is to lowpass-filter the motion data before using them in motion compensation.

As a minimum precaution, before mounting a SAR sensor on a propeller aircraft, the propeller rotation frequency should be compared to the motion sensor sampling frequency to see if potential aliasing problems could occur. If this is the case, the propeller rotation rate might be changed during SAR imaging, but for some aircrafts, such as the C-130, the propeller rotation rate is tightly fixed. In this case, the motion sensor might be mounted on a springs or a rubber mat to reduce high-frequency vibrations, but this might be difficult to do in a way that does not affect the measurement of lower-frequency motion.

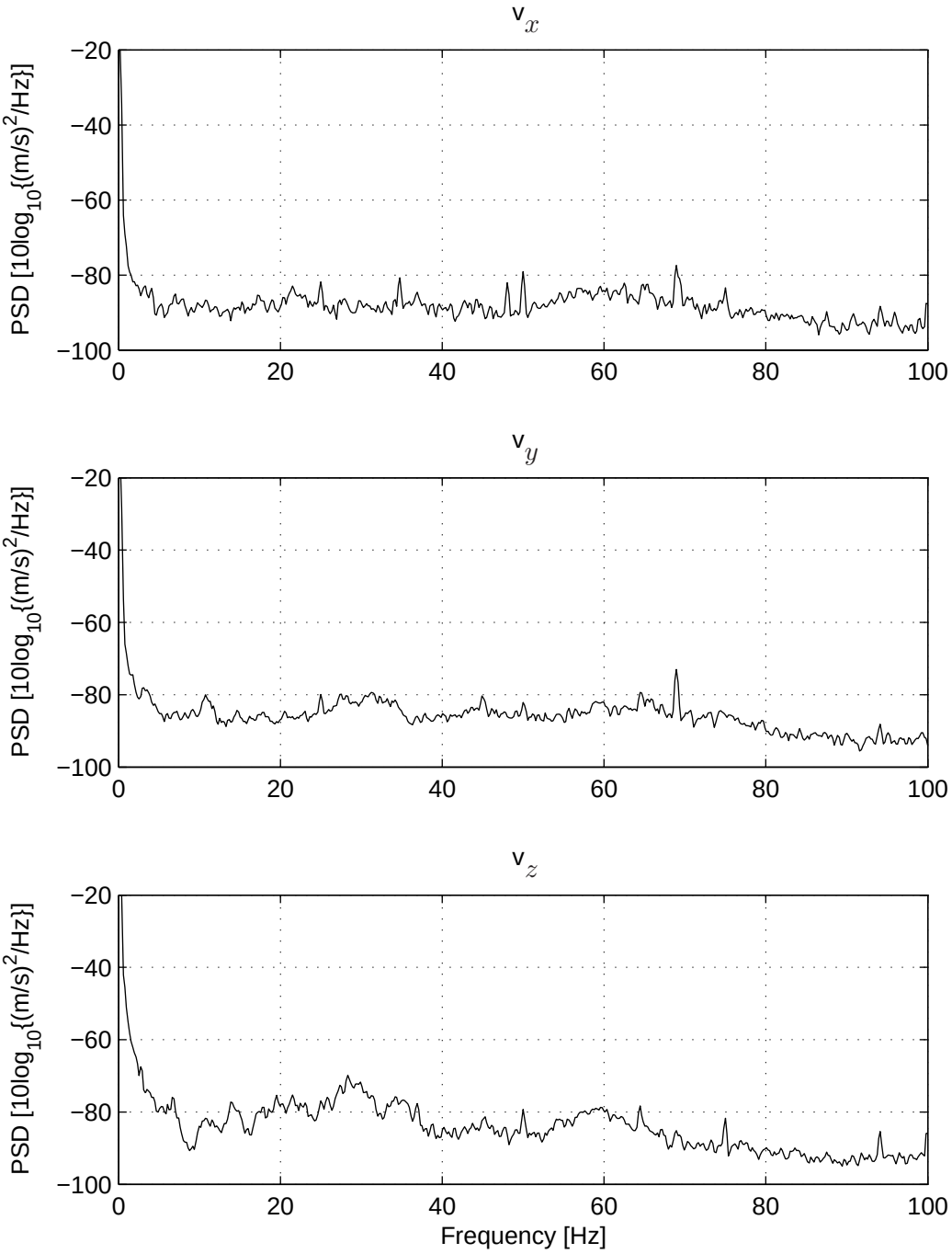

Figure 3.16: Gulfstream GIII power spectral densities (PSD) for velocities. N=10000, L=1024, M=512, Blackman window.

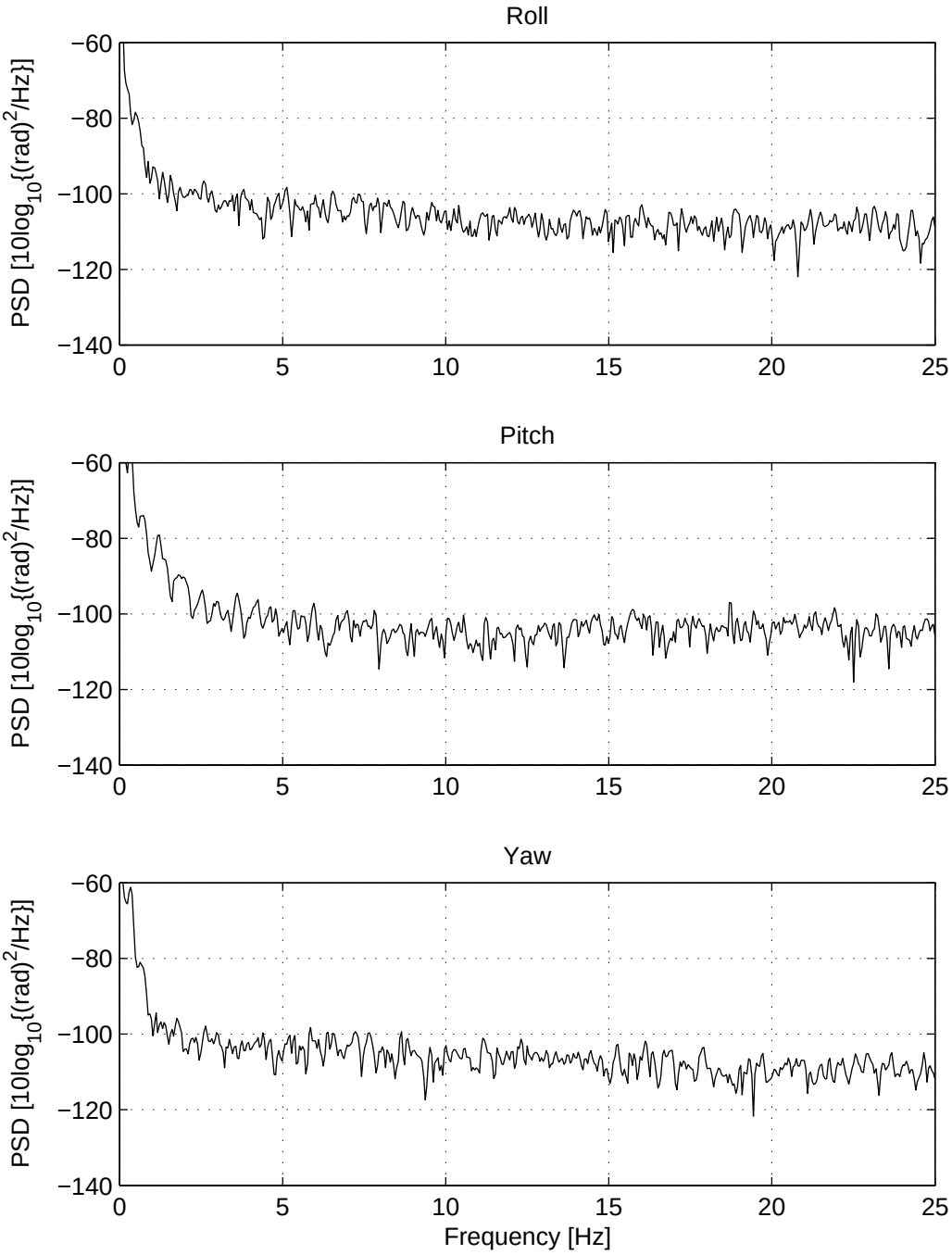

Figure 3.17: Gulfstream GIII Power Spectral Densities (PSD) for attitude. N=10000, L=1024, M=512, Blackman window.

Chapter 4

Motion Errors in Repeat Track Interferometry

In SAR interferometry, the sensitivity of the SAR image phase to small range displacements is utilised by forming the phase difference between images acquired from separate tracks. This phase difference is proportional to the range displacement between the images. Depending on the interferometric baseline, the range displacement is sensitive to scene topography, and the observed interferometric phase can be used to calculate a digital elevation model (DEM) of the imaged scene. Digital elevation models are typically generated using single-pass interferometry, where the SAR images are acquired simultaneously from two antennas mounted on the same aircraft. This reduces baseline errors, since a large part of the motion estimation errors will be common to each antenna, and thus not affect the baseline. The baseline dimensions are, however, limited by the physical constraints of the aircraft.

In repeat-track interferometry (RTI), the SAR images used to form an interferogram are acquired in separate passes. In this case, the interferometric phase also becomes sensitive to atmosphere changes and temporal scene changes between the two acquisitions. Atmospheric effects are a nuisance, but the fact that the interfeometric phase is sensitive to temporal scene displacements can be used in geophysical applications, such as change mapping in glaciology [21], landslide detection, and earthquake mapping. In this case, the baseline must be known with an accuracy a fraction of the size of the scene displacements. In topography mapping, RTI allows for larger baselines than in the single-pass case, allowing an increased sensitivity to topography. However, the baseline depends on the actual tracks flown by the sensors, and the relative baseline accuracy (absolute baseline accuracy divided by baseline length) has to be on the order of the required height accuracy relative to the range to the target.

In this chapter, the basic principles of SAR interferometry are briefly reviewed, followed by a description of existing algorithms for estimating and correction differential motion errors.

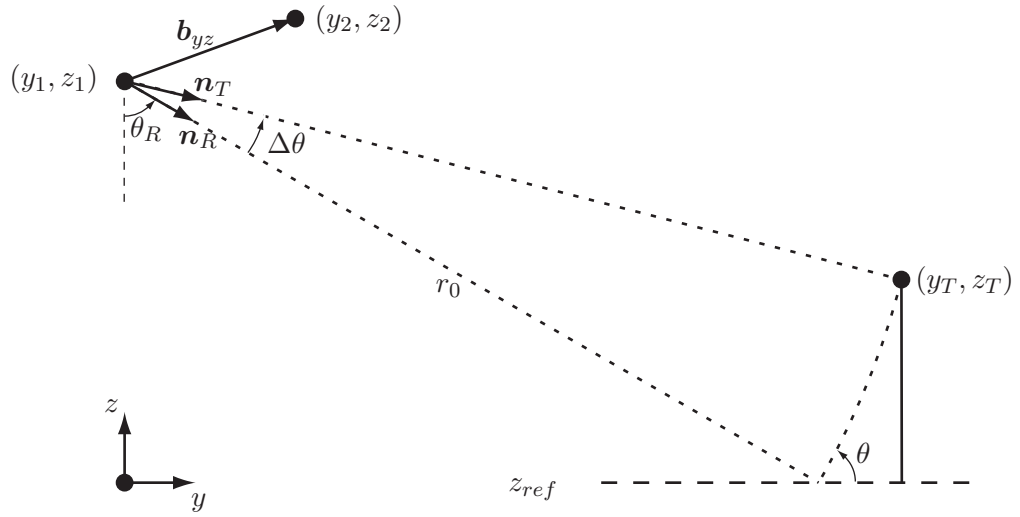

Figure 4.1: SAR interferometry principle.

4.1 Basic principles of interferometry

4.1.1 Geometry

The basic principle of SAR interferometry is illustrated on Figure 4.1. The target is observed from the tracks 1 and 2, separated by the interferometric baseline

$$\boldsymbol{b} = \begin{bmatrix} b_x \\ b_y \\ b_z \end{bmatrix} = \widehat{\boldsymbol{b}} + \boldsymbol{b}_\epsilon = \Delta\boldsymbol{p}_2 - \Delta\boldsymbol{p}_1 \tag{4.1}$$

where $\widehat{\boldsymbol{b}} = \Delta\widehat{\boldsymbol{p}}_2 - \Delta\widehat{\boldsymbol{p}}_1$ is the baseline estimated from the motion data and $\boldsymbol{b}_\epsilon = \Delta\boldsymbol{p}_{2,\epsilon} - \Delta\boldsymbol{p}_{1,\epsilon}$ is the differential baseline error due to motion estimation errors. It is assumed for the present discussion that track 1 is the master track, and that track 2 data are motion compensated to the master track. The along-track baseline component, b_x, is ideally zero, but as long as it is smaller than a fraction of the azimuth resolution, it has negligible impact on the interferometric phase. Neglecting motion errors (these are treated in section 4.2) the interferometric phase depends only on the estimated cross-track baseline

$$\widehat{\boldsymbol{b}}_{yz} = \begin{bmatrix} \widehat{b}_y \\ \widehat{b}_z \end{bmatrix} \tag{4.2}$$

Motion compensation is performed with the assumption of a reference target height z_{ref}. The actual target height is $z_T = z_{ref} + h_T$, leading to the interferometric range shift

$$\Delta r_{topo,IF} = \Delta r_{topo,2} - \Delta r_{topo,1} = -\widehat{\boldsymbol{b}}_{yz} \cdot (\boldsymbol{n}_T - \boldsymbol{n}_R)$$

where $\Delta r_{topo,1}$ and $\Delta r_{topo,2}$ given by (2.20). The range shift is more conveniently calculated using the look angle, $\theta = \theta_R + \Delta\theta$:

$$\Delta r_{topo,IF} \approx -\widehat{\boldsymbol{b}}_{yz} \cdot \frac{\partial \boldsymbol{n}(\theta)}{\partial\theta}\frac{\partial\theta}{\partial z} h_T = -(\widehat{b}_y \cos\theta_R + \widehat{b}_z \sin\theta_R)\frac{1}{r_0 \sin\theta_R} h_T \tag{4.3}$$

The interferogram of the two focused SAR images, u_1 and u_2, is formed by multiplying u_1 by the complex conjugate of u_2. Thus the interferometric phase shift due to topography is given by

$$\phi_{topo} = \phi_{topo,1} - \phi_{topo,2} = -\frac{4\pi}{\lambda}(\Delta r_{topo,1} - \Delta r_{topo,2}) = \frac{4\pi}{\lambda}\Delta r_{topo,IF} \tag{4.4}$$

The interferometric baseline vector can also be resolved in a parallel and a perpendicular baseline component. The parallel baseline is the projection of the baseline on the nominal line-of-sight direction:

$$b_{\parallel} = \widehat{\boldsymbol{b}}_{yz} \cdot \boldsymbol{n}_R = \widehat{b}_y \sin\theta_R - \widehat{b}_z \cos\theta_R \tag{4.5}$$

and the perpendicular baseline is the component of the baseline that is perpendicular to the nominal line-of-sight direction:

$$b_{\perp} = \widehat{b}_y \cos\theta_R + \widehat{b}_z \sin\theta_R \tag{4.6}$$

The inversion of the interferometric phase to obtain the absolute terrain requires precise knowledge of the actual baseline. From (4.3), the inversion of the observed interferometric range shift to a target height is given by

$$\widehat{h}_T = -\frac{r_0 \sin\theta_R}{\widehat{b}_y \cos\theta_R + \widehat{b}_z \sin\theta_R}\Delta\widehat{r}_{topo} \tag{4.7}$$

Here, $\widehat{b}_y \cos\theta_R + \widehat{b}_z \sin\theta_R$ is the perpendicular baseline, and $\Delta\widehat{r}_{topo} = (\lambda/4\pi)\widehat{\phi}_{topo}$ is the interferometric range shift due to topography, as estimated from the interferogram phase. A differential baseline error causes an uncompensated range shift, Δr_ϵ, which in turn causes an error on the interferogram phase. The sensitivity of the estimated topography to an uncompensated range shift, r_ϵ is, from (4.7)

$$\frac{\partial\widehat{h}_T}{\partial\Delta r_\epsilon} = -\frac{r_0 \sin\theta_R}{\widehat{b}_y \cos\theta_R + \widehat{b}_z \sin\theta_R} \tag{4.8}$$

The residual range error is multiplied by the ratio of the ground range to the perpendicular baseline. For practical SAR systems, this factor is large, implying a high sensitivity to motion errors.

There are generally two ways to process SAR images to form interferograms [25]. In the first approach, the images are focused to separate reference tracks (master and slave) separated by a nominal baseline. After focusing, the slave image is resampled to the master geometry, and interferograms are formed. The nominal baseline can then be used to invert the interferometric phase. In the second approach, both images are focused to the same reference track, and no resampling is required before interferogram formation. In both case, to accurately invert the interferometric phase to height, the actual baseline at each azimuth postion must be used.

The common reference track approach has the advantage that the images are automatically registered and flattened, so that targets at the reference height have zero interferometric phase. However, with large baselines, and thus large shifts to be motion compensated, both the center-of-aperture assumption (section 2.2.1) and the range spectral shift (section 2.2.2) can affect the focusing quality. Defocusing results in both a phase bias and increased phase variance [23].

4.1.2 Interferometric phase errors

In addition to the topographic phase (4.4), the observed interferogram phase contains contributions from uncompensated motion errors, radar system phase drift, thermal noise, and – when the two images are obtained at different points in time – atmospheric effects, scene displacements and temporal decorrelation. Furthermore, the phase of an observed interferogram is measured modulo 2π, so phase unwrapping and absolute phase determination techniques must be applied to obtain an estimate of the absolute interferometric phase. Thus the observed interferometric phase is:

$$\phi_{IF} = \phi_{topo} + \phi_{motion} + \phi_{drift}\phi_{temporal} + \phi_{noise} + \phi_{atm} + \phi_{disp} + \phi_{wrap} \quad (4.9)$$

In order to use the interferometric phase for topography mapping (ϕ_{topo}) or change mapping (ϕ_{disp}), the remaining terms must be accounted for. The subject of this thesis is the motion error, ϕ_{motion}, which is one of the major effects for airborne SAR systems. Motion errors can both cause phase bias errors, due to uncompensated offsets and defocusing, as well as increased phase variance.

The system phase drift component, ϕ_{drift}, will typically be a low frequency effect resulting in a slowly varying phase bias term, whereas the noise component, ϕ_{noise}, will result in increased phase variance (see section 4.1.3). Compared to satellite SAR systems, airborne systems generally exhibit higher signal-to-noise ratios since they fly at closer range to the imaged scene.

The atmospheric phase term, ϕ_{atm}, which is caused by changes in the atmospheric refractive index between the observations can be a significant contribution to the observed phase, but its effects are difficult to predict, and can affect the entire image as well as isolated areas in the image. They depend on the weather conditions, cloud cover and humidity at the times of acquisition. In [22], atmospheric phase errors in spaceborne SAR interferograms are examined. It is found that the major error source is the localized changes in the refractive index of the troposphere, an effect which is also present for an airborne SAR system. For the examined interferograms, RMS values of the atmospheric phase signal from 0.5 to 3.6 radians at C-band are reported, corresponding to RMS range displacements from 2 mm to 1.7 cm. In the extreme cases local variations equivalent to a displacement of 11 cm were seen, due to thunderstorms. On average, the reported errors are smaller than, but comparable to, the expected motion errors of 5-10 cm with kinematic GPS.

In change mapping, the displacement phase, ϕ_{disp}, is the desired signal, and the topographic contribution must be estimated and removed, either by use of an external elevation model or by forming a differential interferogram using an additional image with a short temporal baseline relative to one of the other two images. In topography mapping, the displacement term is a nuisance, but it can be minimized by using short revisit times.

The temporal decorrelation, ϕ_{temp}, is due to changes in the sub-resolution cell scattering structure between the acquisitions. With long revisit-times, this can for example occur due to seasonal changes in the vegetation layer, but even with short temporal baselines (i.e. minutes), wind conditions may affect the scattering structure of vegetated areas significantly between acquisitions. The temporal decorrelation increases with radar frequency.

The phase wrapping term, ϕ_{wrap}, comes about from the fact that the phase of an

interferogram is given modulo 2π. With the use of phase unwrapping techniques, the problem is reduced to estimating a single phase offset for the entire image. This offset is an integral multiple of 2π and can be estimated using image registration techniques, tie points in the image or an external elevation model.

4.1.3 The complex coherence

Some of the phase terms described in section 4.1.2 can be considered bias effects, but thermal noise in the SAR system, defocusing, misregistration, and temporal and spatial decorrelation also affect the variance of the interferometric phase estimate. These errors can be evaluated by use of the complex coherence. For the complex SAR images u_1 and u_2, the complex coherence, γ is given by

$$\gamma = \frac{E\{u_1 u_2^*\}}{\sqrt{E\{|u_1|^2\} \cdot E\{|u_2|^2\}}} \tag{4.10}$$

A value of $|\gamma| = 1$ implies complete correlation of the two images (zero phase and amplitude variance). The variance of the interferometric phase estimate increases with decreasing coherence, and for $|\gamma| = 0$ the images are completely decorrelated.

The contribution of the different decorrelation effects in to the complex coherence can be summed up by [23]:

$$\gamma = \gamma_{SNR} \cdot \gamma_{defocus} \cdot \gamma_{misreg} \cdot \gamma_{temporal} \cdot \gamma_{spatial} \tag{4.11}$$

Temporal decorrelation occurs when the scene scattering properties change between image acquisitions, for example due to vegetation changes or weather effects. Spatial decorrelation is caused by the fact that different frequency bands of the scene reflectivity function are observed at different incidence angles [24]. Range spectral filtering of the SAR images can remove part of the spatial decorrelation, but the larger the difference in incidence angle, the smaller the band overlap becomes, and total decorrelation occurs when there is zero overlap.

Decorrelation due to misregistration is typically caused by residual motion errors. As shown in section 4.2.1, small cross-track velocity errors can cause large azimuth misregistrations. The effect of a misregistration, δ, in the range or azimuth direction on the interferometric coherence can, with no spectral weighting of the range and azimuth reference functions, be shown to be [23]:

$$\gamma_{misreg} = \mathrm{sinc}(\pi \frac{\delta}{\sigma}), \qquad |\delta| < \sigma \tag{4.12}$$

where $\mathrm{sinc}(x) = \sin(x)/x$[1], δ is the misregistration, and σ is the resolution. Obviously, a misregistration equal to or greater than the resolution cell size causes complete decorrelation.

4.2 Motion errors in interferometry

Residual motion errors in the SAR images used to form an interferogram can have several different effects on the interferogram quality. Motion errors common to both

[1] Note that Bamler uses a different definition of the sinc-function in [23].

images have little effect on the interferogram quality and phase, to the extent that they do not cause defocusing of the individual images. When using kinematic GPS and INU combined, defocusing is typically not a problem. However, differential cross-track motion errors of even a few centimeters can lead to large azimuth misregistrations and terrain height estimation errors. The differential motion error, $\boldsymbol{b}_\epsilon$, is the difference in the individual motion estimation errors:

$$\boldsymbol{b}_\epsilon = \begin{bmatrix} b_{x,\epsilon} \\ b_{y,\epsilon} \\ b_{z,\epsilon} \end{bmatrix} = \Delta\boldsymbol{p}_{2,\epsilon} - \Delta\boldsymbol{p}_{1,\epsilon} \tag{4.13}$$

Methods to estimate motion errors from the differences between the images can only detect the differential error, and therefore it is customary to assume that the master track motion data are error-free and attribute the entire motion error to the slave track. Another approach is to attribute 50% of the error to each image. Furthermore, without knowledge of the scene topography or access to tie points, methods to estimate motion errors from the differences between the images can generally only estimate the part of the differential error that changes along the image. This is due to the fact that a constant differential error results only in a constant (but range dependent) range misregistration and no azimuth misregistration. Thus it is indistinguishable from a range shift caused by scene topography. For example, a constant rotation of the baseline is indistinguishable from a rotation of the scene [21].

4.2.1 Impact of motion errors

Residual motion errors in SAR are typically slowly varying if they are caused by for example INU drift. For the following derivation, it is assumed that the motion error variation is so slow that, for a target located at a nominal along-track position x_0, the differential cross-track motion error can be considered linear within the synthetic aperture centered on x_0:

$$\boldsymbol{b}_{yz,\epsilon}(x - x_0) \approx \boldsymbol{b}_{yz,\epsilon}(x_0) + (x - x_0) \left.\frac{\partial \boldsymbol{b}_{yz,\epsilon}}{\partial x}\right|_{x=x_0} \tag{4.14}$$

where $\boldsymbol{b}_{yz,\epsilon}$ is the cross-track differential motion error:

$$\boldsymbol{b}_{yz,\epsilon} = \begin{bmatrix} b_{y,\epsilon} \\ b_{z,\epsilon} \end{bmatrix} \tag{4.15}$$

Futhermore it is assumed that the along-track differential motion error can be considered constant within an aperture:

$$b_{x,\epsilon}(x - x_0) \approx b_{x,\epsilon}(x_0) \tag{4.16}$$

Attributing the entire differential motion error to the slave track, the differential motion error can be interpreted as a residual motion error on the slave track. The situation is illustrated in Figure 4.2, looking down into the slant range plane. For a target at (x_0, r_0), the slant range plane is the plane parallel to the reference track and the target line-of-sight vector $\boldsymbol{n}_T(x_0, r_0)$. The residual motion error on the slave track results in the target being focused to a track, (x', r'), which is translated

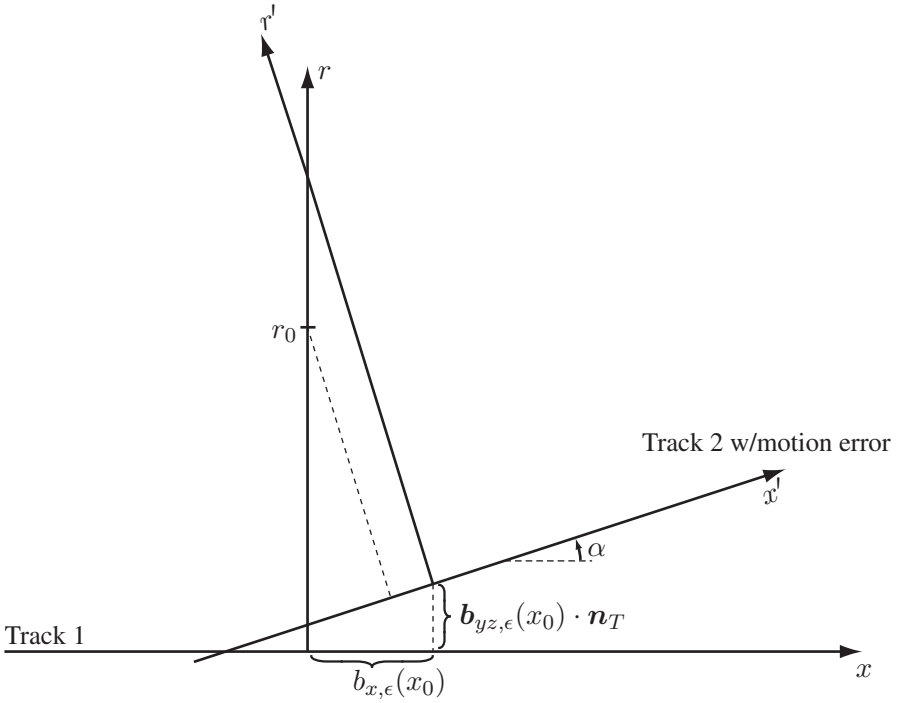

Figure 4.2: Effect of a differential motion error in interferometry, looking down into the slant-range plane. The (x, r) system is a local reference system with origin at $(x_0, 0)$ in reference track coordinates, where x_0 is the nominal target along-track position.

and rotated relative to a local reference system (x, r). This reference system has its origin at $(x_0, 0)$ in master track coordinates (which are also the reference track coordinates). The transformation from (x, r) coordinates to (x', r') coordinates is, from plane analytic geometry, given by

$$\begin{bmatrix} x' \\ r' \end{bmatrix} = \begin{bmatrix} \cos\alpha & \sin\alpha \\ -\sin\alpha & \cos\alpha \end{bmatrix} \begin{bmatrix} x - b_{x,\epsilon}(x_0) \\ r - \boldsymbol{b}_{yz,\epsilon}(x_0) \cdot \boldsymbol{n}_T \end{bmatrix} \tag{4.17}$$

where, from (2.25)

$$\tan\alpha = \frac{\partial \boldsymbol{b}_{yz,\epsilon}}{\partial x} \cdot \boldsymbol{n}_T \tag{4.18}$$

The range shift, $\delta_{r,\epsilon}$, due to a differential motion error, is then:

$$\delta_{r,\epsilon} = r_2 - r_1 = r' - r = b_{x,\epsilon} \sin\alpha + (r_0 - \boldsymbol{b}_{yz,\epsilon} \cdot \boldsymbol{n}_T)\cos\alpha - r_0 \tag{4.19}$$

with the differential motion errors evaluated at x_0. The azimuth shift due to motion error is:

$$\delta_{x,\epsilon} = x_2 - x_1 = x' - 0 = -b_{x,\epsilon} \cos\alpha + (r_0 - \boldsymbol{b}_{yz,\epsilon} \cdot \boldsymbol{n}_T)\sin\alpha \tag{4.20}$$

If $\alpha \ll 1$, which will be the case for small motion errors (see also 2.3.1), the following approximations apply

$$\sin\alpha \approx \alpha \approx \tan\alpha = \frac{\partial \boldsymbol{b}_{yz,\epsilon}}{\partial x} \cdot \boldsymbol{n}_T \tag{4.21}$$

$$\cos\alpha \approx 1 \tag{4.22}$$

With these approximations, the range shift can be approximated by (see (2.19))

$$\delta_{r,\epsilon} \approx -\boldsymbol{b}_{yz,\epsilon} \cdot \boldsymbol{n}_T = -b_{y,\epsilon} \sin\theta_T + b_{z,\epsilon} \cos\theta_T = r_\epsilon \tag{4.23}$$

where it has been assumed that $b_{x,\epsilon} \sin\alpha \approx 0$ since $\alpha \ll 1$. The differential range error can be interpreted as residual (uncompensated) range shift, r_ϵ, on track 2. This range shift is problematic, since it results in a bias on the interferogram phase:

$$\phi_{IF,\epsilon} = \frac{4\pi}{\lambda} r_\epsilon = -\frac{4\pi}{\lambda} \boldsymbol{b}_{yz,\epsilon} \cdot \boldsymbol{n}_T \tag{4.24}$$

If the effect of topography on the differential range error can be neglected, the range shift can be approximated by:

$$\delta_{r,\epsilon,ref} = -b_{y,\epsilon} \sin\theta_R + b_{z,\epsilon} \cos\theta_R \tag{4.25}$$

where it is assumed that the target lies on the reference surface, i.e. $\theta_T \approx \theta_R$. This approximation can of course not be applied to interferometric SAR theory in general, but under the assumption of small differential motion errors and moderate topography, (4.25) is a reasonable approximation to (4.23), since in this case $|\cos\theta_T - \cos\theta_R| \ll 1$ and $|\sin\theta_T - \sin\theta_R| \ll 1$. The range shift can then also be written as

$$\delta_{r,\epsilon,ref} = -b_{\parallel\epsilon} \tag{4.26}$$

where $b_{\parallel\epsilon} = \boldsymbol{b}_{yz,\epsilon} \cdot \boldsymbol{n}_R$ is the projection of the baseline error on the nominal line-of-sight direction.

The azimuth shift can be approximated by:

$$\begin{aligned} \delta_{x,\epsilon} &\approx -b_{x,\epsilon} + r_o \frac{\partial \boldsymbol{b}_{yz,\epsilon}}{\partial x} \cdot \boldsymbol{n}_T \\ &= -b_{x,\epsilon} - r_o \frac{\partial r_\epsilon}{\partial x} \\ &= -b_{x,\epsilon} + r_0 \left(\frac{\partial b_{y,\epsilon}}{\partial x} \sin\theta_T - \frac{\partial b_{z,\epsilon}}{\partial x} \cos\theta_T\right) \end{aligned} \tag{4.27}$$

where it has been assumed that $(\boldsymbol{b}_{yz,\epsilon} \cdot \boldsymbol{n}_T) \sin\alpha \approx 0$. If the effect of topography on the differential range error can be neglected, the azimuth shift (4.27) can be approximated by

$$\begin{aligned} \delta_{x,\epsilon,ref} &= -b_{x,\epsilon} + r_0 \left(\frac{\partial b_{y,\epsilon}}{\partial x} \sin\theta_R - \frac{\partial b_{z,\epsilon}}{\partial x} \cos\theta_R\right) \\ &= -b_{x,\epsilon} + r_0 \frac{\partial b_{\parallel\epsilon}}{\partial x} \end{aligned} \tag{4.28}$$

As can be seen from (4.28), the azimuth shift is sensitive to uncompensated cross-track velocities in the line of sight direction, and this sensitivity can be exploited in the estimation of motion errors. As an example, a differential cross-track velocity error of 1 cm/s in the line-of-sight direction will lead to an azimuth shift of 42 cm, assuming a range of 10 km and a sensor velocity of 240 m/s. The azimuth shift in itself does not introduce a phase bias, but if it causes excessive misregistration, a loss of interferometric coherence occurs, according to (4.12).

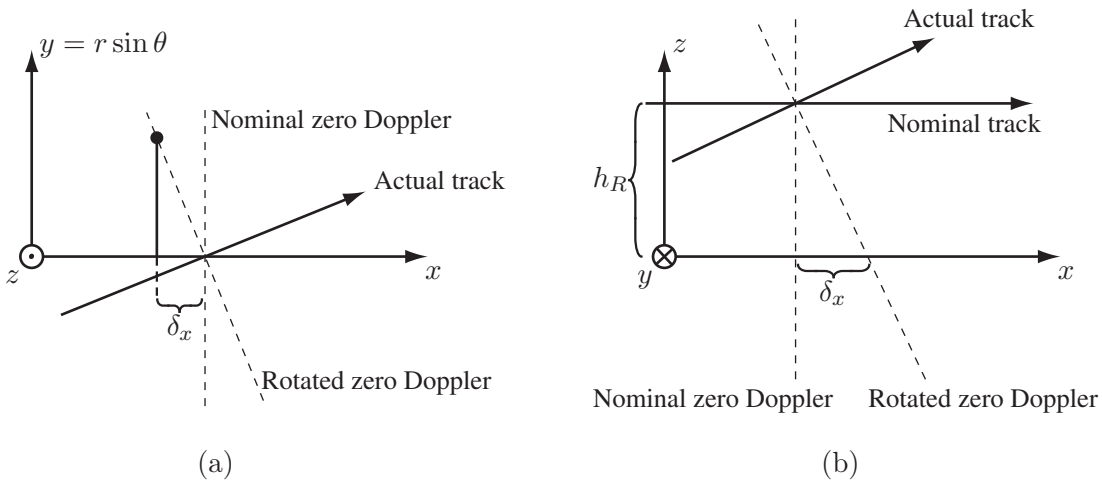

(a) (b)

Figure 4.3: Azimuth shifts due to cross-track velocity errors in a flat Earth geometry, (a) Horizontal cross-track velocity error, looking into the ground plane, (b) Vertical cross-track velocity error, looking into the (x, z)-plane and assuming a reference surface height $z_{ref} = 0$.

If a flat reference surface is assumed, (4.28) can be written

$$\delta_{x,\epsilon,flat} = -b_{x,\epsilon} + \frac{\partial b_{y,\epsilon}}{\partial x} r_0 \sin\theta_R - \frac{\partial b_{z,\epsilon}}{\partial x} h_R \tag{4.29}$$

where $h_R = r_0 \cos\theta_R$ is the reference sensor altitude. Thus, for targets located on a flat reference surface, a horizontal cross-track velocity error causes a range dependent azimuth shift proportional to the target ground range, whereas a vertical cross-track velocity error causes an azimuth shift that is independent of range. This can also be interpreted in terms of the zero-Doppler plane. This is the plane perpendicular to the actual sensor flight direction. The broadside SAR focusing maps all targets to the sensor along-track position at which they appear in the zero-Doppler plane. An uncompensated horizontal cross-track velocity error causes a horizontal rotation of this plane, as illustrated in Figure 4.3(a). This results in a horizontally variant azimuth shift. An uncompensated vertical velocity error causes a vertical rotation of the plane. This results in a vertically variant azimuth shift, but with all targets approximately at the same height, the azimuth shift is range invariant. This is important, since it means that from the azimuth misregistrations alone, an along-track motion error cannot be distinguished from a vertical cross-track velocity error.

4.2.2 Impact of topography

Motion compensation is often carried out without accounting for the topography of the scene. Even if the topography is known a priori, accounting for it complicates the motion compensation procedure, as different targets observed at in the antenna beam may require different line-of-sight vectors. The result of performing motion compensation with unkown topography is the residual range shift $\Delta r_{topo,IF}$, given by (4.3). However, if the sensor does not follow the reference track, the topographic range shift changes along the aperture, introducing an azimuth shift through the

azimuth matched filter. Note that this shift is introduced by the motion compensation procedure and thus depends on the estimated sensor motion, not the motion estimation error. It occurs even in the absence of motion estimation errors.

Assuming that the estimated sensor motion can be considered linear within the synthetic aperture of a single target, the same analysis as in section 4.2.1 can be applied, interpreting the topographic range shift as a residual range shift on track 2. From (4.23) it is seen that the linear along-track variation of the topographic shift does not affect the interferometric range shift. Thus the range shift due to topography is, as could be expected:

$$\delta_{r,topo} = \Delta r_{topo,IF} = -\frac{b_\perp}{r_0 \sin\theta_R} h_T \tag{4.30}$$

with $\Delta r_{topo,IF}$ given by (4.3). The azimuth shift due to uncompensated topography is, from (4.27) and (4.3):

$$\begin{aligned} \delta_{x,topo} &= -r_0 \frac{\partial \Delta r_{topo,IF}}{\partial x} \\ &= \frac{h_T}{\sin\theta_R} \frac{\partial b_\perp}{\partial x} \\ &= \frac{1}{\sin\theta_R} \left(\frac{\partial \widehat{b}_y}{\partial x} \cos\theta_R + \frac{\partial \widehat{b}_z}{\partial x} \sin\theta_R \right) h_T \end{aligned} \tag{4.31}$$

where h_T is the target height over the reference surface to which motion compensation has been performed. Thus the azimuth shift is directly proportional to the perpendicular baseline velocity and to the height of the target above the reference surface. There is no phase bias error associated with this shift, and thus it can be accepted to the extent that it does not cause a loss of coherence, according to (4.12).

To give an idea of the magnitude of the topography-induced azimuth misregistrations, an example is in order. Assuming a 45° look angle, a sensor velocity of 240 m/s and a sensor cross-track velocity of 1 m/s perpendicular to the line-of-sight direction, a target height of 100 m will lead to an azimuth shift of 0.6 m.

4.2.3 Summary of motion error model

The motion error model derived in section 4.2.1 assumes that the along-track variation of the differential motion error can be considered linear within a synthetic aperture. For slowly varying motion errors caused by, for example, INU drift, this is a good approximation. For rapidly varying motion estimation errors which cannot be considered linear within an aperture, the model cannot be applied directly. In that case, only the slowly varying part of the motion may be estimated, leaving a residual motion error along the aperture. If it is desired to estimate a rapidly varying motion error, an option is to use a lower azimuth resolution, implying a shorter aperture. If the motion error can be considered linear within the shorter aperture, the model can then be applied.

The model for the topography-induced misregistrations in section 4.2.2 is based on the assumption that the along-track variation of the estimated differential sensor motion can be considered linear within a synthetic aperture. In the absence of motion errors, the estimated sensor motion is also the actual sensor motion. In the

EMISAR system, the flight control system causes a sinusoidal vertical motion of the aircraft with an amplitude of approximately 0.5 m and a period of typically 1 km to 1.5 km. This period is comparable to the typical EMISAR synthetic aperture length at L-band, which is 800 m, assuming an azimuth resolution of 1.5 m and a range of 10 km. Thus, the actual sensor motion cannot necessarily be considered linear within an aperture, and this should be noted when applying the model (4.31).

When the sensor motion and the motion estimation errors can be considered linear within a synthetic aperture, the total observed range registration can, from sections 4.2.1 and 4.2.2, be modeled by:

$$\begin{aligned}\delta_r &= \delta_{r,\epsilon} + \delta_{r,topo} \\ &\approx -b_{\parallel\epsilon} - \frac{b_\perp}{r_0 \sin\theta_R} h_T\end{aligned} \tag{4.32}$$

where $b_{\parallel\epsilon}$ is the projection of the differential motion error onto the nominal line-of-sight direction (4.28) and $b_\perp$ is the perpendicular baseline, given by (4.6). The last term of (4.32) is the interferometric range shift due to a target height, h_T, above the reference surface. In topography mapping, this is the desired signal to be estimated from the interferometric phase.

The total observed azimuth misregistration can be modeled by

$$\begin{aligned}\delta_x &= \delta_{x,\epsilon} + \delta_{x,topo} \\ &\approx -b_{x,\epsilon} + r_0 \frac{\partial b_{\parallel\epsilon}}{\partial x} + \frac{h_T}{\sin\theta_R} \frac{\partial b_\perp}{\partial x}\end{aligned} \tag{4.33}$$

where $b_{x,\epsilon}$ is the differential along-track motion error.

4.3 Estimating misregistration

The misregistration between two SAR images varies with both range and azimuth and can be estimated in several different ways. With traditional methods, the misregistrations are estimated at a number of evenly spaced image positions, and the shift estimation is carried out by crosscorrelating patches around these positions. In this work, the spectral diversity method has been used, and this is briefly summarized in the following.

4.3.1 Spectral Diversity Coregistration (SDC)

The Spectral Diversity Coregistration (SDC) algorithm [26] for estimating misregistration uses the fact that a displacement in the time (or spatial) domain is equivalent to a linear phase multiplication in the frequency domain. The basic principle is illustrated in Figure 4.4, and is the same whether the method is used for range or azimuth coregistration. The method was originally invented for absolute phase determination [27], where it is known as the split-spectrum algorithm. In the following, the principle of the algorithm is illustrated for estimating azimuth misregistration, but the method can equally well be applied in the range direction.

A point target located at the nominal position $x = 0$ is assumed. The impulse response in image 1 is displaced by Δx_1, and the impulse response in image 2 is

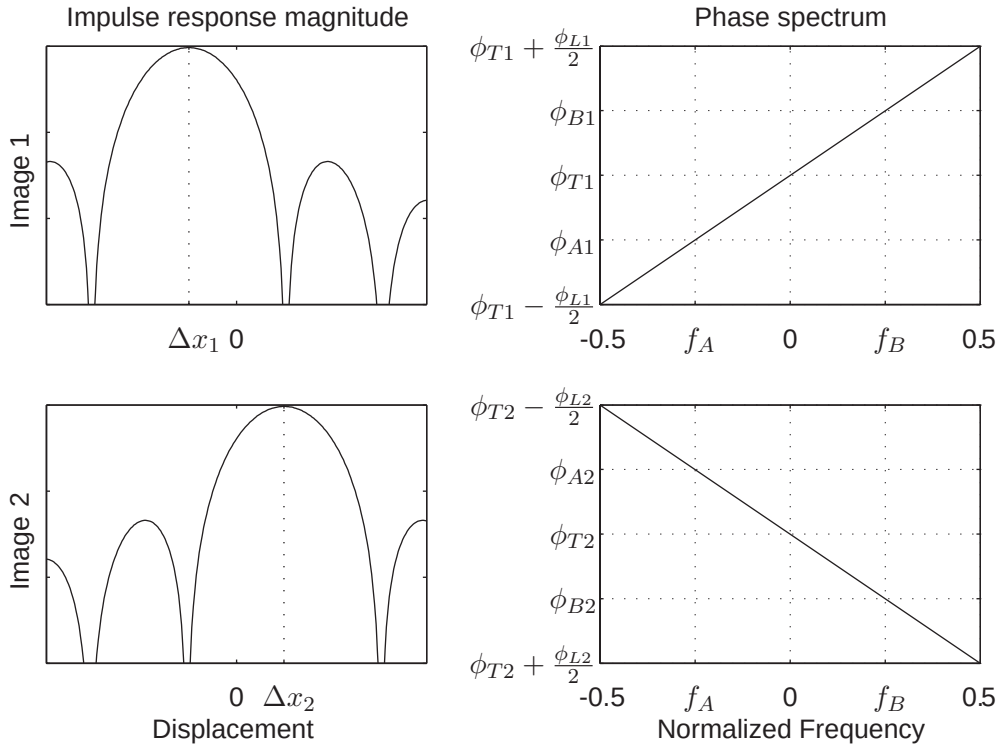

Figure 4.4: Illustration of Spectral Diversity Coregistration method.

displaced by Δx_2. The misregistration to be estimated is $\delta_x = \Delta x_2 - \Delta x_1$. Going to the frequency domain, the shifts are equivalent to linear phase factors. The linear phase in the frequency domain due to a shift in the time domain can be characterized by the total variation of the phase, ϕ_L, over the bandwidth according to

$$\phi_L = -2\pi \frac{\Delta x}{\rho_x} \tag{4.34}$$

where ρ_x is the sample spacing in the x-direction.

The spectral diversity method starts by generating from each image, 1 and 2, two non-overlapping low-resolution looks centered on the normalized frequencies f_A and f_B. The mean phase of the resulting low-resolution impulse responses is from Figure 4.4

$$\phi_{A1} = \phi_{T1} + \phi_{L1} f_A \qquad \phi_{B1} = \phi_{T1} + \phi_{L1} f_B \tag{4.35}$$

$$\phi_{A2} = \phi_{T2} + \phi_{L2} f_A \qquad \phi_{B2} = \phi_{T2} + \phi_{L2} f_B \tag{4.36}$$

where the target phases, ϕ_{T1} and ϕ_{T2} contain contributions from topography, motion errors and possibly other phase bias terms. Next, two low-resolution interferograms are generated, one from the two low band looks, A, and one from the two high band looks, B. The phase of these interferograms is

$$\phi_A = \phi_{A1} - \phi_{A2} = \phi_{T1} - \phi_{T2} + f_A(\phi_{L1} - \phi_{L2}) \tag{4.37}$$

$$\phi_B = \phi_{B1} - \phi_{B2} = \phi_{T1} - \phi_{T2} + f_B(\phi_{L1} - \phi_{L2}) \tag{4.38}$$

Finally, a differential interferogram between the two low-resolution interferograms is formed to cancel the target phase terms

$$\phi_{SDC} = \phi_A - \phi_B = (f_A - f_B)(\phi_{L1} - \phi_{L2}) \tag{4.39}$$

Using (4.34), the shift can then be estimated by

$$\delta_x = \Delta x_2 - \Delta x_1 = \frac{\rho_x}{2\pi\Delta f}\phi_{SDC} \tag{4.40}$$

where $\Delta f = f_B - f_A$ is the look center frequency separation relative to the full-resolution bandwidth.

Before using the spectral diversity method, the images should be registered to within $\pm\rho_x/(2\Delta f)$ to avoid wrapping of the differential interferogram, and to get the maximum coherence. For the example on Figure 4.4, $f_B - f_A = \frac{1}{2}$, and the images should thus be registered to within a resolution cell.

In [26] it is shown that the probability density function of the differential interferogram phase is equal to the convolution of the probability density function of the two low-resolution interferograms, and therefore the differential phase is considerably more noisy, leading to a noisy estimate of the image shifts. The estimate noise can be reduced by averaging the differential interferograms. If N samples are averaged, it is shown in [28] that for N large, the variance of the spectral diversity shift estimator comes close to the theoretical minimum, which is achieved with a complex cross correlation. The spectral diversity algorithm, however is faster and simpler to implement, and insensitive to phase variations from the topography that are cancelled out in the differential interferogram formation. With the complex cross-correlation method, the topographic phase and other systematic phase contributions must be removed prior to the correlation [28].

4.4 Estimating differential motion errors

The first step in differential motion error estimation is the estimation of δ_x and δ_r as a function of image coordinates. When patch-based methods such as speckle tracking or coherence optimization are applied, the misregistration estimates are typically only available at a subset of image positions. The SDC method described in section 4.3.1 automatically provides estimates of the range misregistration for every second range sample, and estimates of the azimuth misregistration for every second azimuth sample. Inverting the observed misregistrations to differential motion errors is complicated by the fact that cross-track motion errors give rise to both range and azimuth misregistrations, whereas along-track errors give rise only to azimuth misregistrations. There are generally two approaches to estimate the differential motion errors, parametric and non-parametric. These are described in the following.

4.4.1 Parametric motion error estimation

A method that uses image miregistrations for motion estimation is suggested in [29] and generalized in [30]. It is assumed that the baseline errors can be modeled by

polynomia

$$b_{x,\epsilon}(x) = \sum_{k=0}^{p_x-1} b_{x,\epsilon,k} x^k \tag{4.41}$$

$$b_{y,\epsilon}(x) = \sum_{k=0}^{p_y-1} b_{y,\epsilon,k} x^k \tag{4.42}$$

$$b_{z,\epsilon}(x) = \sum_{k=0}^{p_z-1} b_{z,\epsilon,k} x^k \tag{4.43}$$

Inserting these expressions into (4.32) and (4.33), and using several points in the image, the coefficients of these polynomia can be obtained from a least squares fit, as described in [30].

With the parametric method, a polynomial fit to the baseline error is obtained in both the along-track and each of the cross-track directions. The method is well suited for slowly varying errors (e.g. INU drifts) that can be modeled by polynomia. Furthermore, the method can be used when the motion errors are so large that shifts of several resolution cells are seen and the images do not register at all. This could be the case in systems where only non-kinematic GPS is available for correcting the INU motion data. In principle, the method requires knowledge of the topography, since the range and azimuth misregistrations contains contributions from both motion errors and topography. However, if the method is used over flat terrain, this can be neglected. Also, if the method is used as a preprocessing step to roughly register the images to within a resolution cell, the topography may also be ignored. This is especially true in case of a small perpendicular baseline and moderate topography.

4.4.2 Non-parametric motion error estimation

A non-parametric method for differential motion error estimation is the algorithm proposed by Reigber in [2]. It is called the residual motion estimation algorithm, and will in the following be referred to as the RME algorithm. The underlying assumption is that the dominant contribution to the observed azimuth misregistration, δ_x, comes from the cross-track motion estimation error, $\delta_{x,\epsilon}$, and that azimuth misregistration from along-track motion errors and unknown topography can be ignored ($\delta_{x,topo} \approx 0$ and $b_{x,\epsilon} \approx 0$) . With these assumptions, and the assumption that the motion error can be considered linear within an aperture, the observed azimuth misregistration at a given image coordinate is directly proportional to the projection of the derivative of the motion error at that coordinate. Thus, the underlying assumption of the RME algorithm is that

$$\delta_x \approx r_0 \frac{\partial b_{\parallel\epsilon}}{\partial x} = r_0 \left(\frac{\partial b_{y,\epsilon}}{\partial x} \sin\theta_R - \frac{\partial b_{z,\epsilon}}{\partial x} \cos\theta_R \right) \tag{4.44}$$

Considering a single range bin at range r_0, the differential motion error in this range bin can be estimated to within a constant by:

$$b_{\parallel\epsilon}(x_0, r_0) = \int_0^{x_0} \frac{\delta_x(x, r_0)}{r_0} \mathrm{d}x + b_{\parallel\epsilon,0}(r_0) \tag{4.45}$$

where $b_{\|\epsilon,0}$ is an unknown constant. With this approach, the differential motion error is not limited to a polynomial variation. The spectral diversity method for estimating misregistration (see section 4.3.1) is convenient for this algorithm, since the output estimates of the azimuth misregistrations are automatically closely spaced (two times the original azimuth pixel spacing), and no interpolation is necessary.

In the more general case, the variation of (4.44) across the range swath can be used to estimate both the horizontal and the vertical components of the cross-track error. Consider a single along-track position, x_0, where N estimates, $\delta_{x1}, \delta_{x2}, \ldots, \delta_{xN}$, of the azimuth misregistration are available, corresponding to the ranges $r_1, r_2, \ldots, r_N$. Then, from (4.44), a linear model can be set up:

$$\boldsymbol{\chi} = \boldsymbol{H}\boldsymbol{P} \tag{4.46}$$

where the observation vector, $\boldsymbol{\chi}$ is

$$\boldsymbol{\chi} = \begin{bmatrix} \delta_{x1} \\ \delta_{x2} \\ \vdots \\ \delta_{xN} \end{bmatrix} \tag{4.47}$$

and the sensitivity matrix, $\boldsymbol{H}$, is

$$\boldsymbol{H} = \begin{bmatrix} r_1 \sin\theta_{R1} & -r_1 \cos\theta_{R1} \\ r_2 \sin\theta_{R2} & -r_2 \cos\theta_{R2} \\ \vdots & \vdots \\ r_N \sin\theta_{RN} & -r_N \cos\theta_{RN} \end{bmatrix} \tag{4.48}$$

The parameter vector is

$$\boldsymbol{P} = \begin{bmatrix} \frac{\partial b_{y,\epsilon}}{\partial x} \\ \\ \frac{\partial b_{z,\epsilon}}{\partial x} \end{bmatrix} \tag{4.49}$$

The least squares solution to (4.46) provides an estimate of P:

$$\widehat{\boldsymbol{P}} = \boldsymbol{H}^{\dagger}\boldsymbol{\chi} \tag{4.50}$$

where $\boldsymbol{H}^{\dagger}$ is the $2 \times N$ pseudo-inverse of $\boldsymbol{H}$:

$$\boldsymbol{H}^{\dagger} = (\boldsymbol{H}^{\mathrm{T}}\boldsymbol{H})^{-1}\boldsymbol{H}^{\mathrm{T}} \tag{4.51}$$

and

$$\widehat{\boldsymbol{P}} = \begin{bmatrix} \frac{\partial \widehat{b}_{y,\epsilon}}{\partial x} \\ \\ \frac{\partial \widehat{b}_{z,\epsilon}}{\partial x} \end{bmatrix} \tag{4.52}$$

contains the estimated derivatives of the differential motion error. Using the spectral diversity method, an estimate of the azimuth misregistration is available for every range position ($N = N_{RA}$) but only for every second azimuth position, due to the two looks. Solving (4.50) for every available range line, $N_{AZ}/2$ estimates of $(\frac{\partial b_{y,\epsilon}}{\partial x}, \frac{\partial b_{z,\epsilon}}{\partial x})$

are available, and both estimates can then be integrated to obtain the differential motion error estimates to within a constant in each of the cross-track dimensions.

$$\widehat{b}_{y,\epsilon}(x_0) = \int_0^{x_0} \frac{\partial \widehat{b}_{y,\epsilon}}{\partial x} \mathrm{d}x + b_{y,\epsilon,0} \tag{4.53}$$

$$\widehat{b}_{z,\epsilon}(x_0) = \int_0^{x_0} \frac{\partial \widehat{b}_{z,\epsilon}}{\partial x} \mathrm{d}x + b_{z,\epsilon,0} \tag{4.54}$$

where x_0 is an arbitrary along track position, and $b_{y,\epsilon,0}, b_{z,\epsilon,0}$ are unknown constants.

If the variation of the incidence angle across the swath is small, $\boldsymbol{H}^T\boldsymbol{H}$ becomes almost singular, and the separation of the differential motion error derivatives into a horizontal and vertical component becomes ill-conditioned. If the swath is narrow enough to ignore the range variation of the motion-induced phase errors, the slant range projection of the differential motion error can be estimated as in (4.45), averaging over all ranges.

Even if the focused swath width is large enough to separate the baseline error into horizontal and vertical components, misregistrations cannot be estimated for incoherent areas in the images. To account for this, a coherence mask can be generated, indicating which pixels to exclude in the differential motion estimation. This exclusion is easily accomplished by removing rows of $\boldsymbol{H}$, but if this reduces the swath width, the problem can again become ill-conditioned. An example of this is seen in section 6.3.3. Approaches for stabilizing the estimate in these situations should be examined further, but it has not been done in this study.

If there are areas in the image where no valid misregistration estimates are available for a significant range of azimuth positions (e.g. a wide river flowing in the range direction across the image), the integrations (4.53) and (4.54) cannot be performed across this area. In this case, the differential motion derivatives must be interpolated across this area. An approach for this has been suggested in [31]. This approach uses more than two subapertures in the spectral diversity misregistration estimation. This allows estimates of the misregistration to be obtained even over low-coherent areas, using that the azimuth impulse response from a high-coherent area can extend in to the low-coherent area. However, if the azimuth width of the low-coherent area is on the order of or larger than half the synthetic aperture width, this approach is also not possible.

4.4.3 Estimating constant differential motion errors

As mentioned in section 4.2, a constant cross-track differential motion error $(b_{y,\epsilon,0}, b_{z,\epsilon,0})$ does not give rise to azimuth shifts. This is also seen from (4.27), since for a constant error, the derivatives of the error are 0. If the topography is unknown, it is generally impossible, whether using parametric or non-parametric motion error estimation, to distinguish whether the range shift caused by such an error is due to a motion error, or due to topography. In this case, the differential motion error must be estimated using an external digital elevation model or tie-points in the image.

A constant differential motion error will, from (4.25), result in a range shift

$$\begin{aligned} \delta_r(r,x) &= -b_{y,\epsilon,0}\sin\theta_T(r,x) + b_{z,\epsilon,0}\cos\theta_T(r,x) \\ &\approx -b_{y,\epsilon,0}\sin\theta_R(r) + b_{z,\epsilon,0}\cos\theta_R(r) \end{aligned} \tag{4.55}$$

The last approximation is valid for small motion errors and moderate topography, and allows estimates of the differential shift to be averaged over azimuth. Thus a constant motion error will result in a range shift which is independent of along-track position but range dependent. This in turn results in an interferometric phase shift, according to (4.24). With the approach in [32], an external DEM is projected to the image slant range geometry (see section 5.2.2) and a synthetic interferogram is generated, simulating the topographic phase contribution (4.4). The synthetic interferogram is then subtracted from the unwrapped interferogram, and the phase of this differential interferogram is, assuming that all time-varying motion errors have been corrected,

$$\begin{aligned}\phi_s(r,x) &= \phi_{abs} + \phi_{\epsilon,0}(r) \\ &= \phi_{abs} + \frac{4\pi}{\lambda}(-b_{y,\epsilon,0}\sin\theta_R(r) + b_{z,\epsilon,0}\cos\theta_R(r)) \\ &= \phi_{abs} - \frac{4\pi}{\lambda}b_{\parallel\epsilon,0}(r)\end{aligned} \tag{4.56}$$

which is independent of x. To reduce phase noise, ϕ_s can be averaged over the along-track dimension to obtain the range profile $\phi_s(r)$, from which the three unknown parameters, $(\phi_{abs}, b_{y,\epsilon,0}, b_{z,\epsilon,0})$ can be estimated. At each range, the range shift due to the constant motion error is the projection of the constant motion error on the nominal line of sight direction at that range. A linear model can be set up

$$\begin{bmatrix}\Delta r_1 \\ \vdots \\ \Delta r_N\end{bmatrix} = \begin{bmatrix}1 & -\sin\theta_1 & \cos\theta_1 \\ \vdots & \vdots & \vdots \\ 1 & -\sin\theta_N & \cos\theta_N\end{bmatrix} \begin{bmatrix}\frac{\lambda}{4\pi}\phi_{abs} \\ b_{y,\epsilon,0} \\ \tilde{b}_{z,\epsilon,0}\end{bmatrix} \tag{4.57}$$

where $\Delta r_i = \frac{\lambda}{4\pi}\phi_{diff}(r_i)$ are the samples of the $\phi_s(r)$ profile converted to a range shift. The solution to (4.57) can be obtained the same way as in 4.4.2.

4.5 Correcting differential motion errors

When the differential motion errors have been estimated as described in 4.4.2, there are several options to correct the SAR data, as illustrated in Figure 4.5.

(a) The simplest approach is to correct the interferogram phase using the estimated baseline errors. This does not correct the misregistration caused by the baseline error, but if the errors are small enough that the misregistration does not significantly affect the coherence, this can be ignored. The correction then becomes a simple postprocessing step. Alternatively, the phase correction can be supplemented by interpolation in the images before interferogram formation. The phase that is subtracted from the interferogram is given by (4.24).

(b) A method is suggested in [33] that, in addition to the phase error (4.24) also corrects the azimuth misregistration caused by the differential motion errors. This is achieved by inverting the azimuth compression of the slave image, applying the phase correction, and recompressing. With fast FFT routines, this can be achieved more efficiently than phase correction and interpolation in

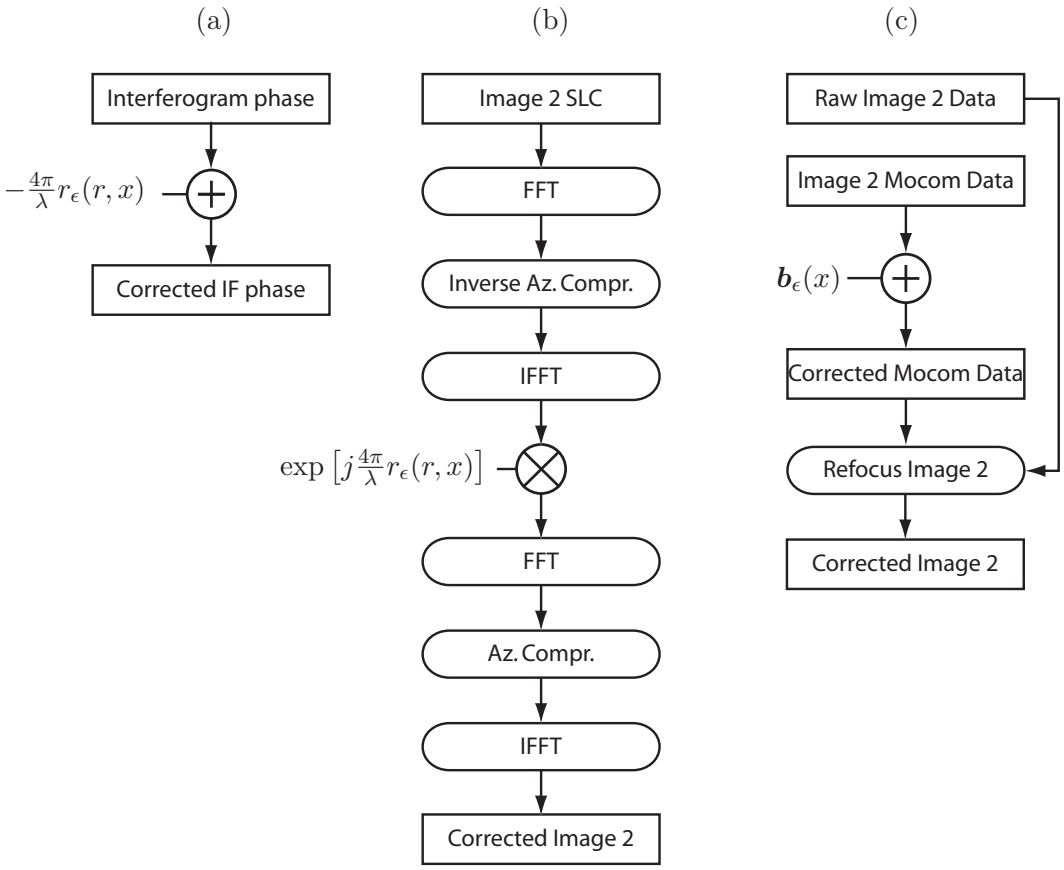

Figure 4.5: Correction of estimated differential motion errors, (a) Simple IF correction, (b) Inverse azimuth compression approach, (c) Reprocessing with corrected motion data.

separate steps [34]. Alternatively, both master and slave can be corrected this way, applying 50% of the correction to each image. In either case, the method does not correct the range misregistration caused by the differential error, but the range misregistration is typically much smaller than the corresponding azimuth misregistrations. Since the correction is applied to image 2, the phase correction has the opposite sign as in (a).

(c) The most accurate way to correct the estimated baseline errors is to modify the navigation data used for motion compensation and reprocess. This is more time-consuming than the abovementioned methods, but also corrects the residual range registration. Again, both images can be reprocessed with 50% of the baseline correction or the slave image can be reprocessed with the entire correction applied to the motion data for the slave image. When the correction is applied to image 2, the estimated differential motion error, $\boldsymbol{b}_\epsilon$, is added to the image 2 motion data. Note that with the RME algorithm described in section 4.4.2, only the cross-track components of the differential motion error are estimated and corrected.

Chapter 5

Improved Non-parametric Motion Error Estimation

As described in section 4.4, there are generally two ways to estimate differential motion errors in SAR interferometry, parametric and non-parametric. The non-parametric approach allows the estimation of motion errors that cannot be modeled by a polynomial, but it relies on the assumption that the observed azimuth misregistrations do not contain contributions from along-track motion estimation errors, or from unknown topography.

In section 5.1, the influence of along-track errors on the non-parametric motion error estimate is analyzed, and a method to distinguish along-track position errors from cross-track velocity errors using an external DEM is proposed. This method relies on a parametric estimate of the along-track error, but the estimate of the cross-track error is still non-parametric.

The influence of topography on the non-parametric motion error estimate is difficult to quantify, as it depends on the actual topography and the tracks flown by the sensor. In section 5.2 a method to account for these errors using an external DEM is proposed.

The proposed schemes have been implemented in MATLAB and tested on EMISAR data. In section 5.3, the implementation is described, whereas the experimental evaluation is presented in Chapter 6.

5.1 Along-track errors

A residual along track motion error, $b_{x,\epsilon}(x)$, results directly in a corresponding azimuth misregistration, see (4.27). If small, this error does not affect the image or interferogram quality. However, if interpreted as a differential cross-track velocity error by the RME algorithm, it leads to erroneous cross-track motion error estimates. This means that after correcting the SAR image(s) with the estimated motion error, a residual error occurs:

$$\tilde{\boldsymbol{b}}_{yz,\epsilon} = \boldsymbol{b}_{yz,\epsilon} - \widehat{\boldsymbol{b}}_{yz,\epsilon} \tag{5.1}$$

where $\boldsymbol{b}_{yz,\epsilon}$ is the actual cross-track motion error, $\widehat{\boldsymbol{b}}_{yz,\epsilon}$ is the motion error estimated by the RME algorithm and $\tilde{\boldsymbol{b}}_{yz,\epsilon}$ is the residual error on the RME estimate, induced

by along-track errors.

For the general case, where the differential motion error is resolved into both horizontal and vertical components, the impact of along-track errors can be analyzed by using (4.50). An along-track baseline error, $b_{x,\epsilon}(x)$ causes an azimuth misregistration of $\delta_x = -b_{x,\epsilon}(x)$. For a single range line at azimuth positon x, the error on the estimated derivatives of the differential cross-track error is then, from (5.1) and (4.46)

$$\begin{bmatrix} \frac{\partial \tilde{b}_{y,\epsilon}}{\partial x} \\ \\ \frac{\partial \tilde{b}_{z,\epsilon}}{\partial x} \end{bmatrix} = -\boldsymbol{H}^{\dagger} \begin{bmatrix} -b_{x,\epsilon}(x) \\ -b_{x,\epsilon}(x) \\ \vdots \\ -b_{x,\epsilon}(x) \end{bmatrix} = \boldsymbol{H}^{\dagger} \begin{bmatrix} b_{x,\epsilon}(x) \\ b_{x,\epsilon}(x) \\ \vdots \\ b_{x,\epsilon}(x) \end{bmatrix} \tag{5.2}$$

where $\boldsymbol{H}^{\dagger}$ is the $(2 \times N)$ pseudo-inverse of the sensitivity matrix (4.51). This can be written as

$$\begin{bmatrix} \frac{\partial \tilde{b}_{y,\epsilon}}{\partial x} \\ \\ \frac{\partial \tilde{b}_{z,\epsilon}}{\partial x} \end{bmatrix} = \begin{bmatrix} H_y^{\dagger} b_{x,\epsilon}(x) \\ H_z^{\dagger} b_{x,\epsilon}(x) \end{bmatrix} \tag{5.3}$$

where

$$H_y^{\dagger} = \sum_{i=1}^{N} H_{1i}^{\dagger} \tag{5.4}$$

$$H_z^{\dagger} = \sum_{i=1}^{N} H_{2i}^{\dagger} \tag{5.5}$$

are the row sums of $\boldsymbol{H}^{\dagger}$ both in units of $\left[\mathrm{m}^{-1}\right]$.

In section 4.2.1 it was shown that in a flat Earth geometry, a horizontal velocity error gives rise to a range-dependent azimuth shift, whereas a vertical velocity error results in an azimuth shift that is independent of range. An along-track motion error also results in a range-independent azimuth shift, so intuitively,

$$H_{y,flat}^{\dagger} = 0 \tag{5.6}$$

$$H_{z,flat}^{\dagger} = -\frac{1}{h_R} \tag{5.7}$$

where h_R is the nominal sensor altiude above the reference terrain height used in motion compensation and $H_{z,flat}^{\dagger}$ is found from (4.29). Thus, a differential along-track motion error only affects the vertical baseline estimate. If the along-track error is positive, then from (4.33), a negative azimuth shift occurs. From (4.29), a positive velocity error also gives a negative azimuth shift, so a positive along-track error is estimated as a positive vertical velocity error. After correcting the motion data with the RME motion error estimate, the residual error will then be a negative crosstrack velocity, as indicated by (5.7).

For a non-flat Earth geometry, the values of $H_y^{\dagger}$ and $H_z^{\dagger}$ can be evaluated. This has been done for the EMISAR geometries used in Chapter 6. For the `fl075` geometry (section 6.2), the sensor altitude over the reference surface is $h_R = 7504$ m. For this

geometry, $H_y^\dagger = -2.0 \times 10^{-7}$ m^{-1} and $H_z^\dagger = -1.3 \times 10^{-4}$ m^{-1}, so as expected $|H_z^\dagger| \gg |H_y^\dagger|$. Furthermore, $-1/H_z^\dagger = 7497$ m $\approx h_R$. The same is seen for the `fl045` geometry (section 6.3), where the altitude is $h_R = 12395$ m In this case, $H_y^\dagger = -2 \times 10^{-7}$ m^{-1} and $H_z^\dagger = -8.1 \times 10^{-5}$ m^{-1}. For this geometry also, $-1/H_z^\dagger = 12378$ m $\approx h_R$.

The residual error on the estimate of the differential motion error will be given by

$$\tilde{b}_{y,\epsilon}(x) = H_y^\dagger \int_0^x b_{x,\epsilon}(x')\mathrm{d}x' \approx 0 \tag{5.8}$$

$$\tilde{b}_{z,\epsilon}(x) = H_z^\dagger \int_0^x b_{x,\epsilon}(x')\mathrm{d}x' \approx -\frac{1}{h_R}\int_0^x b_{x,\epsilon}(x')\mathrm{d}x' \tag{5.9}$$

The validity of the approximation (5.8) can be evaluated for the `fl045` scene, which is approximately 100 km long. A constant $b_{x,\epsilon}$ of 1 m will lead to a linearly growing horizontal error, reaching a maximum at the edge of the image of $\tilde{b}_{y,\epsilon}(100 \text{ km}) = -2.0 \times 10^{-7}$ m^{-1} $\cdot$ 1 m $\cdot$ 100 km $= -2$ cm. The vertical error, $\tilde{b}_{z,\epsilon}$, will reach a maximum of -8.1 m. In this case the error from using the approximation (5.9) is 1 cm.

For long strips, the vertical position error can grow significantly as an along-track error is integrated along the image. Linear and higher order along-track errors will introduce quadratic and higher-order cross-track errors, respectively. However, rapidly varying motion errors will not contribute significantly to the vertical error, since the integration in (5.9) suppresses rapidly varying errors. As an example, let the along-track motion error be modeled as a sinusoid,

$$b_{x,\epsilon} = b_0 \cos 2\pi \frac{n}{L_x} x \tag{5.10}$$

where b_0 is the amplitude, n is the number of cycles of the error along the image and L_x is the length of the image. The induced vertical error will, from (5.9) be:

$$\tilde{b}_{z,\epsilon}(x) = \frac{b_0 L_x}{2\pi n h_R} \sin 2\pi \frac{n}{L_x} x \tag{5.11}$$

which is inversely proportional to n.

If one or both images are corrected using the erroneous estimate of the vertical motion error, $\widehat{b}_{z,\epsilon} = b_{z,\epsilon} + \tilde{b}_{z,\epsilon}$, the induced cross-track error will compensate completely the azimuth misregistration due to along-track errors, but cross-track errors are introduced instead. Since the impact of these are much more severe than a small uncompensated azimuth misregistration, this must be accounted for.

5.1.1 Estimating along-track errors using External DEM

If an external DEM is available, the phase of the unwrapped, RME-corrected interferogram, $\phi_{RME}(x, r)$, can be compared to a synthetic interferogram, $\phi_{synt}(x, r)$ generated from the external DEM and the motion data, as described in sections 4.4.3 and 5.2.3. In the absence of other phase errors, this residual interferogram will contain contributions from a constant phase offset, ϕ_{abs}, a constant differential motion error, $\boldsymbol{b}_{\epsilon,0}$, and the error induced by along track motion, $\tilde{\boldsymbol{b}}_\epsilon$. The residual

interferogram phase, $\phi_{RME,\epsilon}$, is then, from (4.55) and (5.9)

$$\begin{aligned}\phi_{RME,\epsilon}(x,r) &= \phi_{abs} - \frac{4\pi}{\lambda}\left(\boldsymbol{b}_{\epsilon,0} + \tilde{\boldsymbol{b}}_{\epsilon}(x,r))\right)\cdot \boldsymbol{n_T}(x,r) \\ &\approx \phi_{abs} - \frac{4\pi}{\lambda}\left(\boldsymbol{b}_{\epsilon,0} + \tilde{\boldsymbol{b}}_{\epsilon}(x,r)\right)\cdot \boldsymbol{n}_R(r) \\ &= \phi_{abs} - \frac{4\pi}{\lambda}\left(b_{y,\epsilon,0}\sin\theta_R(r) - b_{z,\epsilon,0}\cos\theta_R(r) + \frac{\cos\theta_R(r)}{h_R}\int_0^x b_{x,\epsilon}(x')\mathrm{d}x'\right) \\ &= \phi_{abs} - \frac{4\pi}{\lambda}\left(b_{y,\epsilon,0}\sin\theta_R(r) - b_{z,\epsilon,0}\cos\theta_R(r) + \frac{1}{r}\int_0^x b_{x,\epsilon}(x')\mathrm{d}x'\right)\end{aligned} \tag{5.12}$$

An alternative to using the unwrapped interferogram is to use the range misregistration of image 1 and the corrected image 2, which is unambiguous, but a much noisier estimate of the shift (see section 4.3). The range misregistration may be useful in estimating the absolute phase offset, ϕ_{abs}, though. For moderate topography, if no DEM is available but a small perpendicular baseline is used, the expected topographic range shifts are small. In this case, the synthetic interferogram may not be necessary at all, and the interferogram phase or range misregistration may be used on its own. However, if it is desired to estimate motion errors smaller than or comparable to the topographic range shifts, an external DEM is necessary.

The along-track error is modeled as a p-order polynomial:

$$b_{x,\epsilon}(x) = b_{x,\epsilon,0} + b_{x,\epsilon,1}x + b_{x,\epsilon,2}x^2 + \cdots + b_{x,\epsilon,p}x^p \tag{5.13}$$

This is a reasonable approximation, since, as indicated in the previous section, rapid variations in the along-track error will not significantly affect the RME estimate, due to the integration. For small along-track errors, it is not necessary to know the actual along-track error, only the part that affects the cross-track motion estimate significantly. The integral in (5.9) becomes:

$$\int_0^x b_{x,\epsilon}(x')\mathrm{d}x' = b_{x,\epsilon,0}x + \frac{1}{2}b_{x,\epsilon,1}x^2 + \frac{1}{3}b_{x,\epsilon,2}x^3 + \cdots + \frac{1}{p+1}b_{x,\epsilon,p}x^{p+1} \tag{5.14}$$

Taking well-distributed samples across the residual phase interferogram at points (r_i, x_j) where $i = 1\ldots N$ and $j = 1\ldots M$, and converting the residual phase, $\phi_{RME,\epsilon}$, to residual range shifts, Δr_{ij}, a linear model can be set up

$$\boldsymbol{\rho} = \boldsymbol{KQ} \tag{5.15}$$

where the observation vector is now $N\cdot M\times 1$ and contains the samples of the residual interferogram (converted from phase to range shift):

$$\boldsymbol{\rho} = \begin{bmatrix}\Delta r_{11}\\ \vdots \\ \Delta r_{ij}\\ \vdots \\ \Delta r_{NM}\end{bmatrix} = \frac{\lambda}{4\pi}\begin{bmatrix}\phi_{RME,\epsilon}(r_1,x_1)\\ \vdots \\ \phi_{RME,\epsilon}(r_i,x_j)\\ \vdots \\ \phi_{RME,\epsilon}(r_N,x_M)\end{bmatrix} \tag{5.16}$$

The sensitivity matrix is $N \cdot M \times (p+4)$

$$\boldsymbol{K} = \begin{bmatrix} 1 & -\sin\theta_1 & \cos\theta_1 & -\frac{1}{r_1}x_1 & -\frac{1}{2r_1}x_1^2 & \dots & -\frac{1}{(p+1)r_1}x_1^{p+1} \\ \vdots & \vdots & \vdots & \vdots & \vdots & \ddots & \vdots \\ 1 & -\sin\theta_i & \cos\theta_i & -\frac{1}{r_i}x_j & -\frac{1}{2r_i}x_j^2 & \dots & -\frac{1}{(p+1)r_i}x_j^{p+1} \\ \vdots & \vdots & \vdots & \vdots & \vdots & \ddots & \vdots \\ 1 & -\sin\theta_N & \cos\theta_N & -\frac{1}{r_N}x_M & -\frac{1}{2r_N}x_M^2 & \dots & -\frac{1}{(p+1)r_N}x_M^{p+1} \end{bmatrix} \tag{5.17}$$

The parameter vector is

$$\boldsymbol{Q} = \begin{bmatrix} \Delta r_{abs} \\ b_{y,\epsilon,0} \\ b_{z,\epsilon,0} \\ b_{x,\epsilon,0} \\ b_{x,\epsilon,1} \\ \vdots \\ b_{x,\epsilon,p} \end{bmatrix} \tag{5.18}$$

Instead of estimating directly the polynomial coefficients of $\tilde{b}_x$ it is advantageous to reformulate (5.13) using Chebyshev polynomials:

$$\tilde{b}_x(x) = \beta_{x0}T_0(\breve{x}) + \beta_{x1}T_1(\breve{x}) + \beta_{x2}T_2(\breve{x}) + \cdots + \beta_{xp}T_p(\breve{x}) \tag{5.19}$$

where $T_i(x)$ are the i-order Chebyshev polynomials of the first kind and $\breve{x}$ is

$$\breve{x} = \frac{x - \frac{1}{2}(x_M + x_0)}{\frac{1}{2}(x_M - x_0)} \tag{5.20}$$

Since the Chebyshev polynomials are orthogonal and normalized, the magnitude of the estimated coefficients can be interpreted directly as the magnitude of each of the terms of (5.19).

When (5.15) has been solved to obtain the estimate, $\widehat{\boldsymbol{Q}}$, of (5.18), the along-track motion error estimate, $\widehat{\boldsymbol{b}}_{x,\epsilon}$ can be calculated from (5.19). The estimate of the residual vertical motion error induced by along-track motion can be obtained from:

$$\tilde{b}_{z,\epsilon}(x) = -\frac{1}{h_R}\int_0^x \widehat{b}_{x,\epsilon}(x')\mathrm{d}x' \tag{5.21}$$

where the integral can be calculated from the estimated along-track motion error coefficients and (5.19). The estimated constant differential motion error components, $(b_{y,\epsilon,0}, b_{z,\epsilon,0})$ should also be added to the cross-track motion error estimate.

When the corrections calculated by the along-track motion estimation are small and do not cause appreciable misregistration, it is sufficient to phase correct the interferogram by the estimated cross-track errors, as described in section 4.5. If the navigation data are corrected, the along-track coordinate should also be corrected, otherwise the estimated along-track error will be converted to azimuth misregistration.

5.1.2 Summary of algorithm

The final along-track correction scheme is summarized here:

1. Perform standard non-parametric RME estimation (section 4.4.2) and correction (section 4.5), ignoring along-track errors.
2. Generate interferogram from RME-corrected data and subtract the synthetic interferogram to obtain a residual interferogram, $\phi_{RME,\epsilon}$.
3. Take samples of the residual interferogram to obtain the observation vector, $\boldsymbol{\rho}$ (eq. 5.16).
4. Calculate the sensitivity matrix, $\boldsymbol{K}$ (eq. (5.17)) using a p-order model for the residual along-track error.
5. Solve for $\widehat{\boldsymbol{Q}}$ (eq. (5.18)) using the standard least squares solution (4.50).
6. Calculate the final vertical motion correction from (5.21). This is a $p+1$-order correction, due to the integral.
7. Correct final motion error (see section 4.5) by interferogram phase correction or complete refocusing using corrected navigation data (including the p-order along-track correction). The inverse azimuth compression scheme cannot be used, as it cannot correct a non-constant along-track error without modifying the phase of the refocused image.

The proposed method is, like the basic RME algorithm, capable of correcting arbitrary cross-track motion errors, as this is done in the initial RME estimation. Since the cross-track errors induced by along-track residual motion will be of a low-frequency nature, due to the integration, it is reasonable to assume that the major contribution can be modeled by a polynomial. If the obtained estimate does not model the observed residual phase error, the order, p, of the along-track motion model can be increased. The method has been tested on EMISAR images as described in sections 6.2.4 and 6.3.4.

5.2 Impact of topography

5.2.1 Accounting for spherical Earth geometry

To accurately apply an external digital elevation model in SAR processing, it is necessary to account for the spherical Earth geometry. As mentioned in section 5.3, the `sarif` range-Doppler SAR processor [21] has been used in this project. This processor uses the (s, c, h)-coordinate system [29]. The (s, c, h)-coordinates are curvilinear coordinates on a reference sphere that locally approximates the WGS-84 Earth model ellipsoid [10]. It is defined by first selecting the approximate midpoint of the reference track as the origin of the (s, c, h)-system. The approximating sphere is selected so that it is tangent to the ellipsoid at the origin and has the same radius of curvature as the ellipsoid in the reference track direction. Then s is the along-track coordinate, c the cross-track coordinate and h the altitude over the reference sphere. The reference track is then defined by $\boldsymbol{p}_R(s) = (s, c_R, h_R)$ where c_R, h_R are constants

for the given reference track. The s and c coordinates are actually arc lengths on the reference sphere, but for the aircraft geometry they can be considered locally cartesian (i.e. within an aperture, and when evaluating the effects of for example motion compensation).

5.2.2 External DEM projection to slant range geometry

To use an external DEM, this must first be converted to the SAR image slant range geometry. In this work, the external DEM used is the Shuttle Radar Topography Mission 3 arcminute (SRTM-3) DEM [35]. This is supplied as a 3-arcminute ($\approx$ 90 m) grid of latitude, longitude and geoid height values. First, a subset of the DEM covering the imaged area is extracted. Then the geoid heights are converted to ellipsoid heights using a geoid model, and the coordinates are converted from (latitude, longitude, ellipsoid height) to the reference (s, c, h) system used in the processing. In [29], the following relations between target coordinates, slant range, and reference track coordinates are given:

$$s_T = s_R + rn_s \frac{R_a}{R_a + h_T} \tag{5.22}$$

$$c_T = c_R + rn_c \frac{R_a}{R_a + h_T} \tag{5.23}$$

$$h_T = h_R + rn_h + \frac{r^2\left(n_s^2 + n_c^2\right)}{2\left(R_a + h_R + rn_h\right)} \tag{5.24}$$

where (s_T, c_T, h_T) are the coordinates of the DEM point, (s_R, c_R, h_R) are the reference track coordinates, r is the distance from the reference track to the DEM point, $\boldsymbol{n}_T = (n_s, n_c, n_h)$ is the line-of-sight vector from the reference track to the target, and R_a is the radius of the approximating sphere. For a broadside looking SAR, $n_s = 0$, so $s_R = s_T$. Note that the definition of h_R used here is slightly different from the one used in sections 5.1 and 4.2.1, where it defines the sensor altitude over the reference surface used in motion compensation. The reference surface might not be located on the reference ellipsoid but at some constant offset altitude, h_{ref}.

With little error, the denominator of (5.24) can be approximated by $2R_a$, since $h_R \approx -rn_h$. From (5.23) and (5.24), and using that $n_c^2 + n_h^2 = 1$, three equations can be set up

$$rn_c = \frac{(c_T - c_R)(Ra + h_T)}{R_a} \tag{5.25}$$

$$rn_h = h_T - h_R - \frac{r^2 n_c^2}{2R_a} \tag{5.26}$$

$$r = \sqrt{r^2 n_c^2 + r^2 n_h^2} \tag{5.27}$$

from which r can readily be obtained. Applying this procedure to each DEM point results in a nonuniform grid of (s, r, h)-points, and a twodimensional resampling can be used to obtain a rectangular grid with the desired spacing in the image range and azimuth coordinates. This can be done under the assumption of moderate topography with no severe layover. The principle is illustrated in Figure 5.1

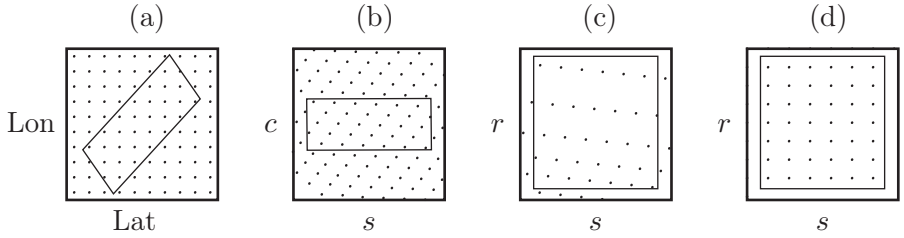

Figure 5.1: External DEM projection. (a) External DEM, (b) Converted to (s, c, h), (c) Converted to (s, r, h), (d) Resampled to uniform (s, r) grid.

5.2.3 Generation of synthetic interferogram

A synthetic interferogram can be generated concurrently with the DEM projection described in the previous section. For each DEM point that has been converted to the reference (s, c, h) geometry, the range to the master and slave track positions can be calculated, and the difference formed. This range difference can again be resampled to a rectangular grid in the image coordinates. If the dual reference track approach is used, the synthetic interferogram should be generated using the nominal master and slave tracks. For the common reference track approach, which has been used in this work, the actual sensor positions should be used. The motion data must in this case be interpolated at the along-track positions, s_T, at which the DEM points are available. Following the resampling to image coordinates, the phase shifts that have been applied in the motion compensation are applied to the synthetic interferogram.

5.2.4 Modeling azimuth misregistration from topography

According to (4.31), targets at an elevation different from the reference elevation used in motion compensation will cause an azimuth misregistration proportional to the cross-track velocities with which the data were acquired. If the azimuth misregistration is used in differential motion error estimation, the topography-induced misregistration will be interpreted wrongly as due to cross-track velocities, see section 4.4. It is therefore important that the cross-track velocities are minimized, but this depends on the flight control system used in the SAR aircraft platform. For example, the flight control system used for EMISAR on the Gulfstream G3 suffers from servo loop oscillations, leading to typical vertical cross-track velocities of up to 0.5 m/s. It is difficult to qualitatively assess the impact of topography on the residual motion estimate, but it can be exemplified using actual navigation data and a DEM. A simple method for modeling the misregistration from topography using an external DEM and navigation data is presented in the following. The method uses the fact that the topography-induced azimuth misregistration is caused by the motion compensation – which is known – coupling with the topography, which can be supplied from the external DEM.

For each output range line in the image, the vertical and horizontal cross-track velocities for each track can be obtained from the navigation data. Then, the expected

azimuth misregistration in each range bin can be calculated using (4.31):

$$\begin{aligned}\widehat{\delta}_{x,topo}(s;r) &= \frac{\widehat{h}_T(s,r)}{\sin\theta_R(r)}\frac{\partial b_\perp}{\partial s}(s,r) \\ &= \frac{\widehat{h}_T(s,r)}{\sin\theta_R(r)}\left((\frac{\partial\widehat{c}_2(s)}{\partial s}-\frac{\partial\widehat{c}_1(s)}{\partial s})\cos\theta_R(r)+(\frac{\partial\widehat{h}_2(s)}{\partial s}-\frac{\partial\widehat{h}_1(s)}{\partial s})\sin\theta_R(r)\right)\end{aligned} \tag{5.28}$$

where s has now been used as the along-track coordinate, $(\widehat{c}_1(s),\widehat{c}_2(s),\widehat{h}_1(s),\widehat{h}_2(s))$ is the cross-track motion estimate from the navigation data, and $\widehat{h}_T$ is the target terrain height supplied from the external DEM. The estimate is smoothed by applying a rectangular filter, with the filter length set equal to the synthetic aperture length for the given azimuth line. Calculating (5.28) for each range bin results in a synthetic azimuth misregistration image. The topographic misregistration can be subtracted from the azimuth misregistration obtained by, for example, the spectral diversity algorithm. The corrected misregistrations can then be used as input to a differential motion estimation algorithm. Thus, the azimuth shifts input to, for example, the RME algorithm (section 4.4.2) can be written:

$$\delta_{x,RME} = \delta_{x,SDC} - \widehat{\delta}_{x,topo} \tag{5.29}$$

where $\delta_{x,SDC}$ is the azimuth misregistration estimate obtained by the spectral diversity algorithm.

The method described above can be used to subtract the topography-induced misregistration before RME estimaton. This way, the RME estimate can be improved, and it also gives an idea of the errors that can be expected if an external DEM is not available. The method does not, however, correct the topography-induced misregistrations. Thus, it is applicable when the topography induced misregistrations are small enough that the coherence is not severely affected (see (4.12)), but large enough that the baseline estimate may be affected.

In the event that the influence of the topography-induced azimuth misregistrations on the coherence cannot be neglected, topography-dependent motion compensation must be applied, but this complicates the processing considerably, and has not been examined in this work. A method for topographic motion compensation that has been applied in conjunction with the RME algorithm is given in [36].

5.3 Implementation

MATLAB programs were designed to read the output files setup and radar data files from the `sarif` SAR processor, developed by Johan Mohr, which has been used in this work. A tiled image format and input/output routines for MATLAB were developed to allow easy range and azimuth access to large image files. Then, the methods for non-parametric motion estimation were implemented, including the improvements described in this chapter. A block diagram of the implemented routines is shown on Figure 5.2.

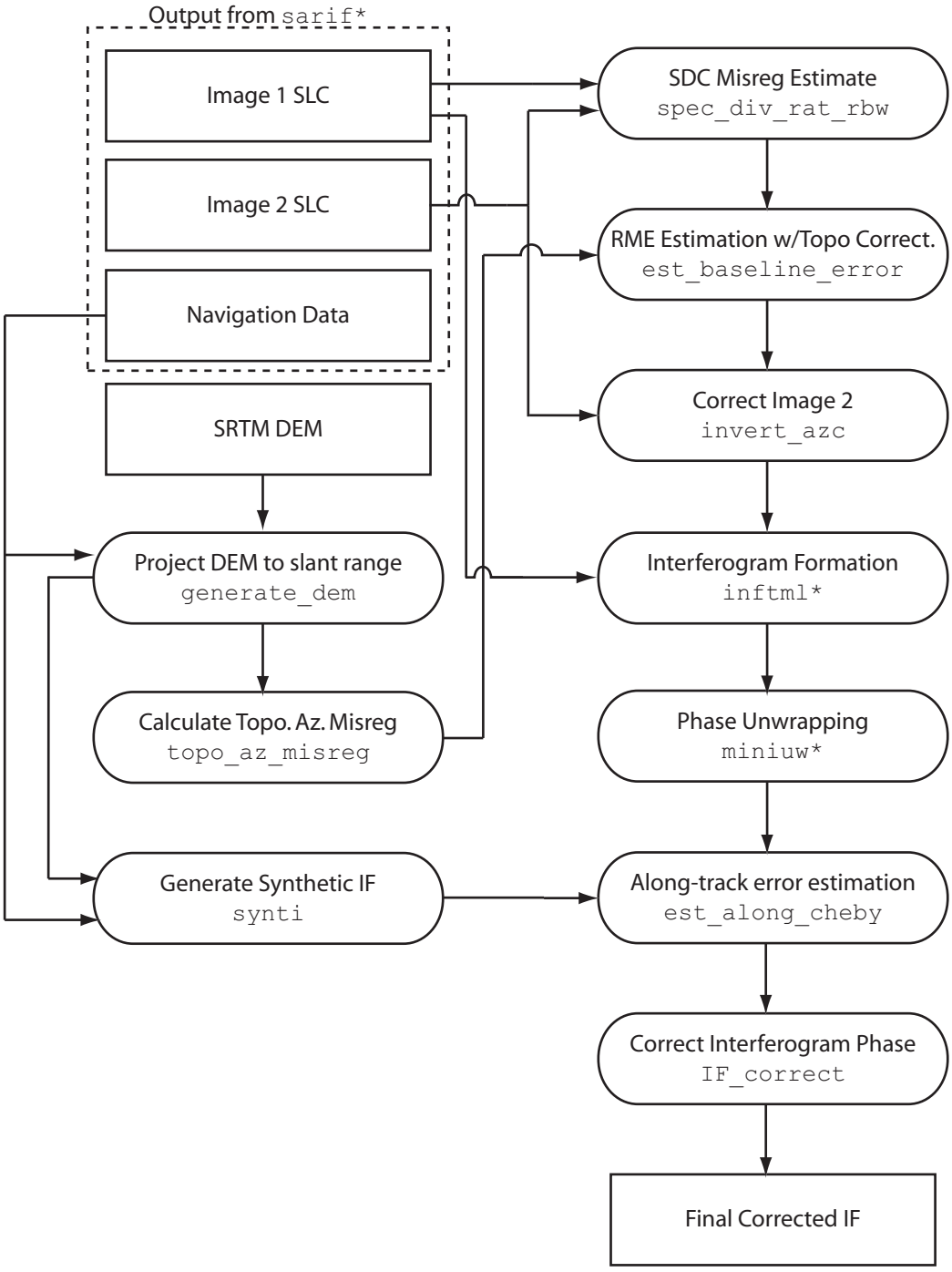

Figure 5.2: MATLAB implementation of non-parametric motion estimation with the improvements described in Chapter 5. An asterisk indicates an external program not developed by the author. Note that the estimation of a constant cross-track baseline error and an absolute phase offset is included in `est_along_cheby`.

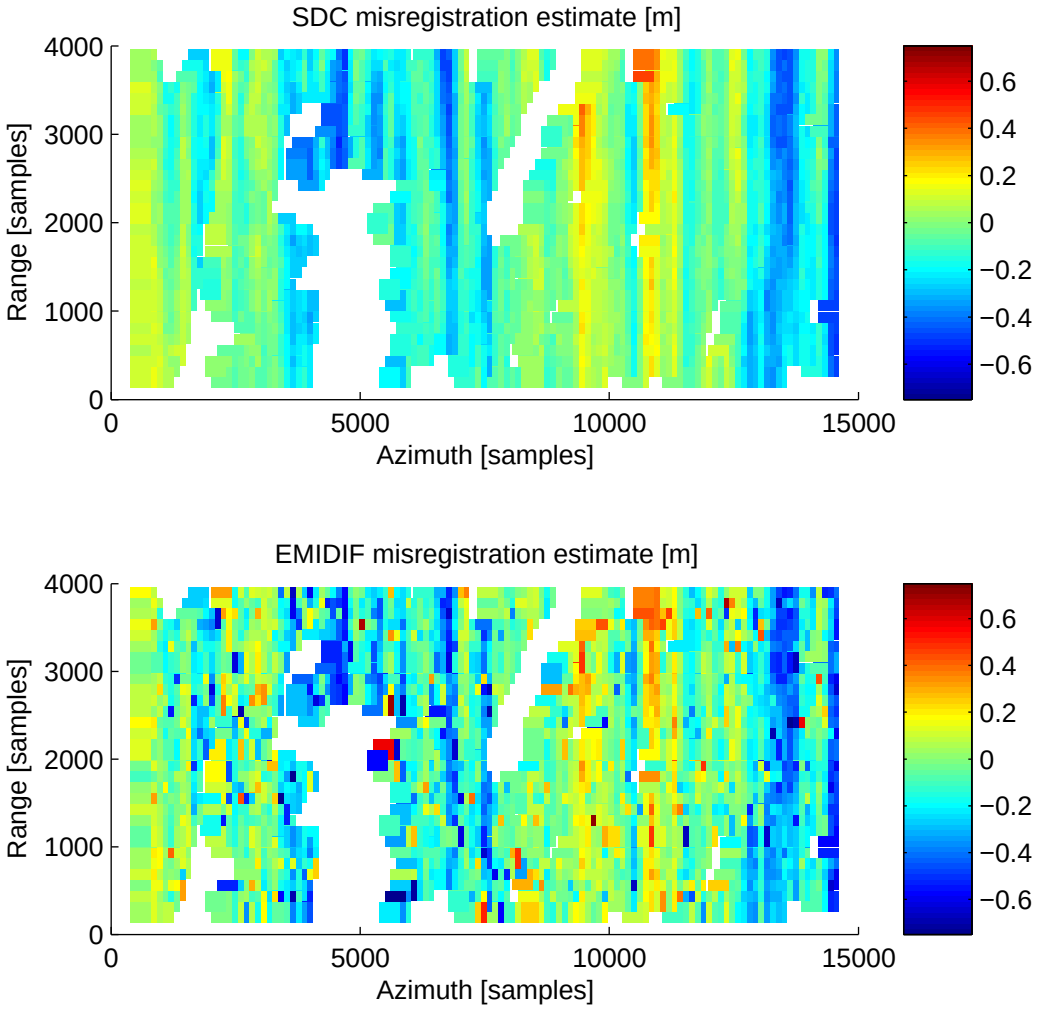

Figure 5.3: Comparison of SDC and `emidif` algorithms for azimuth misregistraton estimation.

5.3.1 Implementation of SDC and RME algorithms

The Spectral Diversity algorithm, described in section 4.3.1, was implemented in MATLAB, to be used on focused EMISAR data. For verification, the spectral diversity algorithm was compared to the `emidif` speckle correlation algorithm for misregistration estimation using the two SAR images in Section 6.2. Only azimuth misregistrations were considered. The filter applied to the SDC estimate was a rectangular filter of the same dimensions as the patch size used in `emidif`, and the SDC estimates were extracted at the 2667 positions at which valid `emidif` estimates were available. The two misregistration images are shown in Figure 5.3. It is seen that the images resemble each other, but the `emidif` estimates are considerably more noisy. The mean difference of the `emidif` and SDC estimates is 0.9 mm whereas the RMS value of the differences is 16 cm. This is probably caused by the noise on the `emidif` estimates.

The RME algorithm, as described in section 4.4.2, was also implemented in MATLAB. This takes as input an azimuth misregistration image, a coherence mask, and

navigation data output by `sarif`. The coherence mask is used to exclude decorrelated areas from the RME estimation. Note that the coherence mask is not shown on the block diagram.

A verification of the implemented SDC and RME processing was carried out by processing the L-band data used in section 6.2 and performing the RME estimation. Then the motion data for one image were artificially modified with a slow sinusoidal variation (one half period along the 25 km image) in the horizontal cross-track coordinate. The vertical motion data were modified by the sum of a slow and a fast (six periods along the image) sinusoidal error. All sinusoids had a peak-to-peak variation of 6 cm. The image was refocused, and a new SDC misregistration estimation and RME estimation was carried out. Ideally, the difference between the estimated residual motion errors should be equal to the artificial errors. In practice, the deviation from the artificial error was less than 2 mm, with no systematic variation except for the constant baseline error, which cannot be detected by the RME algorithm.

5.3.2 Implementation of improved RME

The DEM projection (section 5.2.2) was implemented in MATLAB based upon existing FORTRAN routines for conversion between $(\mathrm{Lat}, \mathrm{Lon}, \mathrm{Alt})$ and (s, c, h) coordinate systems. These were vectorized and converted to MATLAB, and a routine for reading SRTM DEM data was written. This could be modified to other types of elevation data also. The resampling of the slant range projected DEM to image coordinates was accomplished with the MATLAB `griddata` routine, which performs bicubic interpolation on unevenly spaced data.

The synthetic interferogram generation (section 5.2.3) and topographic compensation (section 5.2.4) were implemented in MATLAB. The topographic compensation routine generates a synthetic misregistration image from the navigation data and the DEM data, and this synthetic image is subtracted from the SDC misregistration image prior to RME estimation.

Finally, the along-track motion estimation proposed in section 5.1.1 was implemented in MATLAB, including the modification to use Chebyshev polynomials. Note that this along-track error estimation also estimates a constant cross-track baseline offset, which must be estimated from the topography. MATLAB is well suited for least-squares solution of large systems like (5.15).

Chapter 6

Experimental Evaluation

The RME algorithm (section 4.4) and its suggested improvements (chapter 5) have been implemented in MATLAB and tested on EMISAR data. Two different zero-Doppler RTI data sets have been used, both with a temporal baseline of less than an hour. The first is HH-polarisation L-band ($\lambda = 24$ cm) data set (Flight `fl075` maps `m1314` and `m1352`) acquired in June 1999 over Foulum in Jutland, a mainly agricultural scene. Kinematic GPS data are available here, and the baseline used is sensitive to topography. The strip length is 4096×15000 samples (range×azimuth), or 6.14 km× 22.5 km, with the nominal 1.5 m resolution in both dimensions. The data were obtained from an altitude of 25000 feet, with a near range incidence angle of 37.4°.

The second data set (Flight `fl045` maps `m0757` and `m0841`) is a HH-polarisation C-band set ($\lambda = 5.66$ cm), and acquired in July 1996. Here the focused strip is 6144×65536 samples, or 9.2 km×98.3 km, extending from Foulum out into Kattegat. The data were obtained from an altitude of 41,000 feet, with a near range incidence angle of 36.7°. Only the Gulfstream G3 GPS and EMISAR INU (not EGI) navigation data are available for this scene. The areas covered by the two data sets are illustrated in Figure 6.1. The topography variations over the scenes are on the order of 100 m, as can be seen from the topographic maps in Figures 6.4 and 6.16.

6.1 Data processing

The data processing carried out in this chapter is illustrated in Figure 6.2. The SAR images were initially focused to 1.5 m range and azimuth resolution using the `sarif` range-Doppler processor and associated tool chain, developed by Johan Mohr [21]. Before the initial focusing, the INU navigation data were corrected by a third-order polynomial fit of each of the (s, c, h) coordinates to the GPS data to correct for INU drift. The data were focused to common reference tracks (i.e. one reference track for each dataset). For the C-band data this is natural, since the actual baseline was small (less than 10 m). For the L-band data, it could be considered to use separate reference tracks, due to the relatively large baseline, but for simplicity, a common reference track was also used here.

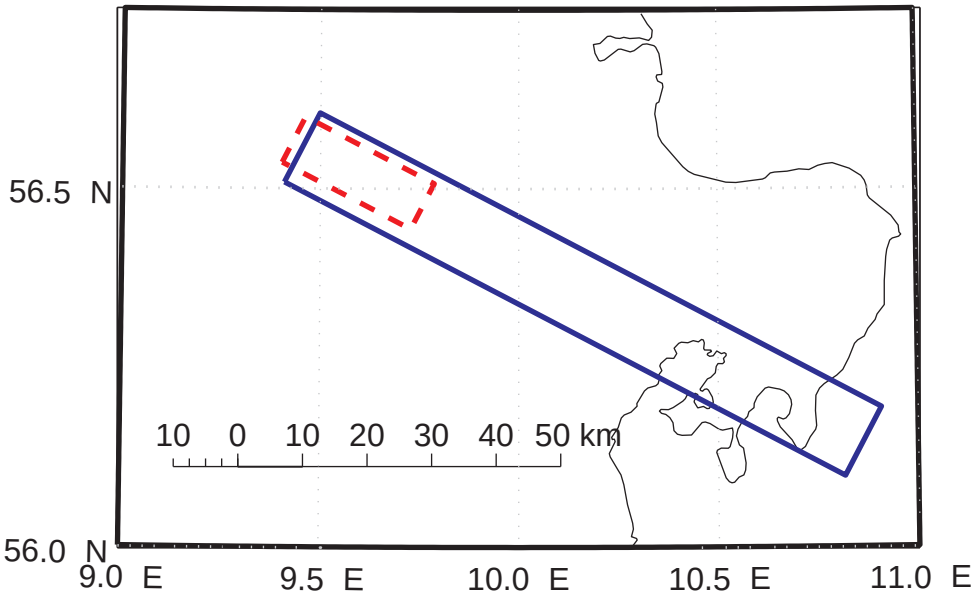

Figure 6.1: Focused areas for `fl045` C-band (blue solid) and `fl075` L-band (red dashed) RTI data sets.

6.2 Evaluation with L-band data

6.2.1 Initial processing

For the L-band data set, a large unexplained delay of approximately 0.6 seconds between the radar data and the navigation data logged by EMISAR was observed. Similar delays have also been seen in data from other of the later EMISAR flights. The problem appears to be in the radar data time stamps since the kinematic GPS data, which are collected independent of EMISAR, align with the EMISAR logged navigation data. Fortunately, EMISAR also stores the navigation data used in online motion compensation in the radar data. Although this is in a local (s, c, h) system defined by EMISAR, the h-coordinate is relatively unaffected by the transformation from geographic coordinates. Therefore, this could be correlated with the integrated INU vertical velocities, to get an estimate of the delay. In the `m1314` master image, a delay of the radar data of 0.590 s relative to the navigation data was estimated, versus a delay of 0.586 s in the `m1352` slave image data. When these delays were accounted for, the kinematic GPS-refined INU data were sufficient to coregister the images to within 0.5 m azimuth misregistration (the resolution cell size is 1.5 m×1.5 m). The vertical and horizontal baseline components obtained from the navigation data are shown in Figure 6.3. The corresponding parallel and perpendicular baseline components at near and far range are also shown in the figure.

After the focusing of the L-band data, a (4x4 look) interferogram was formed. The amplitude image, interferogram and coherence images are shown in Figure 6.4. The mean coherence of the scene is 0.8 (0.84 if the temporally decorrelated lakes are excluded), which is reasonable for an L-band agricultural scene in June. As described in section 5.2, an SRTM 90 m DEM was projected to the slant range geometry. This also shown in Figure 6.4, together with the resulting synthetic interferogram (wrapped) generated from the DEM and the navigation data.

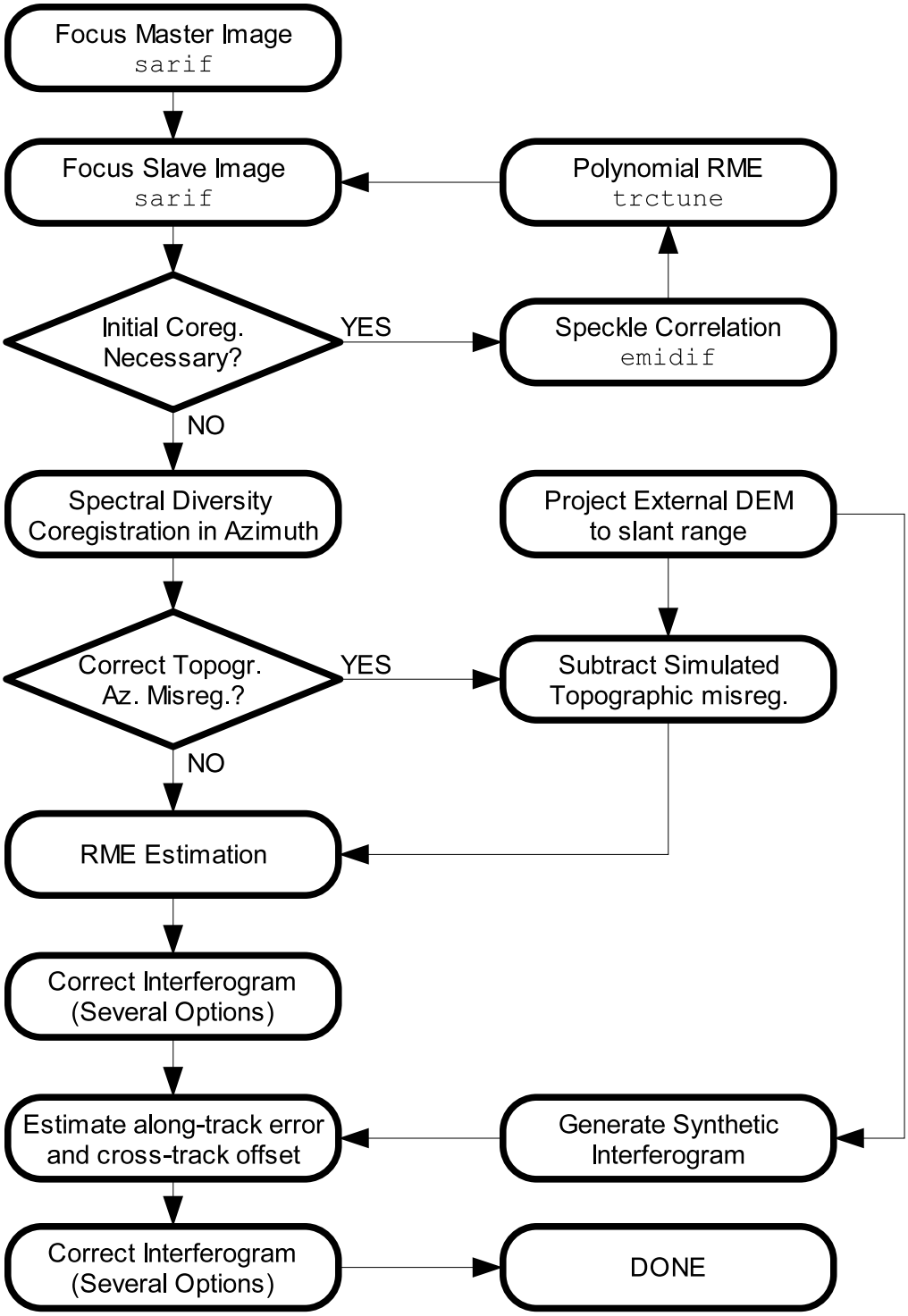

Figure 6.2: Processing flow.

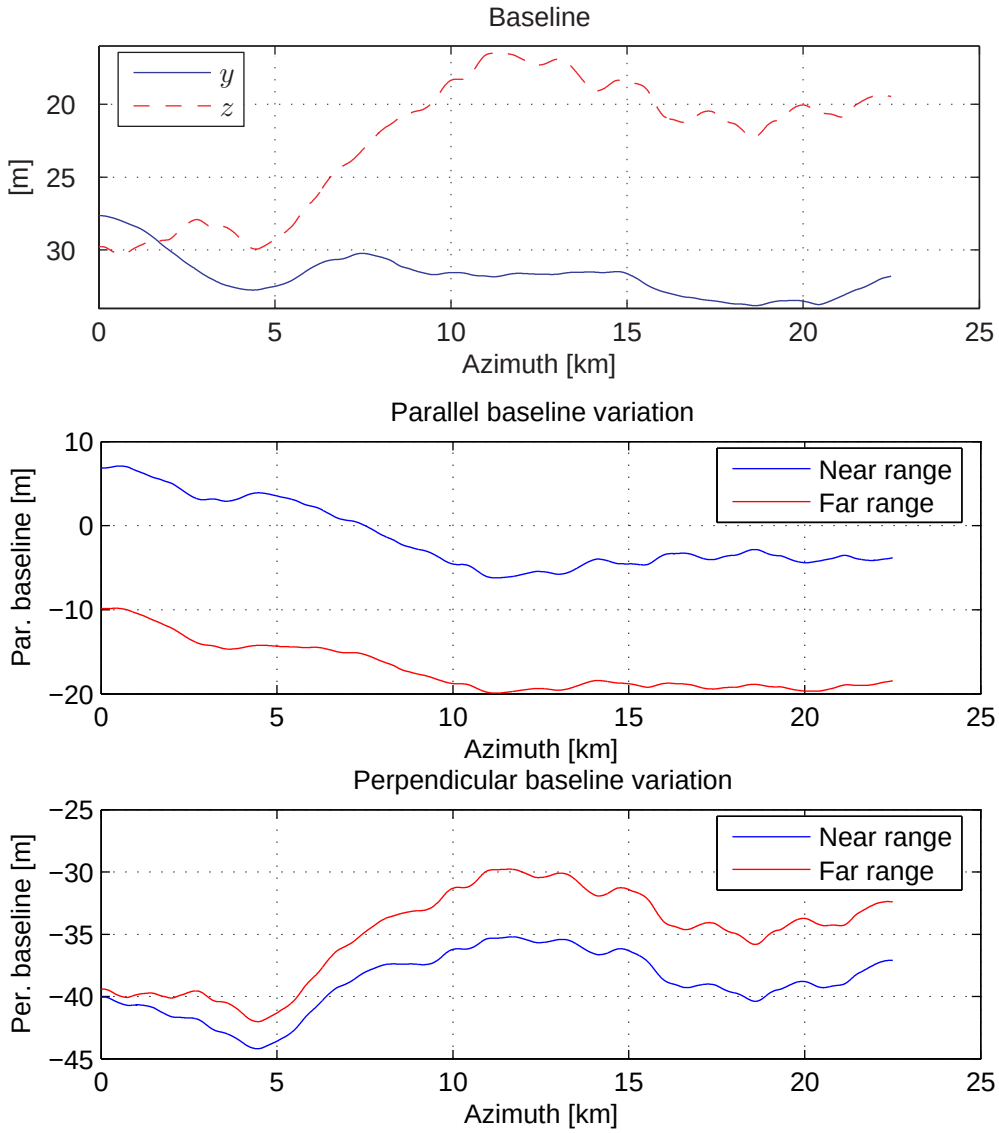

Figure 6.3: Baseline components for the `f1075` L-band data, from navigation data.

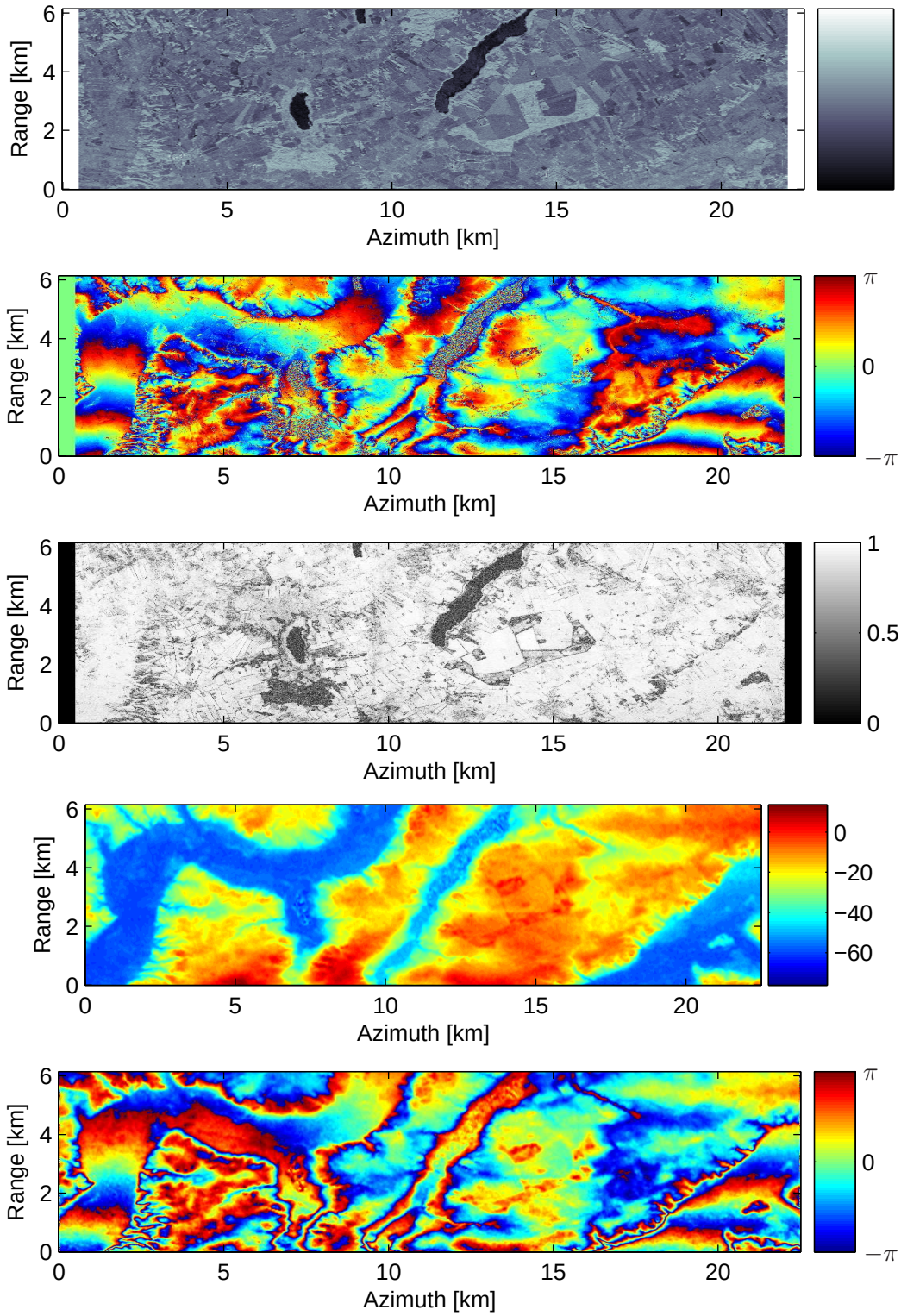

Figure 6.4: `f1075` data after initial focusing and 4x4 multilook, from top down: Amplitude, interferometric phase, coherence, DEM (relative to mocom height), synthetic interferogram from external DEM.

6.2.2 SDC processing

The range and azimuth misregistrations were estimated by the spectral diversity algorithm as described in section 4.3.1. The algorithms developed in principle do not rely on the range misregistration, but it is shown for reference. In both cases, the SDC complex differential interferogram was normalized and filtered using a 201×201 Gaussian kernel before being converted to displacement estimates. The filtering reduces the estimation noise, as well as the impact of small decorrelated areas. Figure 6.5 shows the azimuth misregistration image estimated this way. The major varia-

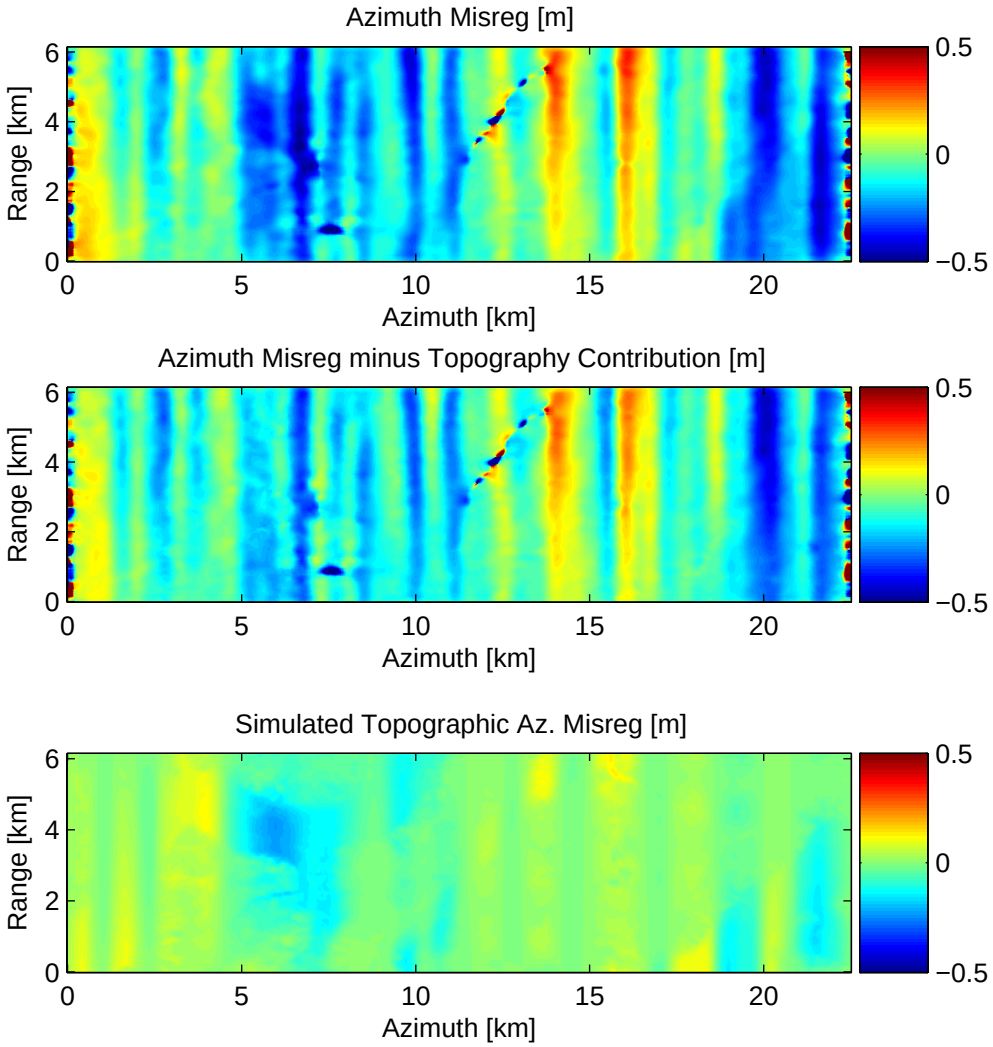

Figure 6.5: Azimuth spectral diversity misregistration estimates for `f1075`, with and without simulated topography-induced azimuth misregistration.

tion of the azimuth misregistration is seen in the azimuth direction. There is also some variation in range, though, indicating that at least part of the misregistration is induced by horizontal cross-track errors. The misregistrations vary rapidly, which suggests that they are caused by an uncompensated delay between radar and navigation data in one or both images. This suspicion is strengthened by the fact that a mean misregistration of -9.6 cm is seen. Of course this could be due to a constant

along-track motion errror, but it could also be caused by an uncompensated delay of 9.6 cm/(240 m/s) = 0.0004 s, and it is likely that the observed 0.6 s radar timestamp delays cannot be estimated completely by the approach mentioned in Section 6.1. The mean misregistration could also be due to a constant vertical velocity error of -9.6 cm/7620 m $\approx 1.3 \times 10^{-5}$ m/m, according to (5.9). This would lead to a linear variation of the vertical error of 0.32 m along the image, which should be visible in the range registration, but this is not the case (see Figure 6.6). It is possible to estimate the delay between radar data and navigation data in each image from the observed azimuth misregistrations [21]. This was attempted, but without succes. Anyway, the effect of such delays are basically differential motion errors (in both along- and cross-track directions), and it provides an opportunity to test the residual motion estimation methods described in this work. This is an area that should be analysed further, though.

Figure 6.5 also shows the simulated azimuth misregistration from topography, obtained by the method described in 5.2.4, and the azimuth misregistration image after subtraction of the simulated topography contribution. The topographic correction seems to remove some of the cloudiness of the original misregistration image, but the effect is minor, and nothing conclusive can be said from this.

The estimated range misregistration is shown in Figure 6.6, together with the range misregistration simulated from the external DEM and the navigation data. Also, the difference between the estimated and the simulated range registration is shown. The expected variations from the evaluation of the external DEM and the navigation data are on the order of 0.5 m, and this is also seen in the range misregistration image. The difference between the two images is most likely due to the differential cross-track errors.

6.2.3 RME estimation and correction

The basic RME algorithm was applied to the azimuth misregistration image to obtain estimates of the residual cross-track motion, as described in 4.4.2. As the mean misregistration is likely due to along-track errors, caused either by an uncompensated delay between radar and navigation data or a constant along-track error (see previous section), it was subtracted before the RME estimation. This is not strictly necessary with the along-track error estimation described in section 5.1.1, and in fact this was tested, as described in 6.2.4.

The estimated motion errors are shown on Figure 6.7, both for the case when the simulated topography was subtracted before RME estimation, and for the case where it was not. It can be seen that in both cases, the estimated errors have the same shape, with a larger variation in the vertical than in the horizontal cross-track component. Without topographic compensation, the total variation in the vertical component is 10 cm, whereas it is 7 cm with topographic compensation. Since the accuracy of kinematic GPS is generally considered to be 5-10 cm this is not unreasonable. The difference in the estimates with and without topography is within 5 cm. This is a large variation compared to the actual estimated errors, but it cannot be concluded from this which estimate is correct.

Since the estimated cross-track errors are small compared to the overall topographic interferometric shifts of up to 0.5 m, it is sufficient to correct the slave image using

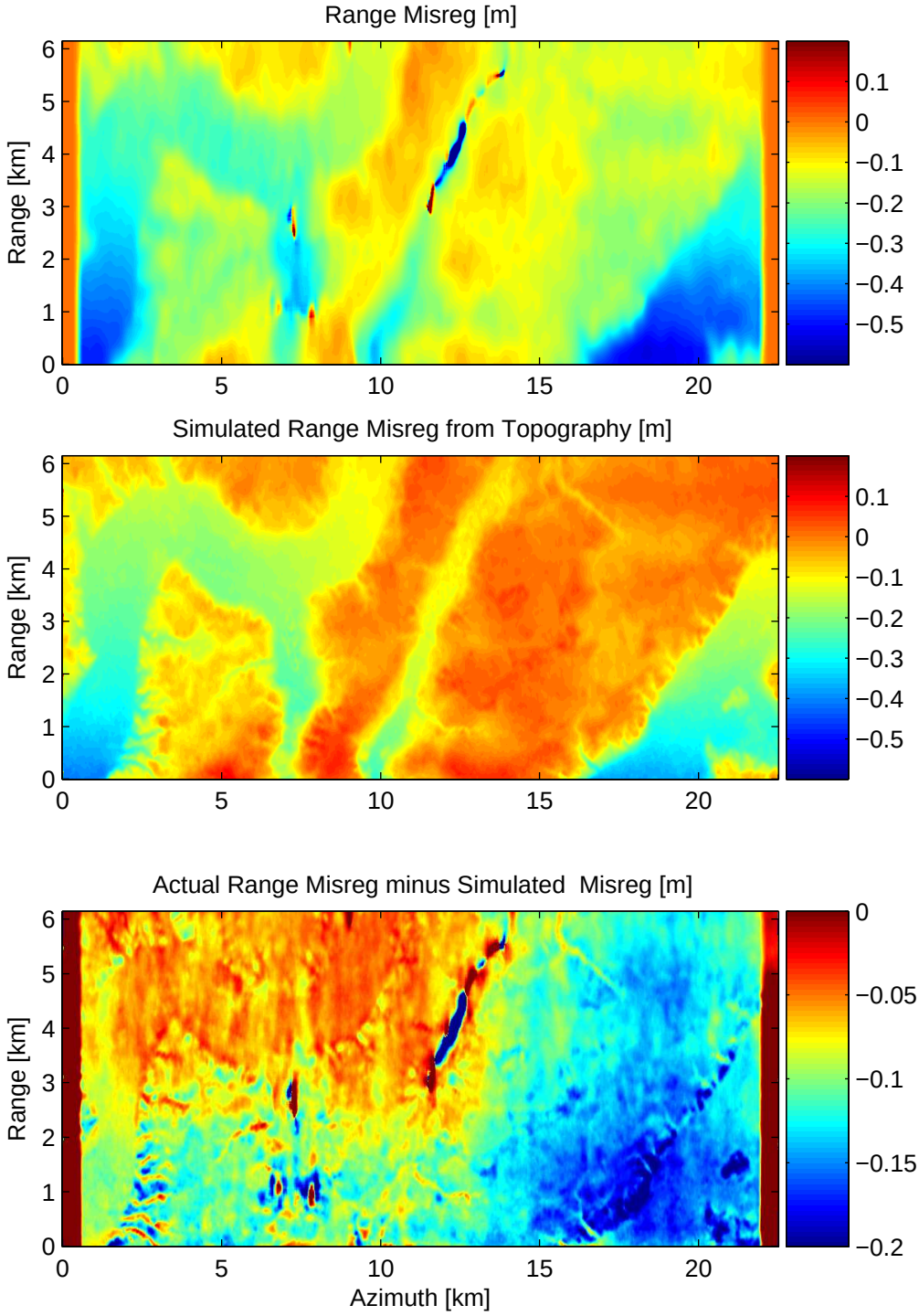

Figure 6.6: (top) Range spectral diversity misregistration estimates for `fl075` data, (middle) Simulated range misregistration from external DEM and navigation data (middle), (bottom) Difference of estimated and simulated misregistrations.

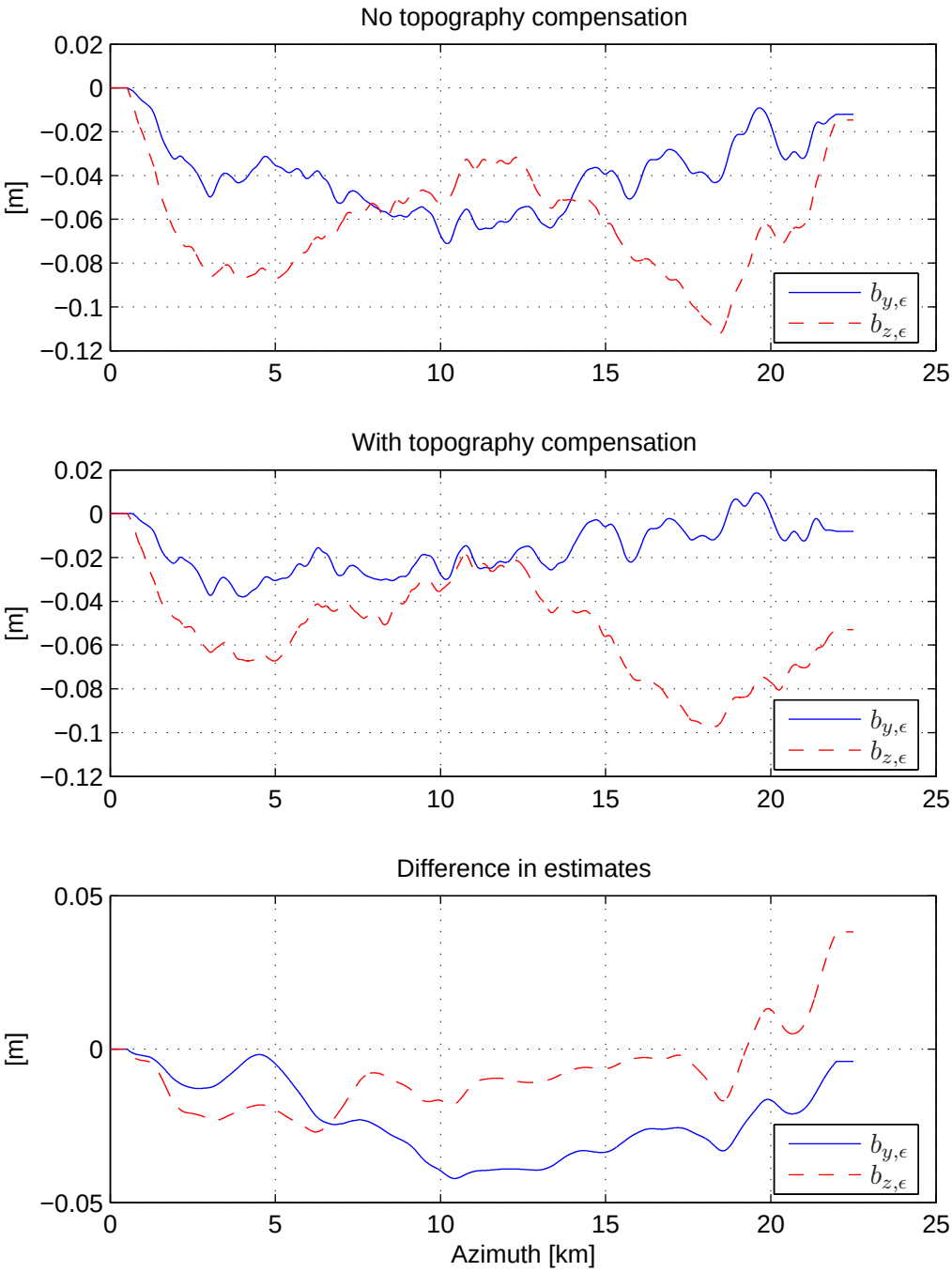

Figure 6.7: `fl075` Cross-track residual errors estimated by basic RME algorithm, (top) Without topography compensation, (middle) With topography compensation, (bottom) Difference in estimates.

only azimuth refocusing (see section 4.5) as this corrects the phase shift and azimuth misregistrations from the residual cross-track motion. This was done for both cases (with and without topographic compensation). The spectral diversity misregistration estimate for the images that were RME corrected without topography compensation is shown on Figure 6.8. The residual misregistration for the images that were corrected with topography compensation is shown on Figure 6.9. Also shown is the simulated residual misregistration due to topography. This is the part of the simulated topographic azimuth misregistration that is not modeled by the RME estimation. For the images corrected with topography compensation, the expected residual azimuth misregistration is simply the estimated topographic misregistration which was subtracted before RME correction. In the case where topographic compensation is not applied prior to RME, part of the topographic misregistration is interpreted as due to across-track errors. The simulated residual misregistration was found by using the RME correction on the synthetic topographic misregistration image. The figure also shows the difference between the actual and the simulated misregistrations, which should ideally be zero. In both cases, the simulated residual misregistration resembles the actual misregistration. The difference between the estimated and simulated residual misregistration shows non-systematic variations of ± 10 cm, but there seems to be a slight correlation between the difference image and the simulated topographic misregistration, suggesting that the topographic misregistration is slightly undercompensated. This could be caused by the lower resolution of the SRTM DEM compared to the image resolution. It could also be caused by the fact that a rectangular filter of length equal to the aperture length is used in the topographic misregistration estimation (see section 5.2.4) but the azimuth compression uses a weighted compression filter to suppress sidelobes, implying a shorter effective aperture. The EMISAR flight control system causes a vertical oscillation of the flown track with a period of approximately 1250 m. This gives rise to azimuth misregistrations, but the synthetic aperture length at midswath is approximately 800 m, so the motion cannot be considered linear within the aperture. The longer the effective aperture, the more the oscillating motion will be averaged out, implying smaller azimuth shifts, and this might explain the residual misregistrations. It was attempted to adjust the filter length used in the topographic compensation to better match the effective aperture length, but the results were inconclusive. Actually it was found that when the filter became too short, the topographic compensation overcompensated the misregistration images, so this is a subject worthy of further study.

The coherence histograms before and after the RME correction are shown on figure 6.10. The coherence is generally high to begin with, but a slight improvement is seen for the corrected images. There is no distinguishable difference between the coherence histograms with regards to topography misregistration compensation. This is not surprising, as the topography misregistration effect is small compared to the cross-track induced azimuth misregistrations (see figure 6.5).

6.2.4 Along-track motion estimation

The RME corrected interferograms were Goldstein-filtered and unwrapped using a Minimum Cost-unwrapper, `miniUW`. Then the synthetic interferogram (see Figures 6.4 and 6.6 for the wrapped and unwrapped synthetic interferogram, respectively)

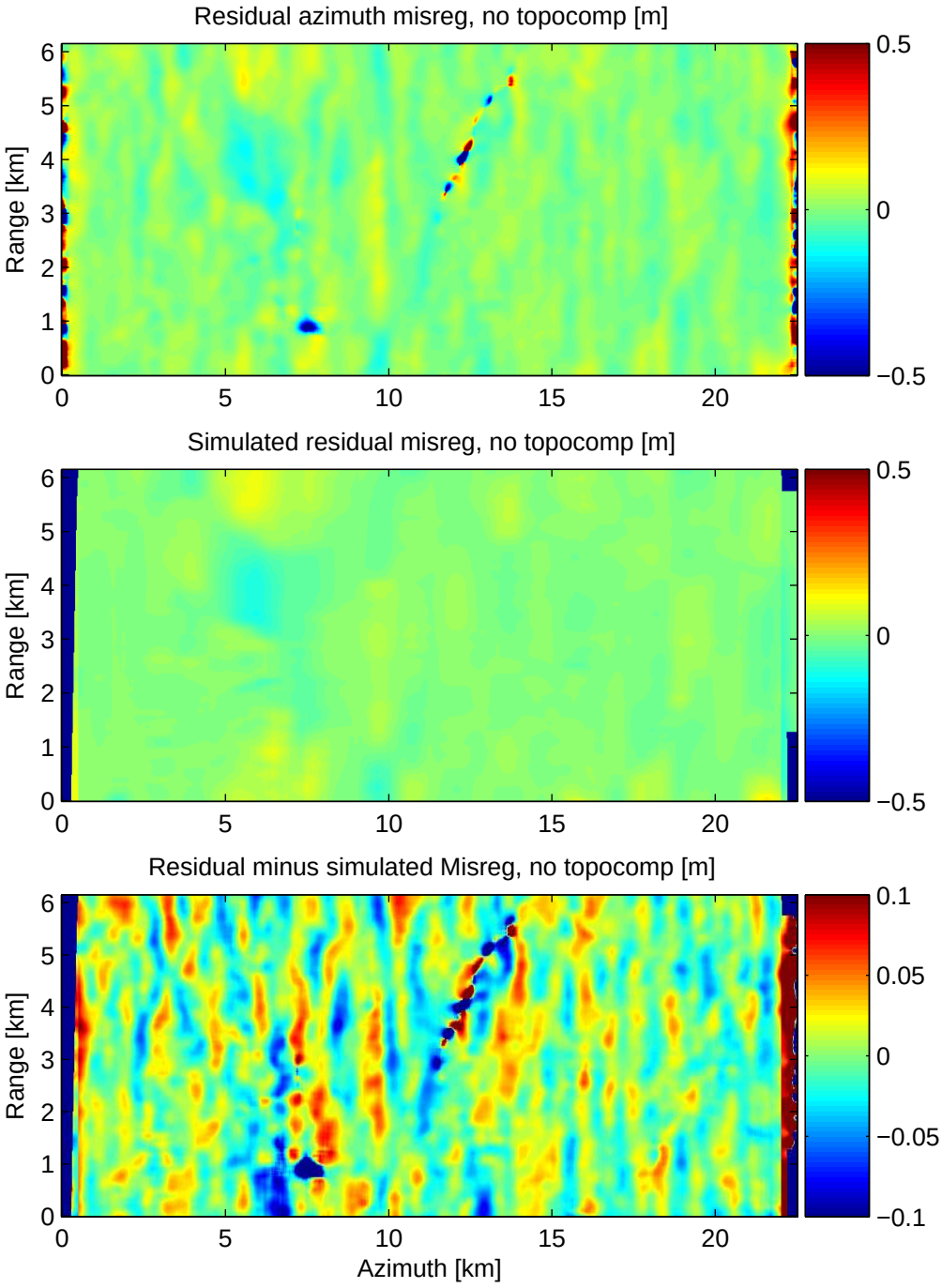

Figure 6.8: Residual azimuth misregistration after RME correction without topographic correction,(top) Estimated residual misregistration (middle) Simulated residual misregistration due to topography, (bottom) Difference between estimated and simulated residual misregistration.

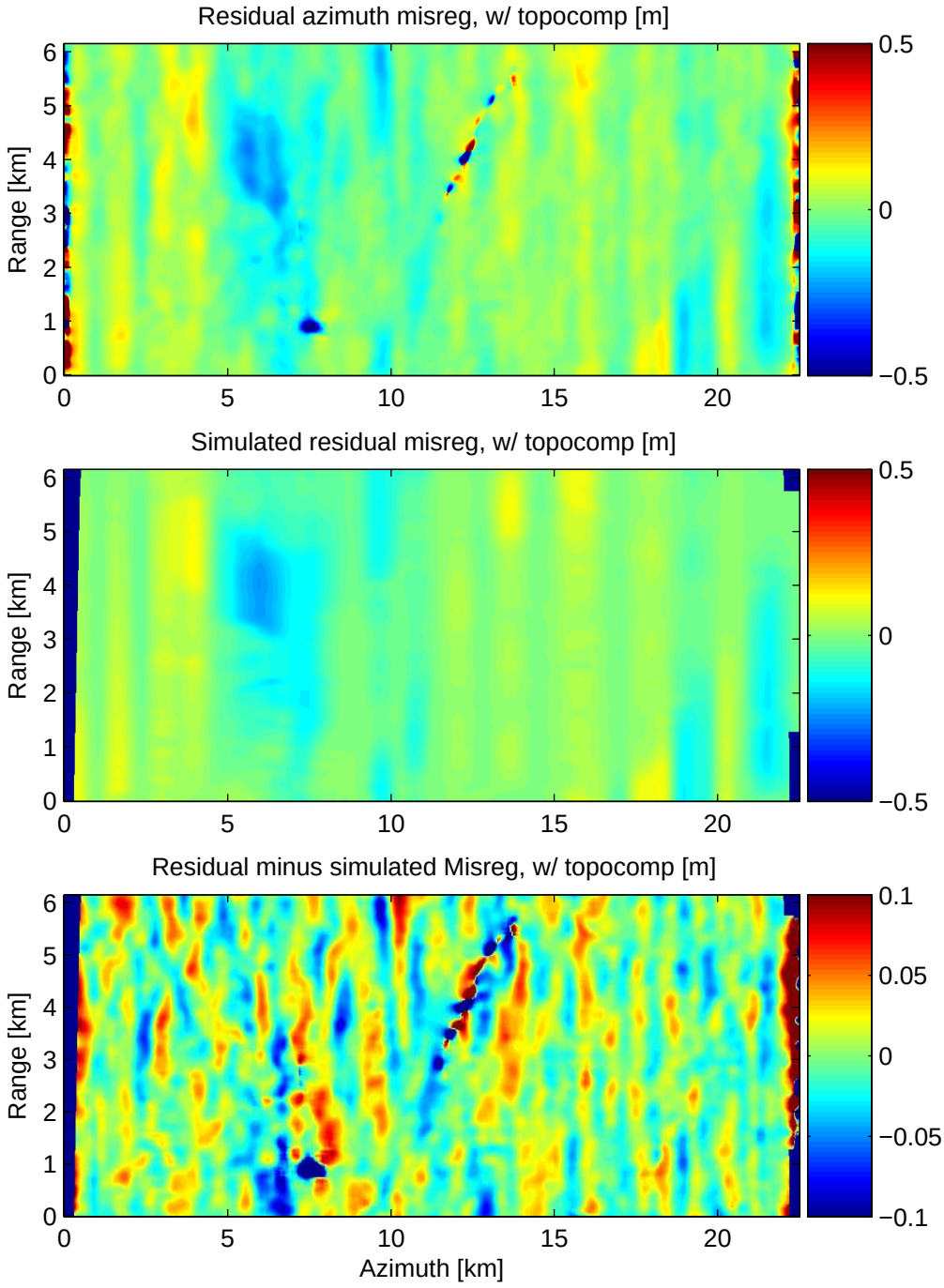

Figure 6.9: Residual azimuth misregistration after RME correction with topographic correction, (top) Estimated residual misregistration (middle) Simulated residual misregistration due to topography, (bottom) Difference between estimated and simulated residual misregistration.

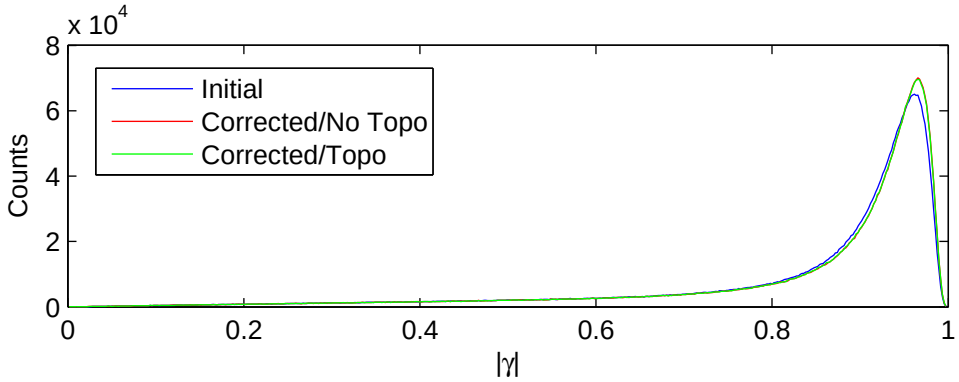

Figure 6.10: Coherence histograms before and after correction.

Case	$\Delta\widehat{r}_{abs}$ [cm]	$\widehat{b}_{y,\epsilon,0}$ [cm]	$\widehat{b}_{z,\epsilon,0}$ [cm]	$\widehat{b}_{x,\epsilon,0}$ [cm]	$\widehat{b}_{x,\epsilon,1}$ [cm]	$\widehat{b}_{x,\epsilon,2}$ [cm]
$\widehat{\boldsymbol{Q}}$	−92.2	−24.6	7.1	10.8	−2.3	−5.4
$\widehat{\boldsymbol{Q}}_m$	−92.2	−25.1	6.8	1.2	−2.3	−5.3
$\widehat{\boldsymbol{Q}}_t$	−78.0	−25.5	1.1	10.2	1.3	−3.4
$\widehat{\boldsymbol{Q}}_{tm}$	−78.0	−25.7	1.1	0.6	1.1	−3.4

Table 6.1: Estimated residual motion parameters using the along-track estimation described in section 5.1.1. Subscript m refers to the case where the overall azimuth misregistration mean of -9.6 cm was subtracted before RME estimation. Subscript t indicates that the azimuth misregistration was topography-corrected before RME estimation. Note that the $b_{x,\epsilon}$ coefficients given are Chebyshev coefficients, and are thus a measure of the magnitude from each term.

.

was subtracted in order to get an idea of the differential motion errors before and after compensation. It is not necessary to calculate a new synthetic interferogram when the RME-correction is applied as azimuth refocusing, as this corresponds to a motion compensation to the initial tracks. The residual interferograms are shown on Figure 6.11 (phase has been converted to range shift), where the mean has been subtracted in each case, as the absolute phase offset is unknown. A range variation is seen in all cases, which is probably due to a constant baseline offset, which cannot be detected with the basic RME algorithm. This can, however, be calibrated out using the approach described in section 4.4.3. Also, a variation in azimuth is observed, although part of it is linear for the RME corrected interferograms, and this part could be calibrated out using a linear fit.

The along-track error estimation described in section 5.1.1 was carried out for both of the RME-corrected residual interferograms using a second order polynomial model of the along-track error. 3435 samples distributed evenly over the residual interferograms were used to solve (5.15). The estimated residual motion parameter vectors, $\widehat{\boldsymbol{Q}}_m$ and $\widehat{\boldsymbol{Q}}_{mt}$, are shown in Table 6.1 (see also (5.18)). Note that the fit interval used in along-track motion estimation goes from 0.67 km to 21.5 km, so the Chebyshev coefficients $\widehat{b}_{x,\epsilon,0}, \widehat{b}_{x,\epsilon,1}, \widehat{b}_{x,\epsilon,2}$ should be interpreted accordingly. Also shown are the results, $\widehat{\boldsymbol{Q}}$ and $\widehat{\boldsymbol{Q}}_t$ obtained when the same RME processing and correction was car-

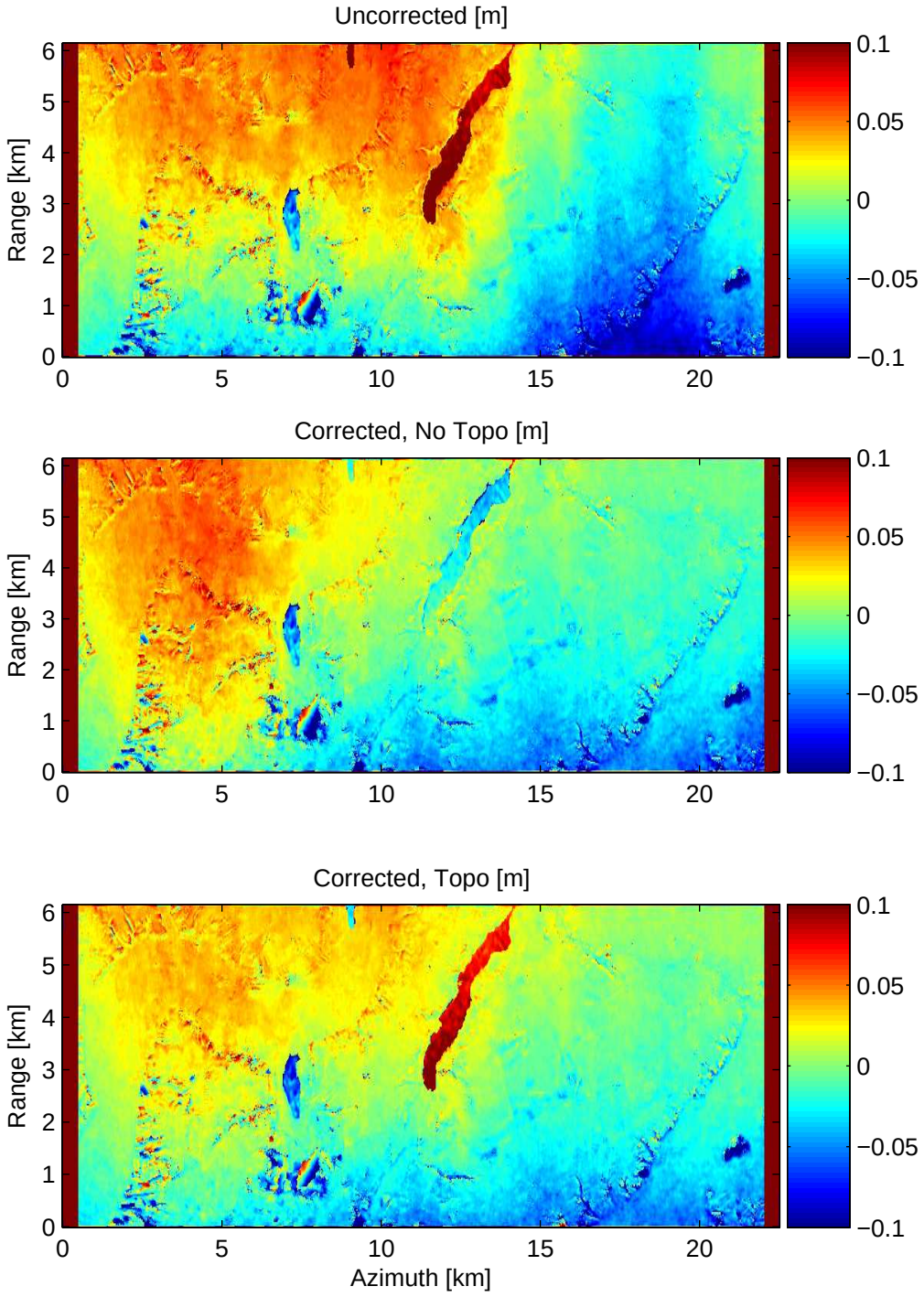

Figure 6.11: Residual interferograms (converted to range shift) after subtraction of synthetic interferogram. (top) No RME correction, (middle) RME corrected without topographic misregistration compensation, (bottom) RME-corrected with topographic misregistration compensation. In all cases, the mean has been subtracted as the absolute phase offset is unknown.

ried out, but with the difference that the mean azimuth misregistration of -9.6 cm was *not* subtracted before RME estimation. It is seen that the −9.6 cm centimeter azimuth misregistration is accurately modeled by $\widehat{b}_{x,\epsilon,0}$ in each case, with minor variations of less than 5 mm in the other parameters.

Looking at the difference in the parameters estimated with and without topography compensation (i.e, $\widehat{\boldsymbol{Q}}_m$ vs. $\widehat{\boldsymbol{Q}}_{mt}$) a 14.2 cm difference in $\Delta\widehat{r}_{abs}$, the main part of which is probably a phase ambiguity of 2π (equivalent to 12 cm) with the L-band wavelength of 24 cm. This still leaves a difference of 2.2 cm, but also variations of several centimeters in the other parameters are seen, noticably $\widehat{b}_{z,\epsilon,0}$ which changes by 6 cm. Some of this can be explained by the difference in the estimated differential motion errors (see Figure 6.7), but the mean difference between the estimated vertical cross-track motion corrections with and without topography compensations are only 7 mm, so this does not explain all. It was attempted to use a higher order polynomial model for the residual along-track error, but the estimated $\tilde{b}_{x3}$ was only 7 mm, with little changes in the other parameters. When comparing the estimated constant differential motion error $(\widehat{b}_{y,\epsilon,0}, \widehat{b}_{z,\epsilon,0})$ to the range misregistration with simulated topography contribution subtracted (bottom of Figure 6.6) there appears to be an inconsistency. The constant differential motion error should be visible in the range misregistration at the start of the image. With the values of $(\widehat{b}_{y,\epsilon,0}, \widehat{b}_{z,\epsilon,0})$ in Table 6.1 ($\widehat{\boldsymbol{Q}}_t$), a range misregistration of 16 cm is expected, but from Figure 6.6, the observed misregistration at near range is approximately -10 cm. This suggests that the constant baseline offset and absolute phase error is modeled incorrectly. An obvious way of doing this is to use the range misregistration in the absolute phase estimation [27]. However more work is needed to integrate this with the along-track estimation. It was attempted to use the residual range misregistration image (Figure 6.6 bottom) as input to the along-track error estimation instead of the residual interferogram (5.12). In this case, an absolute phase offset was not estimated, and the resulting estimates were $\widehat{b}_{y,\epsilon,0} = 0.2$ cm, $\widehat{b}_{z,\epsilon,0} = 12.0$ cm, $\widehat{b}_{x,\epsilon,0} = 0.6$ cm, $\widehat{b}_{x,\epsilon,1} = 0.8$ cm, and $\widehat{b}_{x,\epsilon,2} = -4.6$ cm. These values should be compared to ($\widehat{\boldsymbol{Q}}_{tm}$) in Table 6.1. The estimated along-track motion using the residual range registration is close to the one estimated using the residual interferogram. However, the constant baseline offset is off, and further work is needed to analyze this.

Using the estimated motion parameters of Table 6.1, a final vertical motion correction can be calculated according to (5.21), and this shown on Figure 6.12. The cross-track correction $\tilde{b}_{z\epsilon}$ is a relative correction with respect to the inital RME-estimated cross-track errors on Figure 6.7, and the estimated constant baseline offset has been added. The motion correction was implemented here as a simple phase correction of the RME-corrected residual interferograms to obtain final residual interferograms. Another approach would be to repeat the focusing done after the initial RME estimation, but using now the final residual motion estimate. This was not done for these data, but in the C-band case, a complete refocusing using corrected navigation data was performed, see Section 6.3.

The final corrected residual interferograms should ideally be perfectly flat if the motion errors were estimated correctly and the external DEM was perfect. The actual residual interferograms are shown in Figure 6.13, where it is the absolute value of the residual interferograms (converted from phase to range) that is plotted to illustrate the differences. Except for the temporal+volume decorrelated areas (see Figure 6.4), the final deviations from the synthetic interferogram are below 2.5 cm in

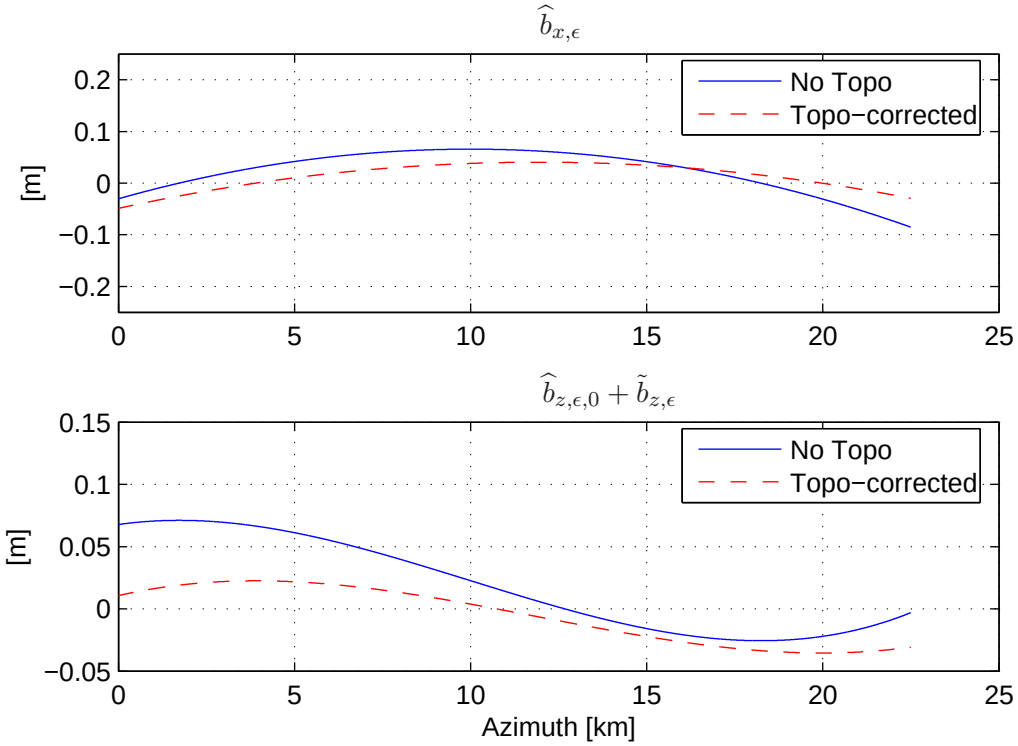

Figure 6.12: Final motion correction estimated by the along-track error estimation.

both the topography-compensated and the non-compensated case. The topography-compensated interferogram seems to be slightly flatter than the non-compensated, especially at the left edge and around 5 km azimuth. We observe from Figure 6.5 that the latter position is also where significant maximum topographic correction was applied. Only in the top right part of the image, the non-compensated interferogram is slightly flatter. The RMS value of the residual phase deviation (if we do not count in the large incoherent areas) is equivalent to 1.3 cm with the topographic compensation and 1.4 cm without, so this is a slight improvement. Part of this variation could be due to atmospheric effects. As mentioned in section 4.1.2, the typical RMS range shifts from atmospheric effects lie in the range 2 mm to 1.7 cm at C-band. If the same applies at L-band, this could explain some of the residual RMS variation. The final corrected interferogram phases were also inverted to terrain height and compared to the SRTM DEM. Of course the data have been corrected using this DEM, but this gives an idea of the high-frequency differences. In this case, the RMS terrain height difference, compared to the external DEM was 3.4 m without topography compensation and 3.2 m with topography compensation. In [37] it is mentioned that the RMS height noise on the SRTM C-band DEM is on the order of 3 m, so results better than this cannot be expected.

To compare the along-track correction method with another method for interferogram calibration, a simpler DEM calibration was performed on the RME-corrected residual interferograms. Here the constant baseline offset was estimated as described in 4.4.3, and a mean linear phase in azimuth was subtracted. This approach has also been used in [38]. Converting these calibrated phases to terrain height, RMS values of 3.6 m (without topographic correction) and 3.4 m (with topographic correction) were obtained. A similar DEM calibration can also be performed on the non-RME

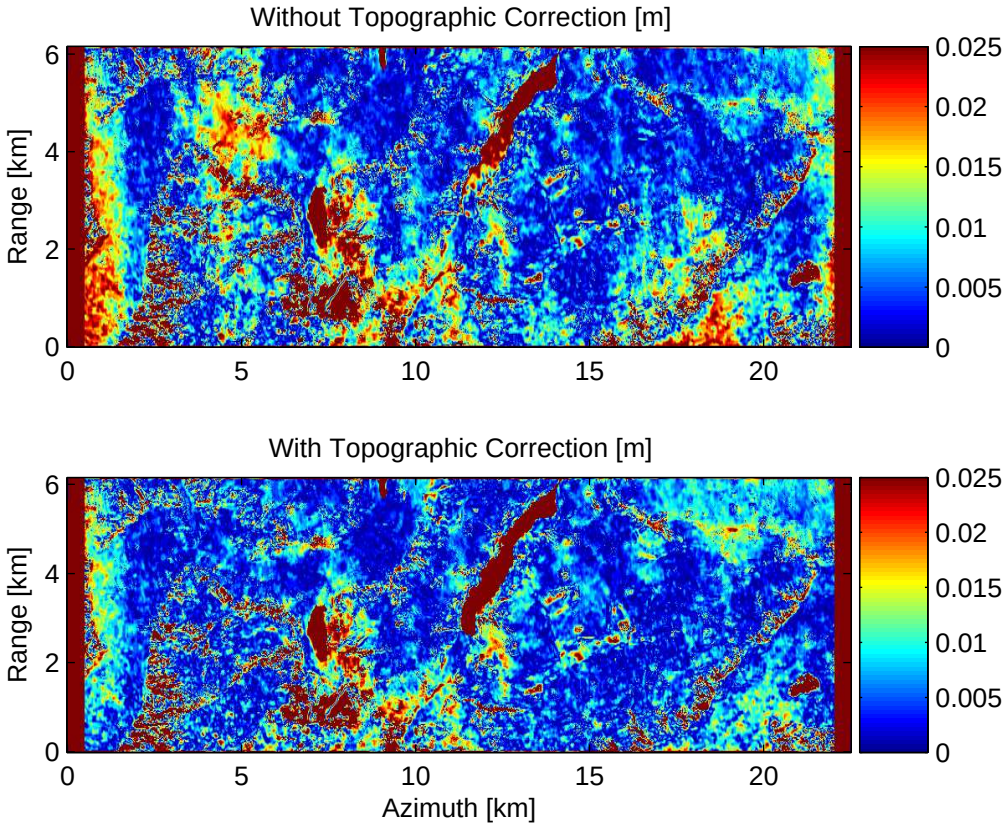

Figure 6.13: Absolute value of final corrected residual interferograms (converted to range shift) after RME-estimation and along-track correction, (top) without topographic compensation, (bottom) with topographic compensation. These should be compared 6.11

corrected interferogram, and in this case, the RMS terrain height deviation from the external DEM becomes 5.7 m, so the main improvement comes from the initial RME correction.

6.3 Evaluation with C-band data

6.3.1 Inital processing

For the C-band data, only the Gulfstream GIII P-code GPS data were available for refining the INU data before initial focusing (see section 6.1). A speckle correlation coregistration (using the `emidif` program) of the initially focused data, showed range misregistrations of up to 5 m and azimuth misregistrations of up to 12 m. The `emidif` misregistration estimates were used in the `trctune` program, which calculates a polynomial differential motion estimate (see section 4.4.1 and [30]). The misregistrations and estimated polynomial baseline corrections are shown in Figure 6.14, together with the horizontal and vertical baseline components as estimated from the polynomially corrected navigation. On Figure 6.15 is shown the variation of the parallel and perpendicular baselines components. These are small, as the desired baseline for these two maps was 0 m.

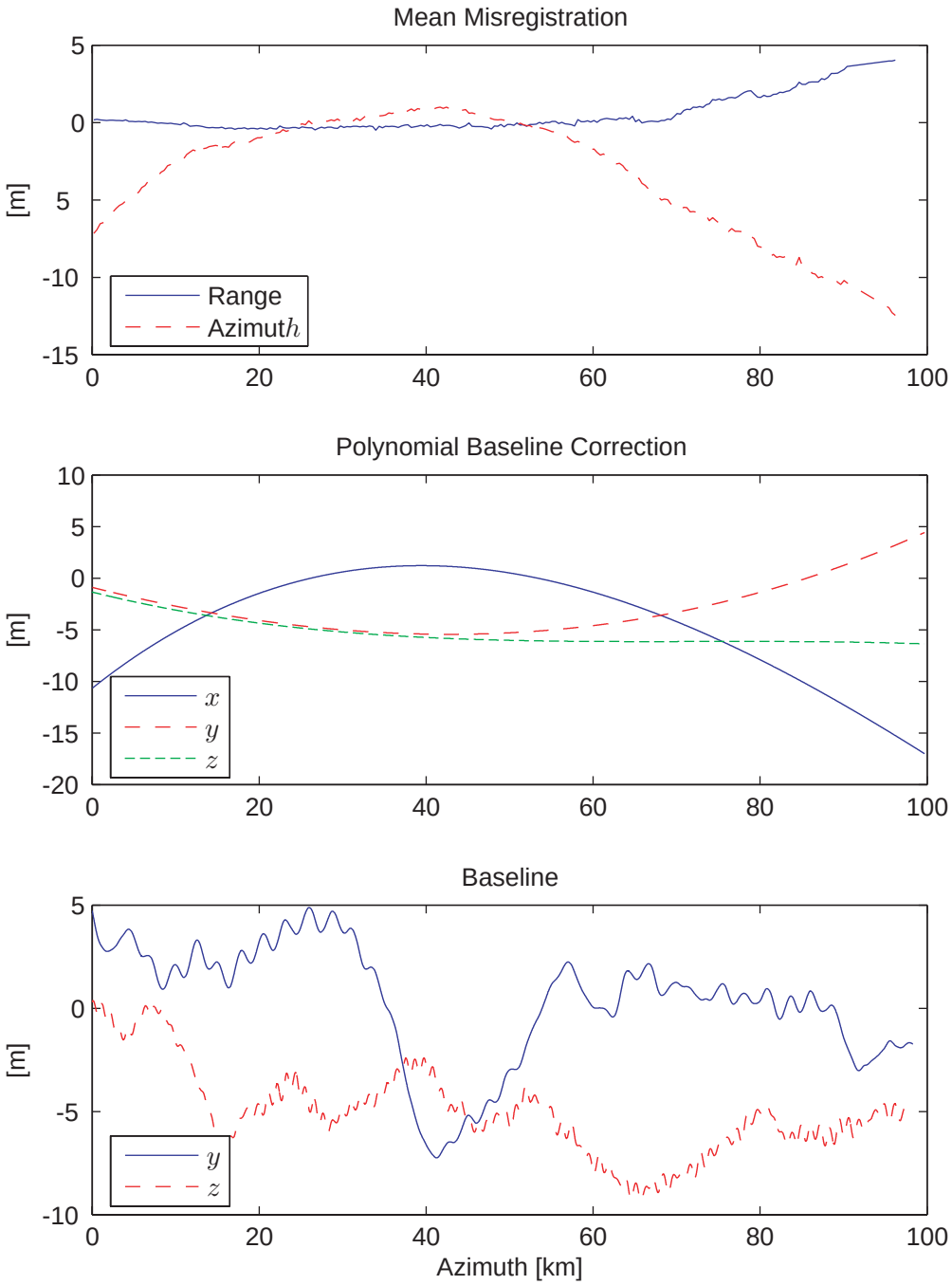

Figure 6.14: Navigation data for `fl045` C-band data, (top) Mean range and azimuth misregistration obtained from speckle correlation, (middle) estimated polynomial baseline correction, (bottom) Final baseline estimate.

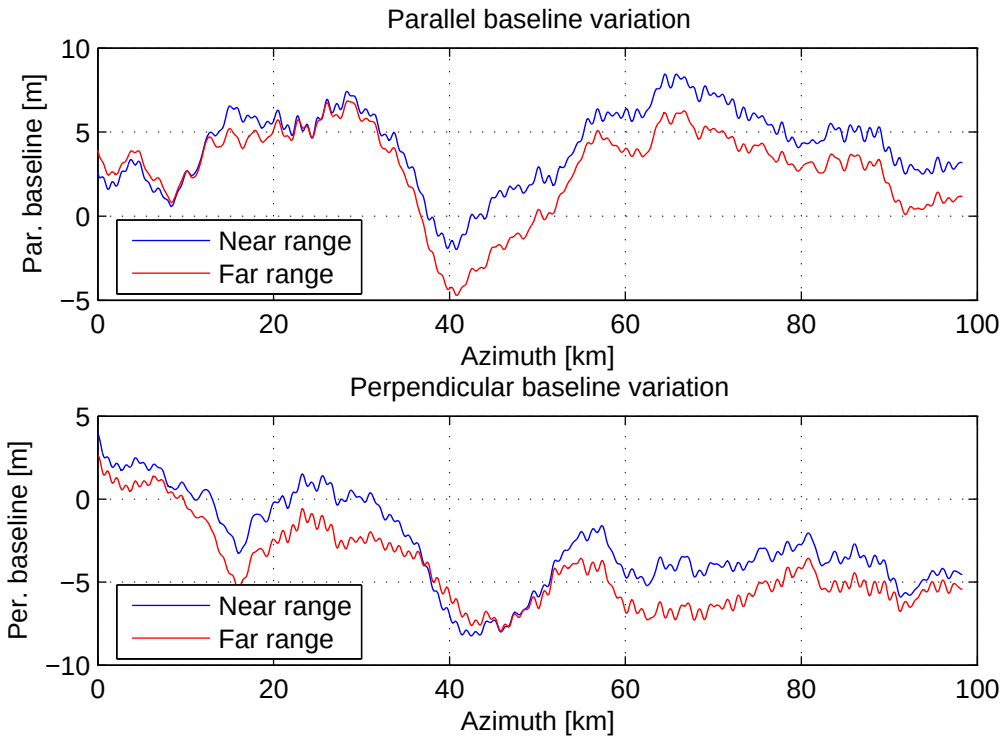

Figure 6.15: Parallel and perpendicular baselines for `f1045`, from the navigation data corrected using polynominal baseline correction.

The polynomial baseline correction was used to correct the navigation data of image 2 (`m0841`), which was then refocused. After refocusing, the residual misregistrations were below 1 m, which is sufficient for interferogram generation, application of SDC, and subsequent RME estimation.

The amplitude, interferogram phase, and coherence images, generated using 11x11 looks, are shown in Figure 6.16, together with the SRTM DEM of the area and the synthetic interferogram generated using this DEM and the motion data. The mean coherence in the image, excluding the large decorrelated ocean areas, is 0.54, but this is most likely due to decorrelation in vegetated areas, as the images were acquired in July. The coherence over vegetated areas is generally lower at C-band than at L-band, due to the smaller wavelength. Comparing the actual interferogram to the synthetic interferogram, it is seen that the expected (i.e. the synthetic) phase variations are small compared to the observed variations, which are most probably caused by differential motion errors.

6.3.2 SDC processing

The azimuth and range misregistration estimation was performed with the spectral diversity coregistration method, with the same parameters and steps as described in 6.2.2. The resulting misregistration images are shown on Figure 6.17. The observed misregistration is the residual after the initial third order polynomial motion error estimation using speckle correlation, so low order motion errors have been removed (see Figure 6.14). However a higher-order residual azimuth misregistration signal

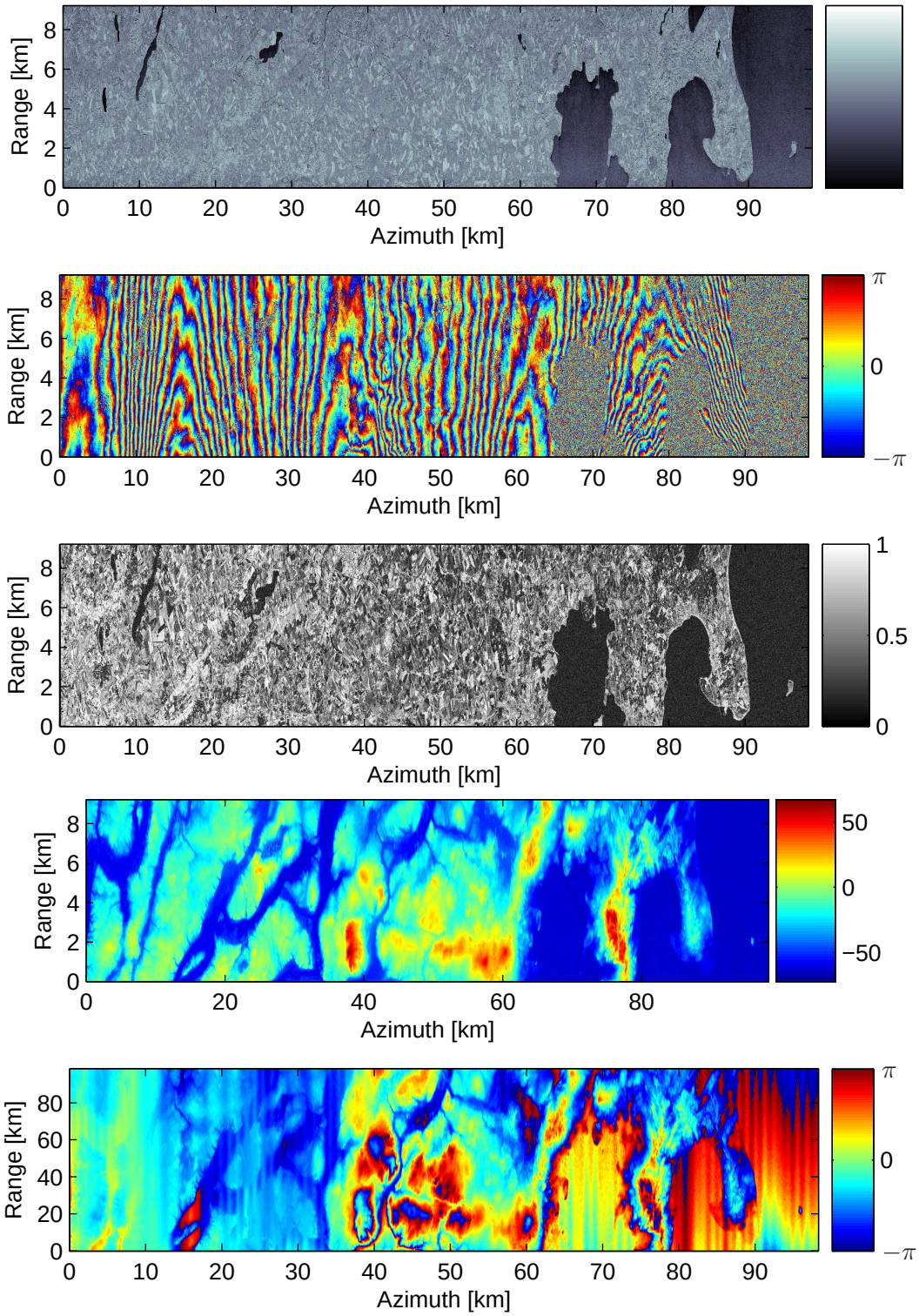

Figure 6.16: `f1045` C-band data after initial focusing and 11x11 multilook, from top down: Amplitude, interferometric phase, coherence, SRTM DEM (converted to height over mocom reference surface), synthetic interferogram from SRTM DEM.

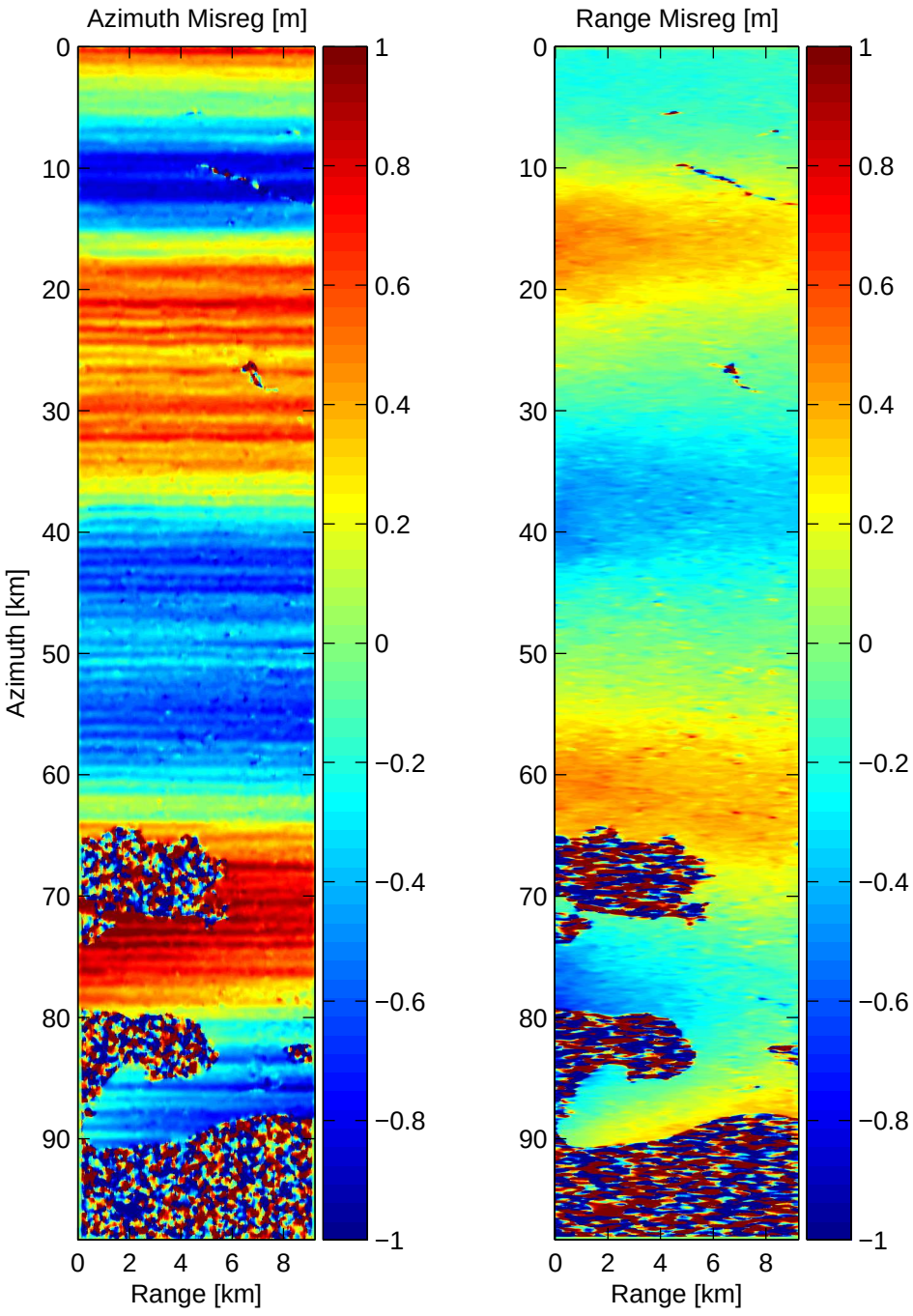

Figure 6.17: `fl045` misregistrations estimated by SDC, (left) Azimuth, (right) Range.

varying between -1 m and 1 m is seen, overlayed with smaller faster variations. The range misregistration also shows a slow variation, but here the variation is from -0.5 m to 0.5 m. The observed misregistrations are likely due to motion errors that could not be modeled by the third-order polynomial because of the long scene length.

6.3.3 RME estimation

The RME estimation was carried out as for the L-band case (section 6.2.3), except that a mean azimuth misregistration was not subtracted, since this had already been removed by the initial polynomial motion error estimation. Topography compensation was also carried out to improve the estimates, but, unlike the L-band case (Figure 6.7), the simulated topography contribution was small compared to the overall estimated error, which is shown on Figure 6.18.

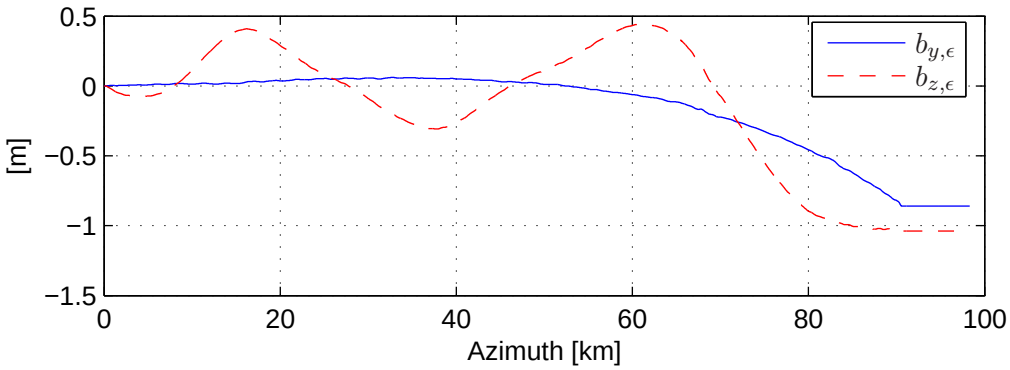

Figure 6.18: `fl045` residual motion errors as estimated by the RME algorithm.

It can be seen from Figure 6.18 that the major variation in the residual error is a slow periodic error on the vertical coordinate, but past 60 km in azimuth, both estimates seem to drift towards negative values. This could be due to the fact that the RME algorithm separation of vertical and horizontal cross-track errors becomes ill-conditioned here (see section 4.4.2), since there are large water areas where no misregistration estimates are available. These are excluded from the estimation, based on a coherence mask, and on Figure 6.19 is shown the condition number of the $\boldsymbol{H}^{\mathrm{T}}\boldsymbol{H}$ matrix used at each azimuth position in the RME estimation (4.51). The condition number is seen to increase tenfold over the mentioned areas, compared to the rest of the image. Further work is needed to increase the RME estimation stability in such cases.

As the estimated residual errors vary significantly compared to the the range resolution, the slave image (`m0841`) navigation data were corrected with the estimated residual error and the image refocused, as described in 4.5. After this processing, a new SDC misregistration estimation was carried out in both range and azimuth, the results of which are shown on Figure 6.20.

Noting the change of scale compared to Figure 6.17, the residual misregistration has been significantly improved, and the remaining azimuth misregistration is high frequency in nature. The rather large variations of up to 0.2 m are due to the simulated topographic misregistration that was subtracted before RME estimation and has therefore not been corrected. In the range misregistration, a slow residual

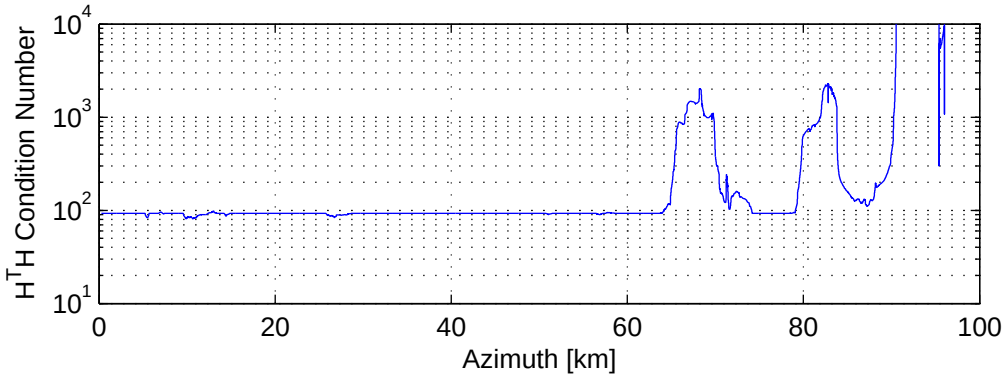

Figure 6.19: Condition number for the $\boldsymbol{H}^{\mathrm{T}}\boldsymbol{H}$ matrix used in RME estimation for `f1045`.

error of up to 15 cm is seen. This is likely due to along-track induced errors. Past 70 km, the range misregistration drifts off significantly, which might be due to large residual along-track errors, but is most likely due to the conditioning problems of the RME estimation mentioned previously. The latter hypothesis is supported by the fact that the initial azimuth misregistration image (Figure 6.17) does not show especially large values past 70 km compared to the rest of the image.

Since misregistration errors of up to 1 m has been corrected by the RME correction, an improvement in coherence is expected. The coherence histograms of the uncorrected and the RME-corrected interferograms are shown on Figure 6.21, where the large water areas have been excluded from the calculation. A notable improvement is seen in the high end, but a large number of low-coherent pixels are still present, probably due to the temporal decorrelation of vegetated areas at C-band.

6.3.4 Along-track error estimation

As mentioned in the previous section, the RME-estimated cross-track errors were corrected by modifying the navigation data and refocusing. After this refocusing, a new interferogram was generated and unwrapped, as described in 6.2.4. The synthetic interferogram was then subtracted to form a residual interferogram for use in along-track error estimation. Since the RME correction was carried out by correcting the navigation data, a new synthetic interferogram was calculated from the corrected navigation data. Due to the small baseline used for this scene (see Figure 6.14), the variation of the interferometric shift in the synthetic interferogram is only a few centimeters in most of the image, which is small compared to the observed range misregistrations. Therefore, an along-track error estimation was also attempted, using the range misregistration image instead of the residual interferogram. In this case, no constant range offset was estimated, since the range misregistration estimate is unambiguous. It is interesting to note that with this approach, no external DEM is needed. 14000 samples of the residual interferogram/range registration image were used in all cases, distributed evenly over the first 60 km of the scene, due to the RME estimation problems mentioned in section 6.3.3. The estimated residual motion parameters are given in Table 6.2, where both a second- and a third-order along-track motion model has been used. The differences in the estimated residual motion parameters are only a few centimeters, which is small compared to the overall

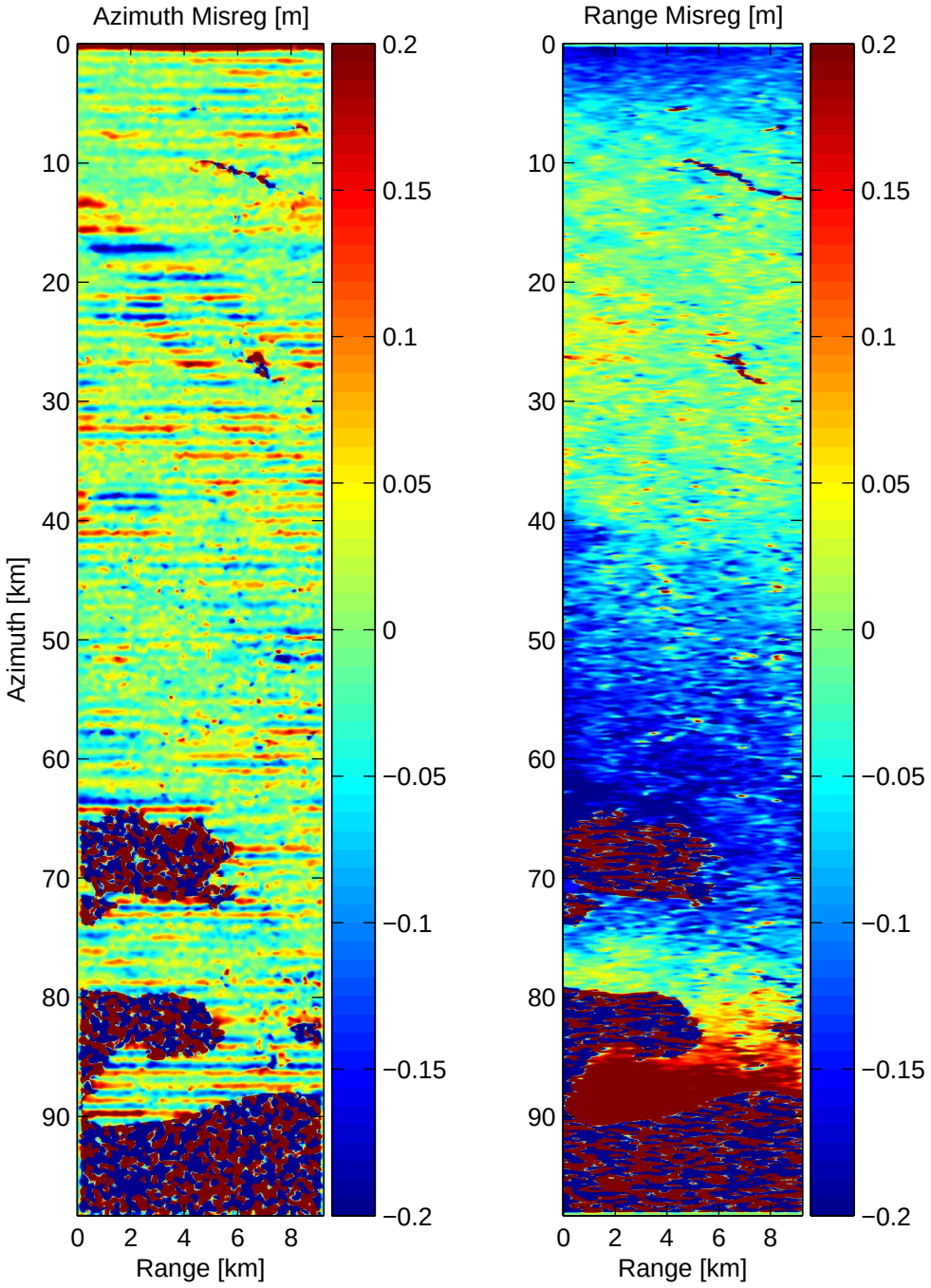

Figure 6.20: SDC estimates of residual misregistrations observed after RME estimation and correction of navigation data.

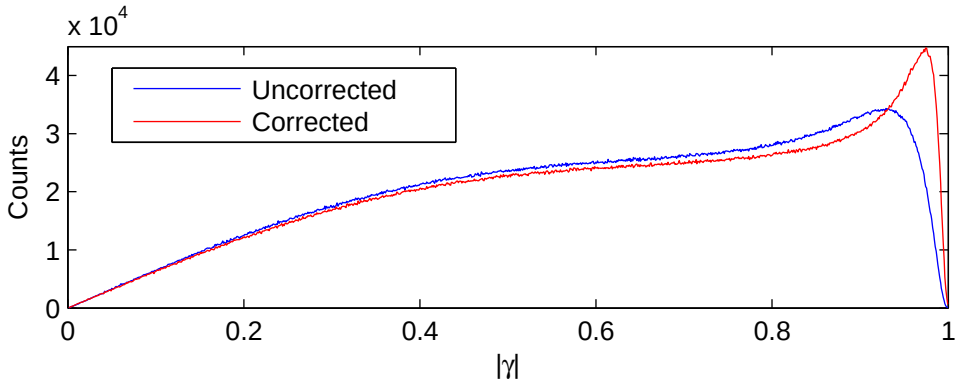

Figure 6.21: Coherence histograms for `f1045`, before and after basic RME-estimation and refocusing.

Case	$\Delta\widehat{r}_{abs}$ [cm]	$\widehat{b}_{y,\epsilon,0}$ [cm]	$\widehat{b}_{z,\epsilon,0}$ [cm]	$\widehat{b}_{x,\epsilon,0}$ [cm]	$\widehat{b}_{x,\epsilon,1}$ [cm]	$\widehat{b}_{x,\epsilon,2}$ [cm]	$\widehat{b}_{x,\epsilon,3}$ [cm]
$\widehat{\boldsymbol{Q}}_{p2}$	6.2	−1.1	−13.0	−2.3	12.5	−6.0	-
$\widehat{\boldsymbol{Q}}_{p3}$	6.2	−1.1	−13.2	−2.3	13.0	−6.0	0.4
$\widehat{\boldsymbol{Q}}_{r2}$	-	1.4	−11.6	−1.8	10.8	−5.3	–
$\widehat{\boldsymbol{Q}}_{r3}$	-	1.4	−11.6	−1.8	10.7	−5.3	0.0

Table 6.2: Estimated residual motion parameters for `f1045` using the along-track estimation described in section 5.1.1, with both second and third order along-track error model. Subscript p means that that the residual interferogram was used for along-track estimation, while r indicates that only the range registration was used. Note that the $\tilde{b}_x$ parameters are given as Chebyshev coefficients. The fit interval is from 0 km to 60 km.

values. Also it is seen that a second order along-track motion model seems sufficient to model the observed residual phase and misregistrations, as the estimated residual motion parameters change by less than 5 mm by adding a third order term to the along-track motion model ($\widehat{\boldsymbol{Q}}_{p3}$ and $\widehat{\boldsymbol{Q}}_{r3}$).

Using the estimated second-order along-track motion parameters of Table 6.2, a final vertical motion correction was calculated according to (5.21), and this is shown on Figure 6.22 for the fit interval from 0 to 60 km. The correction $\tilde{b}_{z,\epsilon}$ is a relative correction with respect to the inital RME-correction $\widehat{b}_{z,\epsilon}$ on Figure 6.18, and the estimated constant baseline offset has been added. The difference between the cross-track motion estimates obtained using the external DEM, and the estimates obtained using the range misregistration is no more than two centimeters, except for the constant horizontal offset, which is slightly larger. To illustrate the along-track estimation, the residual interferogram before along-track correction is shown on Figure 6.23 together with the phase correction calculated from the estimated vertical error $\tilde{b}_{z_\epsilon}(x)$ and the estimated constant baseline offset. It is seen that there is good agreement from 0 to 60 km, for which the along-track motion model has been fitted.

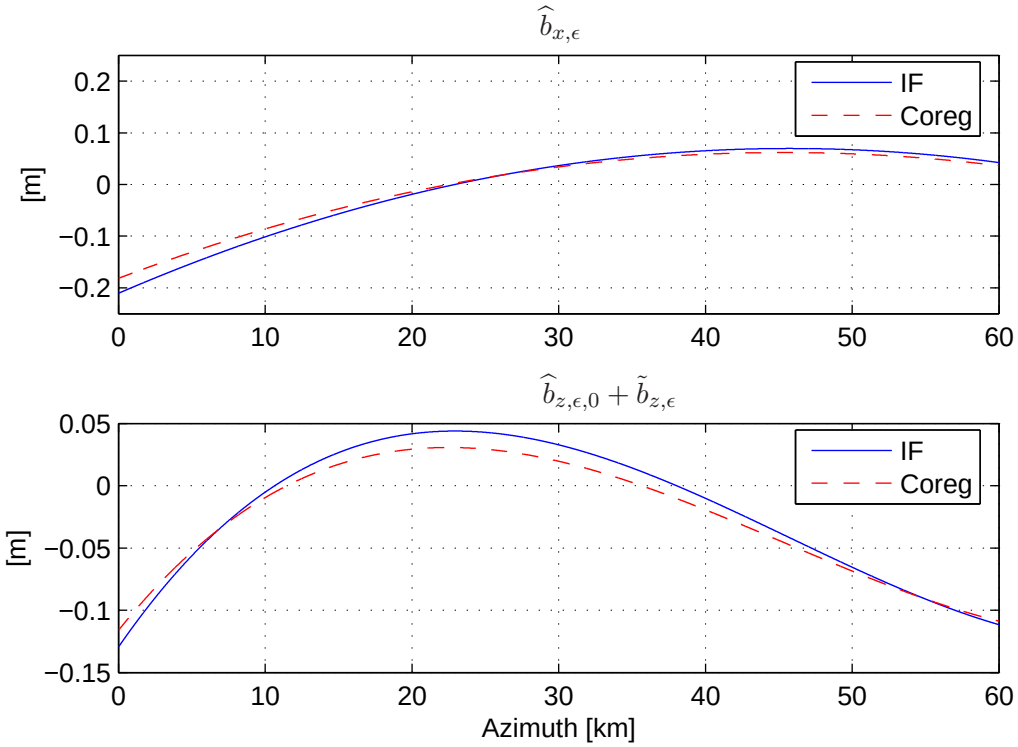

Figure 6.22: `f1045` final motion correction, as estimated by the 3^{rd}-order along-track error estimation. The solid blue curves were estimated using the external DEM, whereas the dashed red curves were obtained using only the range misregistration for along-track error estimation.

After the along-track motion estimation, the slave image navigation data were corrected in both along-track and cross-track coordinates using the motion correction estimated from the residual interferogram with the second-order along-track motion model, $\widehat{\boldsymbol{Q}}_{p3}$. Then the image was refocused, following which a final interferogram

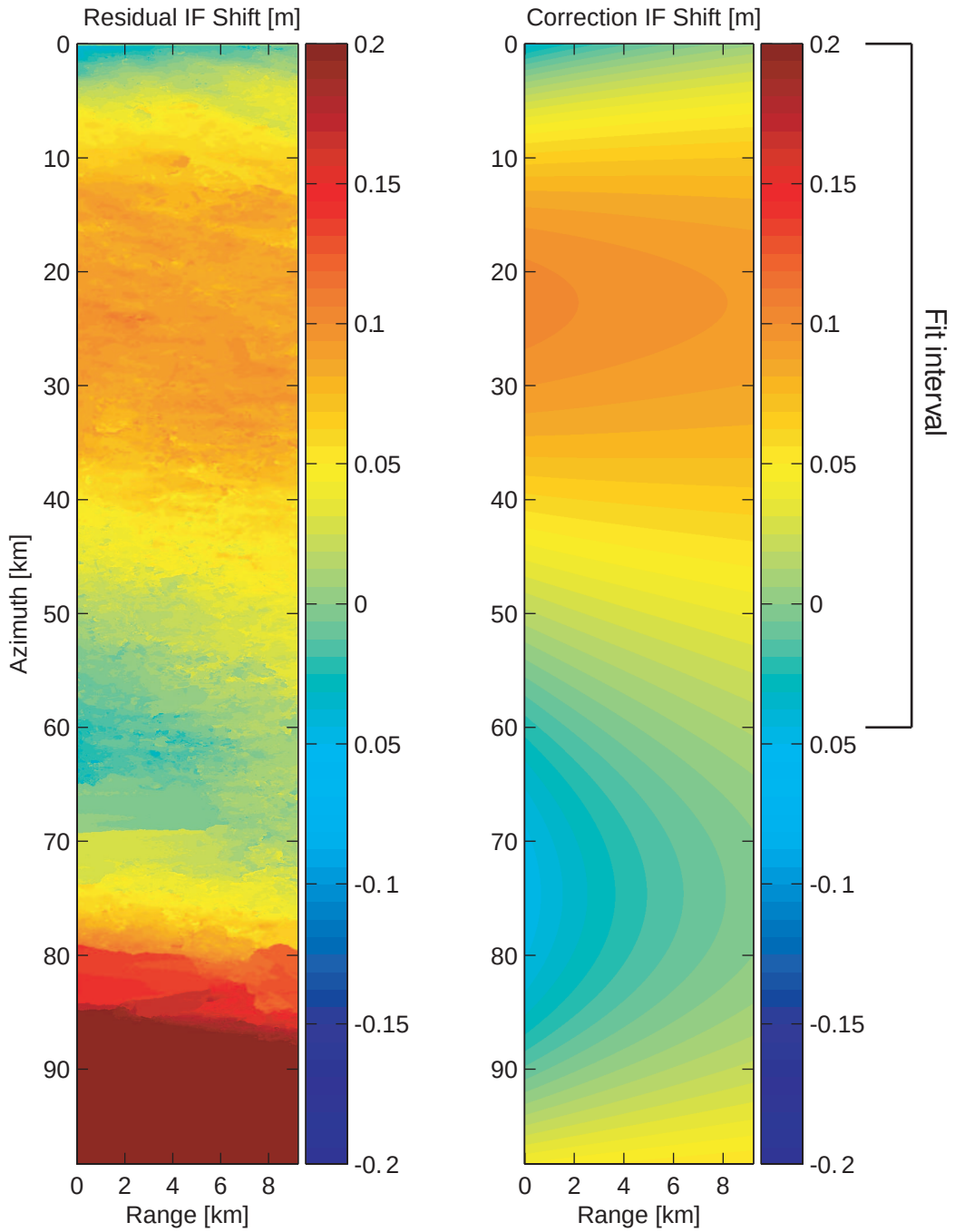

Figure 6.23: Residual interferogram (converted to range shift) and estimated correction with a 3^{rd}-order along-track motion model. Note that the model has only been fitted from 0 to 60 km in azimuth.

was calculated and unwrapped. Spectral diversity range and azimuth misregistration estimation were also carried out, and the residual azimuth misregistration was virtually unchanged compared to the residual azimuth misregistration of the basic RME-corrected image of Figure 6.20. This is as expected, since the misregistration from the applied along-track correction balances out with the misregistration induced by the cross-track correction.

In the range misregistration image, a mean offset of 2.6 cm is still present, the reason for which is not known. It might be related to the fact that the data were corrected using the final motion parameters estimated from the residual interferogram. Here an absolute range offset of 6.2 cm (which might include an $N \cdot 2\pi$ phase ambiguity, corresponding to $N \cdot 2.83$ cm) was estimated, but this has not been applied to the navigation data correction, as it is not possible to correct it this way. Such a constant offset is easy to calibrate out, however. A final residual interferogram was also calculated by subtracting from the final interferogram the synthetic interferogram calculated from the final navigation data. In this case, an offset of 2.7 cm was seen. In Figure 6.24 the absolute variation of the residual range misregistration is shown, together with the absolute residual interferogram variation. In both cases, the mean value has been subtracted before taking absolute values. It is seen that the slow variation in the residual phase and misregistration (Figures 6.20 and 6.23) has been removed, and the final variation of the residual interferometric shift is below 2 cm over the entire fit area from 0 to 60 km. The RMS value of the residual interferometric shift is 7 mm. This is on the order of the RMS value typically seen from atmospheric effects (see section 4.1.2). The appearance of the range misregistration image is probably due to noise in the SDC estimate as well as topography, which is included in the range registration.

To obtain independent verification of the final misregistration estimate, an `emidif` speckle correlation using 24×256 patches across the image was carried out between the master and the final corrected slave image. Azimuth profiles (averaged in the range direction) of the `emidif` misregistration estimates are compared to the SDC estimates on Figure 6.25. For the fit area from 0 to 60 km, the mean range misregistration of 2.6 cm is observed on both the `emidif` and SDC estimates, with variations from this value of less than two centimeters. Past 60 km, the range misregistrations increase due to the conditioning of the RME estimate in this area (see section 6.3.3).

In the azimuth misregistration, it is seen that the `emidif` misregistration estimates are undersampled compared to the SDC estimates. The residual mean azimuth misregistrations of up to 5 cm are due to the topography-induced azimuth misregistrations, which are not corrected with the approach in this work. This could be done if topography-dependent motion compensation was carried out, as mentioned in 5.2.4.

6.4 Discussion

For the L-band scene treated in section 6.2 it was seen that the major part of the differential motion error and related azimuth misregistration was corrected by the basic RME algorithm (section 4.4.2), and only a slight improvement was achieved by using the proposed along-track residual motion correction (section 5.1.1) instead of a standard calibration method. The improvement from applying the topography

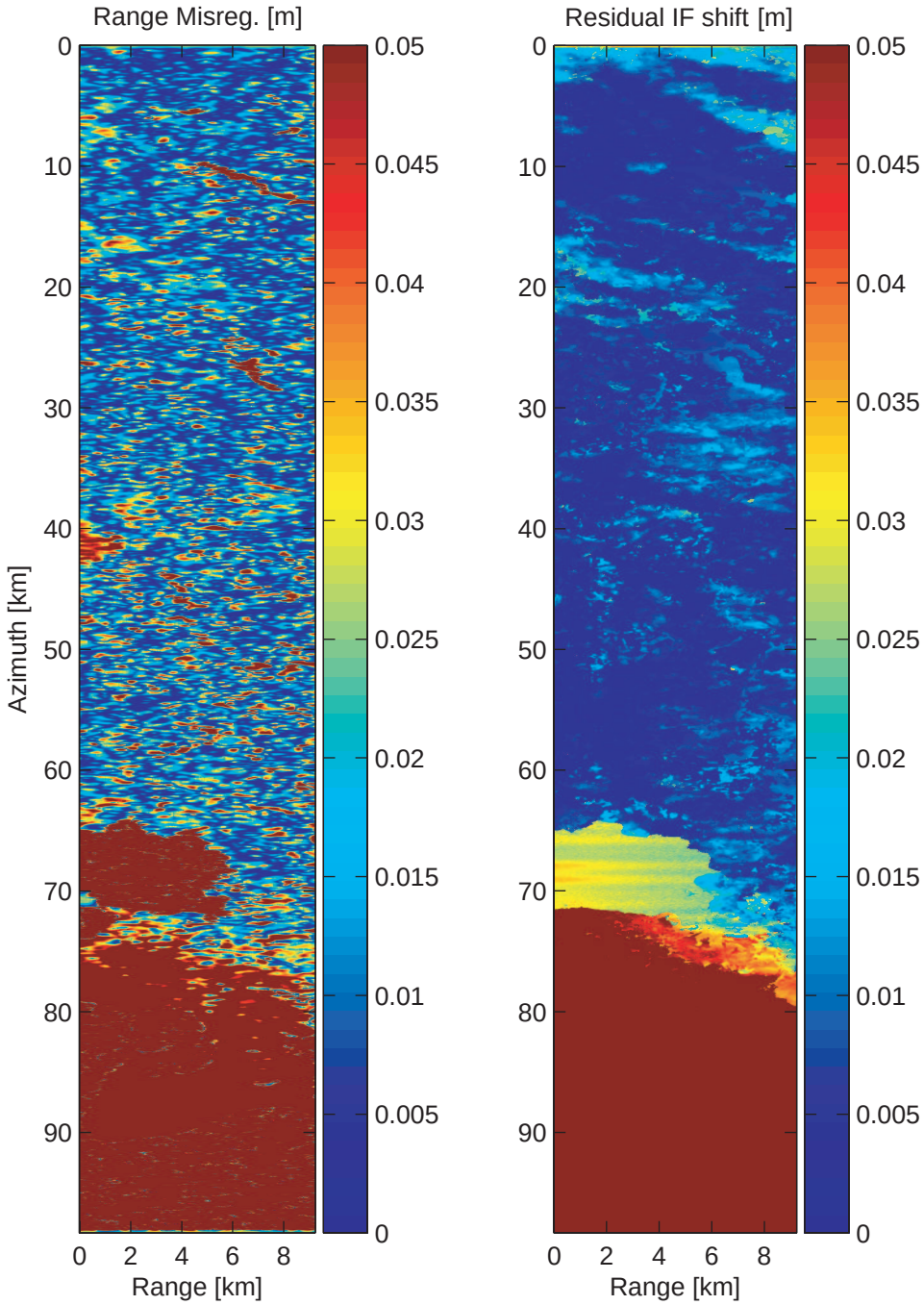

Figure 6.24: Absolute values of residual range misregistration and residual interferogram (converted to range) after final motion data correction and refocusing. The mean value of 2.6 cm has been subtracted from the range registration, and a mean of 2.7 cm has been subtracted from the residual interferograms. The means were subtracted before taking absolute values.

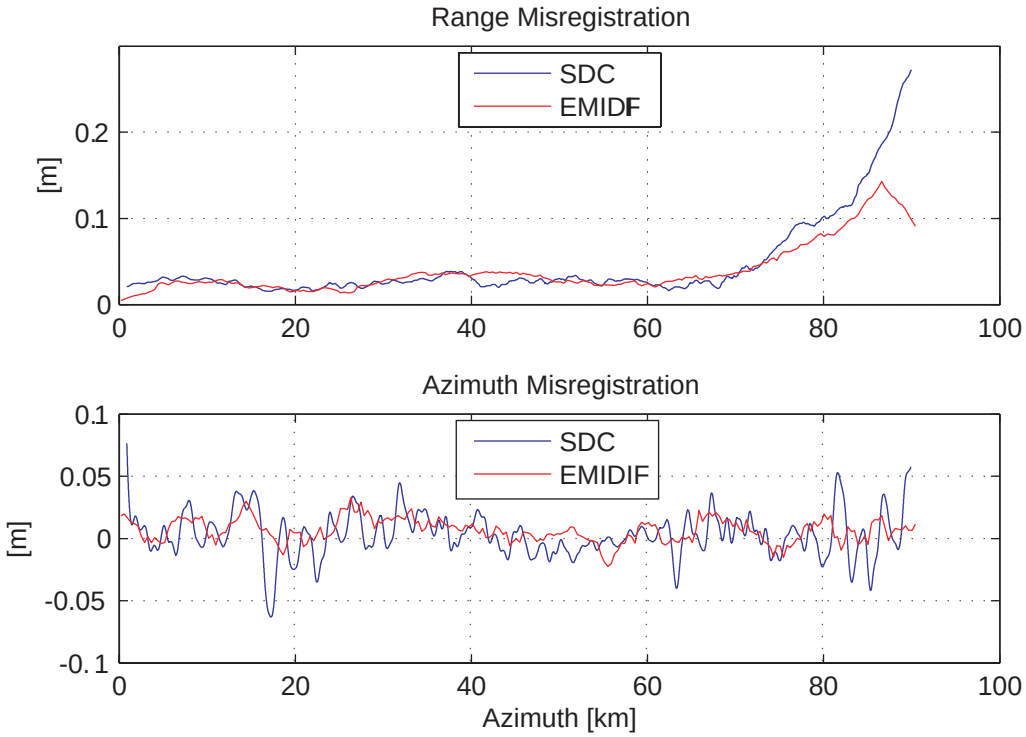

Figure 6.25: Comparison of final misregistration estimates from speckle correlation (`emidif`) and spectral diversity (SDC).

compensation (section 5.2.4) was also slight, however it could be observed in the final residual interferograms. In all cases, the RMS deviations of the residual devations were comparable to the expected deviations of the external SRTM DEM, to which the data were calibrated. More work is needed to improve the estimate of the absolute phase and the constant differential motion error, using the range misregistration estimate.

For the long C-band scene processing described in section 6.3, it was seen that the RME algorithm again compensated the major part of the differential motion error. However, a residual quadratic error was seen in both the range registration and the residual interferometric shift. Here, the proposed along-track motion estimation algorithm accurately compensated for this, except for a 2.6 cm offset that was observed in both the final range misregistration and interferogram. This is probably related to a constant phase offset between the two images, and is easily calibrated out. Otherwise, the observed variations of the residual interferograms was below 2 cm and not systematic in nature. This is true for the first 60 km of the scene. Past 60 km, the observed range misregistration could not be corrected, but this was probably due to stability problems in the RME algorithm caused by the narrow swath available here due to the ocean. More work is needed to improve the stability of the RME algorithm over such areas. It might be possible to constrain the RME estimate using the observed range misregistration, or by extrapolation of the estimated RME derivatives from neighbouring azimuth positions where a wider swath is available.

Chapter 7

Conclusions

The present thesis has dealt with two aspects of motion errors in airborne SAR, propeller induced motion errors and residual motion estimation in repeat track interferometry.

7.1 Vibration analysis

In Chapter 3, the impact of propeller-induced vibration on the SAR impulse response was examined through spectral analysis and point target simulations using motion data measured on a C-130 heavy turboprop aircraft, a Piper PA31 light turpopiston aircraft, and, for reference a Gulfstream GIII jet aircraft. The overall conclusion is that the estimated physical vibration amplitudes above 5-10 Hz do not seem to lead to unacceptable sidelobes in the SAR impulse responses. However, it was found that aliasing of the measured propeller-induced vibration in the motion sensor could, when performing motion compensation, lead to unacceptable spurious sidelobe levels of up to -26 dB in a high-resolution X-band system if a 50 Hz motion sensor was used in a C-130. However, the applied motion sensor was capable of delivering 200 Hz motion data, for which case there did not seem to be any unacceptable sidelobe levels.

For the Piper PA31 case, only 50 Hz motion data were collected, and in this case, all the observed motion above some 5 Hz was seen to be aliased. The simulated sidelobe levels for this case were below -30 db, but such sidelobes could be removed by low-pass filtering the motion data before applying them in motion compensation. Using a higher frequency motion sensor would also alleviate the problem.

For the GIII Gulfstream jet aircraft, there were no high frequency vibrations significant enough to cause sidelobes above the nominal Hamming-weighted impulse response.

7.2 Residual motion errors in RTI

In the second part of this thesis, an existing differential motion error estimation algorithm, the RME algorithm, has been implemented in MATLAB and tested on EMISAR data. As a prerequisite for this, it was also necessary to implement the

Spectral Diversity (SDC) algorithm for misregistration estimation. The RME algorithm integrates the estimated azimuth misregistrations to obtain an estimate of the differential cross-track motion error. The principles behind the algorithm is described in Chapter 4. A strength of the RME algorithm is that is non-parametric, so cross-track motion errors with arbitrary variation can be estimated. However, the algorithm cannot in itself estimate a constant cross-track error, which must be estimated using tie-points or an external DEM.

In Chapter 5, two improvements to the RME algorithm were proposed. The improvement which seems most significant is a scheme to correct for errors in the RME estimate due to along-track motion errors. Differential along-track motion errors cause azimuth misregistrations which in the RME algorithm are interpreted, incorrectly, as due to a cross-track velocity error. The proposed algorithm uses an external digital elevation model (DEM) to estimate the errors due to along-track motion. The along-track error is modeled as having a polynomial variation, but this is not a significant limitation, as only slowly varying along-track errors will affect the RME estimate significantly, and a fast variation in the along-track error can be ignored. Using the estimated along-track error, the cross-track motion data can then be corrected for the errors initially induced by the RME estimation, without affecting the corrected azimuth misregistration. Together with the along-track motion, the constant cross-track offset (see above) and a phase offset is also estimated.

Another error source in the RME algorithm is azimuth misregistrations caused by uncompensated topography coupling with sensor cross-track velocities. A method is proposed for compensating this error contribution in the RME algorithm using an external DEM. The proposed method is simple and does not correct the azimuth misregistrations induced by the topography. This can only be achieved using topography dependent motion compensation, which complicates the SAR processing considerably.

In Chapter 6, the RME algorithm has been applied to two different scenes, an L-band scene with an azimuth length of 22.5 km and a C-band scene with a length of 100 km. The proposed modifications to the RME algorithm were then applied to see if they could improve the results. Both of the proposed modifications require an external DEM, and the DEM used in this work is the Shuttle Radar Topography Mission (SRTM) DEM.

In the L-band scene, kinematic GPS data were available, but a fast varying azimuth misregistration motion error of up to ± 0.5 m was observed, the main part of which was probably due to an uncompensated delay between radar data and navigation data for both images. These variations were corrected by the RME algorithm, and a slowly varying residual phase of 10-15 cm could then be modeled by the along-track motion estimation. This left a residual RMS phase variation equivalent to 1.4 cm between the corrected interferogram and the synthetic interferogram generated from the DEM. This was shown to be consistent with the expected DEM noise from the external DEM. Compared to a standard DEM calibration (estimating and correcting a constant cross-track offset in the range direction and a linear phase in azimuth) of the RME-corrected interferogram, the along-track error estimation method produced slightly better results for the L-band data. The implemented topographic misregistration correction slightly improved the observed RMS phase variation (after along-track correction) from 1.4 cm to 1.3 cm. However, the estimation of the constant cross-track baseline error and the absolute phase offset caused problems,

which still need further work. It is expected that the range misregistration can be applied in this case.

In the C-band scene, the RME algorithm also corrected the major part of the differential motion errors, but here a slow varying residual quadratic error of up to 15 cm was seen on both the residual interferogram and range misregistration. This could be accurately modeled by the proposed along-track error estimation, leaving a residual error variation below 2 cm over the 60 km strip to which the data were fitted. It was also found that the along-track induced error could alternatively be estimated by the residual range misregistration to obtain final motion correction estimates within 2 cm of the estimates obtained from the residual phase and the DEM. This is interesting, as an external DEM is not necessary in this case. However, avoiding an external DEM is not generally possible if the range misregistration is significantly affected by topography.

The proposed along-track motion estimation algorithm seems stable, (except for the estimation of the constant baseline offset and absolute phase), and seems to be able to model succesfully the slow-varying residual motion errors observed after standard RME correction. This could have applications in differential interferometry and repeat pass DEM generation in cases where a rough DEM of the imaged area is available beforehand, and the stationary parts of the scene can be used for RME estimation.

Further investigations are probably needed to verify the merits of the proprosed topography compensation for the RME algorithm although it seems to offer a slight improvement in the L-band case. This could be examined using a scene with more topography, but this was not done.

7.3 Acknowledgements

I wish to thank Kristian Keller, formerly at the National Survey and Cadastre (KMS), for supplying the PA31 navigation data as well as for lending out their EGI unit. Also, thanks to Andreas Reigber for having me as a guest at the Technical University of Berlin, and to Johan Mohr for assistance in using the `sarif` SAR processor and associated tools. Steen Savstrup Kristensen is thanked for his help in recovering raw EMISAR data from damaged tapes, Sten Schmidl for moral support and for his assistance before and during the C-130 EGI data collection. Finally, thanks to my supervisors, Erik Lintz Christensen and Jørgen Dall for always taking time out of their busy schedule when necessary.

Bibliography

[1] Christensen, E.L. (editor), "SAR++ System Design Report," Tech. Rep. R693, Ørsted•DTU - Electromagnetic Systems, 2000.

[2] Reigber, A. and Papathanassiou, K.P., "Correction of residual motion errors in airborne repeat-pass interferometry," *Geoscience and Remote Sensing Symposium, 2001. IGARSS '01. IEEE 2001 International*, vol. 7, pp. 3077–3079, 2001.

[3] Kirk, J.C., "Motion compensation for synthetic aperture radar," *IEEE Transactions on Aerospace and Electronic Systems*, vol. AES-11, no. 3, pp. 338–48, 1975.

[4] Fornaro, G., "Trajectory deviations in airborne SAR: analysis and compensation," *IEEE Transactions on Aerospace and Electronic Systems*, vol. 35, no. 3, pp. 997–1009, 1999.

[5] Carrara, W.G. and Goodman, R.S. and Majewski, R.M, *Spotlight Synthetic Aperture Radar: Signal Processing Algorithms.* Artech House Inc., 1995.

[6] Curlander, J.C. and McDonough, R.N., *Synthetic Aperture Radar - Systems and Signal Processing.* John Wiley & Sons, 1991.

[7] Bamler, R., "A comparison of range-Doppler and wavenumber domain SAR focusing algorithms," *Geoscience and Remote Sensing, IEEE Transactions on*, vol. 30, no. 4, pp. 706 –713, 1992.

[8] Klauder, J.R. and Price, A.C. and Darlington, S. and Aldersheim, W.J, "The Theory and Design of Chirp Radars," *Bell System Technical Journal*, vol. 39, no. 4, pp. 745–808, 1960.

[9] Klein, J.D. and Hensley, S. and Madsen, S.N. and Webb, F.H., "Results of 1993 repeat-pass SAR interferometry experiments," *Geoscience and Remote Sensing Symposium, 1994. IGARSS '94. Surface and Atmospheric Remote Sensing: Technologies, Data Analysis and Interpretation., International*, vol. 1, pp. 295 –297 vol.1, 1994.

[10] Grewal, Mohinder S. and Weill, Lawrence R. and Andrews, Angus P., *Global Positioning Systems, Inertial Navigation, and Integration.* John Wiley & Sons, Inc., 2001.

[11] Hoogeboom, P. and Snoeij, P. and Koomen, P.J. and Pouwels, H., "The PHARUS project, results of the definition study including the SAR testbed

PHARS," *IEEE Transactions on Geoscience and Remote Sensing*, vol. 30, no. 4, pp. 723–735, 1992.

[12] Horn, R., "E-sar - The Experimental Airborne L/c-band Sar System Of DFVLR," *Geoscience and Remote Sensing Symposium, 1988. IGARSS '88. Remote Sensing: Moving Toward the 21st Century., International*, vol. 2, pp. 1025–1026.

[13] Kusk, A. and Dall, J. and Christensen, E.L., "Aircraft Vibrations and Navigation System Performance in SAR," *Proceedings, EUSAR 2004*, vol. 1, pp. 325–328, 2004.

[14] Honeywell Millitary Avionics Division, St. Petersburg, Florida, *Prime Item Development Specification for the H764G Embedded GPS Receiver in an INS (EGI) Rev. F*, 1995.

[15] Honeywell Military Avionics Division, *System Description For Honeywell's H-764G Block II Embedded Global Positioning System (GPS) Receiver In An Inertial Navigation System (INS)*, September 1993.

[16] Honeywell International, Inc., *Q-Flex QA2000 Accelerometer Datasheet*. Available from http://www.inertialsensor.com/docs/qa2000.pdf.

[17] Majure, R.G., "Demonstration of a ring laser gyro system for pointing and stabilization applications," *Position Location and Navigation Symposium, 1990. Record.*, pp. 219 –225, 1990.

[18] Stoica, Petre and Moses, Randolph L., *Introduction to Spectral Analysis*. Prentice-Hall, 1997.

[19] "Personal Communication with Östling and Dammert of Ericsson Microwave Systems AB, Airborne Radar Divison, 2004.".

[20] Östling, D. and Dammert, P.B.G., "Generation and Geocoding of High Resolution SAR Images with the Ericsson SAR/GMTI Experiment System," *Proceedings of EUSAR 2004*, vol. 2, pp. 941–944, 2004.

[21] Mohr, J. J., *Repeat Track SAR Interferometry - An Investigation of its Utility for Studies of Glacier Dynamics*. PhD thesis, Technical Univeristy of Denmark - Department of Electromagnetic Systems, 1997. LD125.

[22] Hannsen, R., *Atmospheric heterogeneities in ERS tandem SAR interferometry*. Delft University Press, 1998.

[23] Bamler, R. and Just, D., "Phase statistics and decorrelation in SAR interferograms," *Geoscience and Remote Sensing Symposium, 1993. IGARSS '93. Better Understanding of Earth Environment., International*, vol. 3, pp. 980–984, 1993.

[24] Gatelli, F. and Guamieri, A.M. and Parizzi, F. and Pasquali, P. and Prati, C. and Rocca, F., "The wavenumber shift in SAR inferometry," *Geoscience and Remote Sensing, IEEE Transactions on*, vol. 32, no. 4, pp. 855 –865, 1994.

[25] Stevens, D.R. and Cumming, I.G. and Gray, A.L., "Options for airborne interferometric SAR motion compensation," *Geoscience and Remote Sensing, IEEE Transactions on*, vol. 33, no. 2, pp. 409 –420, 1995.

[26] Scheiber, R. and Moreira, A., "Coregistration of interferometric SAR images using spectral diversity," *Geoscience and Remote Sensing, IEEE Transactions on*, vol. 38, no. 51, pp. 2179 –2191, 2000.

[27] Madsen, S.N., "On absolute phase determination techniques in SAR interferometry," *Proceedings of the SPIE - The International Society for Optical Engineering*, vol. 2487, pp. 393–401, 1995.

[28] Bamler, R. and Eineder, M., "Accuracy of Differential Shift Estimation by Correlation and Split-Bandwidth Interferometry for Wideband and Delta-k SAR Systems," *Geoscience and Remote Sensing Letters, IEEE*, vol. 2, no. 2, pp. 151–155, 2005.

[29] Madsen, S.N and Zebker, H., *Manual of Remote Sensing, 3rd ed.*, ch. 6. Imaging Radar Interferometry. American Society for Photogrammetry and Remote Sensing, 1997.

[30] Mohr, J. J. and Madsen, S. N., "Parametric Estimation of Time Varying Baselines in Airborne Interferometric SAR," *Proceedings of IGARSS'96*, vol. 1, pp. 677–679, 1996.

[31] Reigber, A. and Prats, P. and Mallorqui, J.J., "Refined estimation of time-varying baseline errors in airborne SAR interferometry," *Geoscience and Remote Sensing Symposium, 2005. IGARSS '05. Proceedings. 2005 IEEE International*, vol. 7, pp. 4799–4802, 2005.

[32] Scheiber, R. and Robert, P., "Origin and correction of phase errors in airborne repeat-pass SAR interferometry," *Geoscience and Remote Sensing Symposium, 2001. IGARSS '01. IEEE 2001 International*, vol. 7, pp. 3114–3116, 2001.

[33] Prats, P. and Reigber, A. and Mallorqui, J.J., "Interpolation-Free Coregistration and Phase-Correction of Airborne SAR Interferograms," *Geoscience and Remote Sensing Letters, IEEE*, vol. 1, no. 3, pp. 188–191, 2004.

[34] Prats, P. and Reigber, A. and Mallorqui, J.J. and Broquetas, A., "Efficient detection and correction of residual motion errors in airborne SAR interferometry," *IGARSS 2004. 2004 IEEE International Geoscience and Remote Sensing (IEEE Cat. No.04CH37612)*, pp. 992–5 vol.2, 2004.

[35] "http://www.jpl.nasa.gov/srtm/."

[36] Prats, P. and Reigber, A. and Mallorqui, J.J., "Topography-Dependent Motion Compensation for Repeat-Pass Interferometric SAR Systems," *Geoscience and Remote Sensing Letters, IEEE*, vol. 2, no. 2, pp. 206–210, 2005.

[37] Rosen, P.A. and Hensley, S. and Gurrola, E. and Rogez, F. and Chan, S. and Martin, J. and Rodriguez, E., "SRTM C-band topographic data: quality assessments and calibration activities," *Geoscience and Remote Sensing Symposium, 2001. IGARSS '01. IEEE 2001 International*, vol. 2, pp. 739–741, 2001.

[38] Reigber, A. and Scheiber, R., "Airborne differential sar interferometry: first results at L-band," *Geoscience and Remote Sensing, IEEE Transactions on*, vol. 41, no. 62, pp. 1516–1520, 2003.